A TEST FOR EVALUATING THE DOWNSCALING ABILITY OF ONE-WAY NESTED REGIONAL CLIMATE MODELS: THE BIG-BROTHER EXPERIMENT

Bertrand Denis

Department of Atmospheric and Oceanic Sciences

McGill University

Montréal, Québec, Canada

Submitted: August 2001
In final form: January 2002

A thesis submitted to the Faculty of Graduate Studies
and Research in partial fulfilment of the requirements for
the degree of
PHILOSOPHIAE DOCTOR

in the collaborative McGill-UQAM
Ph.D. programme of Meteorology

0-612-78674-9

À ma chère mère

et

à Catherine, Valérie et Nicolas

ABSTRACT

The purpose of this thesis is to evaluate the downscaling ability of one-way nesting regional climate models (RCM). To do this, a rigorous and well-defined experiment for assessing the reliability of the one-way nesting approach is developed. This experiment, baptised the Big-Brother Experiment (BBE), is used for addressing some important one-way nesting issues.

The first part of this work is dedicated to the development of a scale decomposition tool employed for the BBE. This tool involves a new spectral analysing technique suitable for two-dimensional fields on limited-area domains, and is based on the discrete cosine transform (DCT). It is used for degrading the spatial resolution of the lateral boundary conditions (LBC) used to drive the Canadian RCM (CRCM), for extracting mesoscale features from the atmospheric fields, and for regional validation, and producing power spectra.

The second part of the thesis describes the BBE framework and its first results. The BBE consists in first establishing a reference virtual-reality climate from an RCM simulation using a large and high-resolution domain. This simulation is called the "Big Brother". This big-brother simulation is then degraded toward the resolution of today's global objective analyses (OA) and/or global climate models (GCM) by removing the short scales. The resulting fields are then used as nesting data to drive an RCM (called the "Little Brother") which is integrated at the same high-resolution as the Big Brother, but over a sub-area of the big-brother domain. The climate statistics of the Little Brother are

then compared with those of the big-brother simulation over the little-brother domain. Differences between the two climates can thus be unambiguously attributed to errors associated with the dynamical downscaling technique, and not to model errors nor to observation limitations. The results for a February simulation shows that the Canadian RCM, using a factor of 6 between the model and the LBC spatial resolution, and an update interval of 3 hours, is capable to pass the BBE test; thus showing the reliability of the one-way nesting approach.

In the third and last part of the thesis, the BBE is used to investigate the sensitivity of an RCM to the spatial resolution and temporal update frequency of the LBC. It is shown that spatial resolution jumps of 12, and an update frequency between twice a day (every 12 hours) and four times a day (every 6 hours), are the limits for which a 45-km RCM yields acceptable results.

RÉSUMÉ

Le propos de cette thèse est d'évaluer l'habileté de raffinement des modèles régionaux de climat (MRC) utilisant la méthode de pilotage unidirectionnel. À cette fin, une expérience rigoureuse et bien définie est développée pour évaluer la fiabilité de la méthode de pilotage unidirectionnel. Cette expérience, baptisée l'Expérience "Grand Frère" (EGF), est utilisée pour s'attaquer à quelques problématiques concernant la méthode de pilotage unidirectionnel.

La première partie de cette thèse porte sur le développement d'un outil servant à la décomposition d'échelle dans le cadre de l'EGF. Cet outil fait appel à une nouvelle technique d'analyse spectrale appropriée pour des champs définis sur des domaines à aire limitée, et est basé sur les transformées discrètes de cosinus (TDC ou DCT en anglais). Il est employé pour dégrader la résolution spatiale des conditions frontières latérales (CFL) servant à piloter le MRC, pour extraire les détails à la méso-échelle des champs atmosphériques dans le but de faire leur validation, et enfin, pour produire des spectres de puissance.

La deuxième partie de cette thèse décrit le cadre de l'EGF ainsi que ses premiers résultats. L'EGF consiste à premièrement établir un climat virtuel de référence à partir d'une simulation d'un MRC utilisant un large domaine à haute résolution. Cette simulation est appelée "Grand Frère". Ce Grand Frère est ensuite dégradé vers une résolution similaire à celle que l'on retrouve de nos jours dans les analyses objectives globales et/ou dans les modèles globaux de climat (MGC). Cela est effectué en enlevant les petites échelles

présentent dans la simulation Grand Frère. Les champs résultants sont alors utilisés comme données pour piloter un MRC (appelé “Petit Frère”), lequel est intégré à la même haute résolution que celle du Grand Frère, mais sur une sous-région de celui-ci. Les statistiques climatiques du Petit Frère sont alors comparées à celles de la simulation du Grand Frère, et cela sur la région couvrant le domaine du Petit Frère. Les différences entre les deux climats peuvent alors être attribuées sans ambiguïté aux erreurs associées à la technique de raffinement dynamique, et non aux erreurs des modèles ou aux limitations des observations réelles. Les résultats pour un mois de février montrent que le MRC canadien, utilisant un facteur de saut de résolution spatial de 6 entre le modèle et ses conditions frontières latérales, et un intervalle de pilotage de 3 heures, est capable de réussir le test de l’EGF. Ceci démontre la fiabilité de l’approche de pilotage unidirectionnel.

Dans la troisième et dernière partie de cette thèse, l’EGF est employée pour examiner la sensibilité d’un MRC aux sauts de résolution spatiale et à la fréquence de mise à jour des conditions frontières latérales. Il est montré qu’un saut de résolution spatial de 12, ainsi qu’une fréquence de mise à jour entre deux fois (aux 12 heures) et quatre fois (aux 6 heures) par jour, sont les limites pour lesquelles un MRC de 45 km de résolution produit des résultats acceptables.

REMERCIEMENTS
(ACKNOWLEDGEMENTS)

J'aimerais remercier chaleureusement mes deux superviseurs, *professeur René Laprise* et *Docteur Jean Côté*, pour m'avoir guidé, supporté et encouragé tout au long de ce travail. Plus précisément, je suis très reconnaissant au *professeur René Laprise* de m'avoir initié à la modélisation régionale du climat, ainsi qu'il l'avait fait dix ans auparavant pour la modélisation globale.

Je remercie également *Docteur Daniel Caya* qui, en tant que directeur du projet MRC, expert et ami, m'a supporté et aidé sur plusieurs aspects reliés à mon passage parmi le groupe de modélisation régionale du climat de l'UQAM. J'en profite pour remercier tout le groupe *MRC* pour son support technique et amical.

Un gros merci au *Docteur Bernard Dugas*, seul modélisateur climatique au Service Météorologique du Canada à Dorval. Son aide précieuse pour l'utilisation de la librairie de diagnostique climatique qu'il a mise au point a été d'un grand secours, tout comme nos nombreuses discussions.

Merci au *Docteur Ramón de Elía*, stagiaire post-doctoral dans l'équipe MRC, pour les discussions sur les expériences Big-Brother, et pour son support moral.

Ce travail a été rendu possible grâce à une subvention du département de l'énergie des États-Unis (US-DOE) via son programme *Climate Change Prediction Program (CCPP)*, ainsi qu'au soutien financier du groupe *MRC* de l'UQAM. Je me dois également de remercier mon employeur, le *Service Météorologique du Canada*, pour m'avoir accordé un congé d'étude de trois ans afin d'effectuer cette recherche.

Finalement, je remercie de tout mon cœur ma conjointe *Catherine*, ainsi que mes enfants *Nicolas et Valérie*, pour m'avoir encouragé et soutenu au cours de ces trois années!

TABLE OF CONTENTS

LIST OF FIGURES

Chapter III, Paper II

Chapter IV, Paper III

LIST OF TABLES

Chapter III, Paper II

Chapter IV, Paper III

LIST OF ACRONYMS

AGCM	Atmospheric General Circulation Model
BBE	Big-Brother Experiment
CAS	Commission for Atmospheric Sciences
CCPP	Climate Change Prediction Program
CRCM	Canadian Regional Climate Model
DCT	Discrete Cosine Transform
DFT	Discrete Fourier Transform
ECMWF	European Centre for Medium-Range Weather Forecasts
FFT	Fast Fourier Transform
GCM	Global Climate Model
GMT	Greenwich Mean Time
IC	Initial Conditions
IPCC	Intergovernmental Panel on Climate Change
JPEG	Joint Pictures Expert Group
JSC	Joint Scientific Committee
KE	Kenetic Energy
LAM	Limited-area Model
LBC	Lateral Boundary Conditions
LLNL	Lawrence Livermore National Laboratory
MPEG	Moving Picture Experts Group
MPI	Max-Planck-Institut für Meteorologie
NCAR	National Center for Atmospheric Research

NCEP	National Centers for Environmental Prediction
OA	Objective Analysis
OGCM	Ocean General Circulation Model
PIRCS	Project to Intercompare Regional Climate Simulations
RCM	Regional Climate Model
UQAM	Université du Québec à Montréal
USDOE	United State Department of Energy
WGNE	Working Group on Numerical Experimentation
WRCP	World Climate Research Programme

STATEMENT OF ORIGINALITY

The contributions to original knowledge are as follows:

- For the first time, a rigorous and unambiguous experimental framework using a perfect-prognosis approach has been employed for demonstrating the downscaling ability of a one-way nested regional climate model (RCM). This work is in response to concerns expressed by the Working Group on Numerical Experimentation (WGNE) about the reliability of one-way nested RCMs (CAS/JSC WGNE, 1999 and 2000). Within the proposed framework, it has been shown that the one-way nesting strategy can accurately simulate fine-scale climate features when driven by large-scale information with resolution similar to current global climate model (GCM) or global objective analyses.

- For the first time, a rigorous study as been done for examining the sensitivity of an RCM to the *spatial* resolution and *temporal* updating frequency of the lateral boundary conditions (LBC). It has been showed that a spatial resolution jump up to 12 and an update interval between 6 and 12 hours are to upper limits that can be employed for nesting a 45-km RCM.

- For the first time, summary diagrams called Taylor diagrams have been used for assessing the performance of an RCM in terms of the stationary and transient climate components, for the total fields as well as for their fine-scale components. Using these diagrams, it has been shown that the transient fine scales are more sensitive to the lack of resolution of LBC than the stationary fine scales; the latter being forced by stationary surface forcings, are therefore weakly dependent of the LBC resolution; while the former are affected by the contamination of entering weather systems due to the imperfect LBC resolution.

- For the first time, a spectral decomposition technique suitable for limited-area domains and using the discrete cosine transform (DCT) has been developed and applied successfully for producing power spectra and for extracting mesoscale features.

CONTRIBUTION OF AUTHORS

Papers on which I am first author (part of this thesis):

1) *"Spectral Decomposition of Two-dimensional Atmospheric Fields on Limited-area Domains using the Discrete Cosine Transform (DCT)"*

by Denis, Côté and Laprise

Dr. J. Côté suggested the use of the DCT and provided the low-level FORTRAN code. I designed and wrote the programs that compute the power spectrum analysis and the spectral filtering using a 2D DCT as well as a 2D standard FFT. The basic test cases have been built with the help of Prof. R. Laprise, who also participated in interpreting the results. I wrote the paper and Prof. R. Laprise made some suggestions.

I presented the results at the Canadian Meteorological and Oceanographic Society (CMOS) congress in May 2000.

2) *"Downscaling Ability of One-way Nested regional Climate Models: The Big-Brother Experiment"*

by Denis, Laprise, Caya and Côté

Prof. R. Laprise suggested the perfect-prognosis approach as the experimental protocol. I constructed and performed all the numerical experiments and their diagnostic analyses. I wrote the paper and Prof. R. Laprise, Drs D. Caya and J. Côté participated in discussions for the interpretation of the results and also commented upon the manuscript.

I presented the results at a Joint Workshop on Regional Climate Modeling at UQAM in June 2000 and Prof. René Laprise made a presentation on my behalf at the Climate Change Prediction Program meeting in March 2000.

3) *"Sensitivity of a Regional Climate Model to the Spatial Resolution and temporal Updating Frequency of the Lateral Boundary Conditions"*

by Denis, Laprise and Caya

I designed and performed all the experiments as well as the analysis of the results. Prof. R. Laprise and Dr D. Caya have contributed in interpreting the results. I wrote the paper and Prof. R. Laprise and Dr. D. Caya commented upon.

Prof. René Laprise presented the results at a WGNE workshop on regional climate modeling in April 2001 and Dr. D. Caya presented them at the CMOS congress in May 2001.

Papers on which I am simply co-author (not presented in this thesis):

1) "*Predictability in a nested limited-area model*"

by Laprise, Ravi Varma, Denis, Caya, and Zawadzki

I performed part of the numerical experiments as well as their analysis. I participated in the discussions of the results and also commented upon the manuscript.

2) "*Scale-dependent predictability of a limited-area model*"

by de Elía, Laprise and Denis

I provided part of the computer programs and scripts required by the experimental framework. I participated in the discussions of the results and I also commented upon the manuscript.

Chapter I

Introduction

Climate change and its impacts on the environment have never been so much "à la mode" than during the last few years. As the evidence of global warming is beginning to emerge from the climate natural variability, Canadians have begun to link regional weather catastrophes, such as the winter '98 Montreal Ice Storm and the summer '97 Saguenay flood, to anthropological climate change.

Enormous progress has been done by the scientific community during the last decade to master the issue of climate change as can be seen in the IPCC reports (Houghton et al., 1990, 1996 and 2001). Because of its nature, climate change is a global phenomenon and this is the reason why a lot of effort has been done at that scale recently. An example of this is the coupling of atmospheric and ocean general circulation models (AGCM and OGCM) (e.g. Flato et al. (2000)). Because of the tremendous computational cost of running these global models, only relatively coarse resolutions can be used to produce climate simulations on present supercomputers. These simulations capture reasonably well the large-scale climate features but still lack details at the regional climate scales where the type of catastrophes mentioned above strikes.

To circumvent the prohibitive cost of computation on uniform and high-resolution grid of global models, some strategies have recently appeared. One of them, called "One-way nesting" is to use a high-resolution computational grid over a small domain nested at its boundaries by data provided by a global low-resolution model or global objective analyses. The use of this strategy for regional climate modelling has started to be employed a decade ago with the seminal work of Dickinson et al. (1989) and Giorgi (1990). Even though one-way nested regional climate models (RCM) have now become widely used and proved to be a workable approach for climate downscaling (Giorgi and Mearns, 1999), skepticism has been expressed concerning the ability of such technique to adequately simulate regional climates (CAS/JSC WGNE, 1999 and 2000). There are a number of issues that are related to the one-way nesting which, as the name implies, does not allow feedback between the RCM and its driving data (simulated or objective analyses). For example, the impact of the spatial resolution jump between the driving data and the nested model, as well as the robustness of the simulated climate to updating frequency of the lateral boundary conditions (LBC) are two important issues that have not been rigorously studied yet.

The RCM's fine-scale features are thought to be the added values over conventional low-resolution Global Climate Models (GCMs). It is therefore natural to ask this fundamental question:

"Can a one-way nested RCM accurately simulate fine-scale climate features when driven by large-scale information only?"

The major problem that it is faced when one tries to answer such a question is the lack of high-resolution climatological datasets available for verification. Furthermore any differences that would be found between the simulated climate and the verification dataset would be difficult to attribute to either the nesting mechanism or, to the model errors (dynamics or physics components). With the objective to circumvent this limitation, a perfect-prognosis experimental framework, called the Big-Brother Experiment (BBE), has been developed and employed in this thesis for evaluating the downscaling ability of a one-way nesting RCM. In a nut shell, the BBE consists in first establishing a reference virtual-reality climate from an RCM simulation using a large and high-resolution domain: this simulation is called the Big Brother. This big-brother simulation is then degraded toward the resolution of today's global objective analyses (OA) and/or general circulation models (GCM) by removing (filtering) the short scales. The resulting fields are then used as nesting data to drive an RCM (called the Little Brother) which is integrated at the same high-resolution as the Big Brother, but over a sub-area of the big-brother domain. The climate statistics of the Little Brother are then compared with those of the big-brother simulation over the little-brother domain. Differences between the two climates can thus be unambiguously attributed to errors associated with the dynamical downscaling technique, and not to model errors nor to observation limitations.

This thesis is composed of 3 papers, organized as follows: the first paper concerns a spectral tool that has been developed and employed throughout this work for 1) degrading the LBC spatial resolution as well as the initial conditions, 2) extracting the fine-scale features from the total fields for subsequent comparison and diagnostics and 3) producing power spectra. The motivation for developing this specific tool was, for instance, that it provides an excellent control on the filtering response in term of scales; this particularity important for the resolution degradation of the LBC in the BBE, and was not available from most current filters.

In the second paper (Chapter III), a substantial introduction including a comprehensive literature review concerning the most important RCM issues is given first. Secondly, the details of the BBE protocol are exposed. A winter-month simulation using this BBE protocol is then performed and analysed.

The last paper (Chapter IV) is devoted to the investigation of the sensitivity of an RCM to the *spatial* resolution and t*emporal* update frequency of the LBC. This investigation makes use of the BBE protocol to highlight their respective impact as well as their combined effect. In addition, the one-February month experiment performed in the first BBE paper is extended to February month of three other years; this extension shall permit to evaluate the robustness of the results found in the first BBE paper.

Conclusions concerning the BBE are included in the last two papers (Chapter III & IV) but they are summarized in Chapter 5 with supplemental discussions and suggestion for future work.

Chapter II

Spectral Decomposition of Two-dimensional Atmospheric Fields on Limited-are Domains Using the Discrete Cosine Transform (DCT)

In this chapter, a new spectral decomposition tool suitable for limited-area domains is developed and tested. The motivation for developing this tool came from a need of accurately analysing and extracting specific scales out of the RCM simulations since our work concentrates on the downscaling ability of the RCM; i.e. its fines-scale features. Therefore, the work done in this chapter aims at equipping us with the best possible tool for using and analysing the results of our Big-Brother Experiments in the two next papers.

Spectral Decomposition of Two-dimensional Atmospheric Fields on Limited-area Domains Using the Discrete Cosine Transform (DCT)

Bertrand Denis[*,+,#],
Jean Côté[#] and
René Laprise[*]

[*] *Département des sciences de la Terre et de l'Atmosphère, Université du Québec à Montréal, Montréal (UQAM), Québec, Canada*

[+] *Department of Atmospheric and Oceanic Sciences, McGill University, Montréal, Québec, Canada*

[#] *Recherche en Prévision Numérique, Meteorological Service of Canada, Dorval, Québec, Canada*

Submitted to *Monthly Weather Review*

25 July 2001

Corresponding author address:

Bertrand Denis
Recherche en Prévision Numérique
2121 Route Transcanadienne
Dorval, Québec
Canada
H9P 1J3

Email Bertrand.Denis@ec.gc.ca

Abstract

For most atmospheric fields, the larger part of the spatial variance is contained in the planetary scales. When examined over a limited area, these atmospheric fields exhibit an aperiodic structure, with large trends across the domain. Trying to use a standard (periodic) Fourier transform on regional domains results in the aliasing of large-scale variance into shorter scales, thus destroying all usefulness of spectra at large wavenumbers. With the objective of solving this particular problem, we have evaluated and adopted a spectral transform called the Discrete Cosine Transform (DCT). The DCT is a widely used transform for compression of digital images such as MPEG and JPEG, but its use for atmospheric spectral analysis has not yet received widespread attention.

We first show how the DCT can be employed for producing power spectra from two-dimensional atmospheric fields and how this technique compares favorably with the more conventional technique that consists of detrending the data before applying a periodic Fourier transform. Secondly, we show that the DCT can be used advantageously for extracting information at specific spatial scales by spectrally filtering the atmospheric fields. Examples of applications using data produced by a Regional Climate Model are displayed. In particular, we show how the 2D-DCT spectral decomposition is successfully used for calculating kinetic energy spectra and for separating mesoscale features from large scales.

1. Introduction

Spectral analysis techniques of global atmospheric fields in the horizontal have been used for several years for diagnostic purposes (e.g. Boer and Shepherd, 1983; Trenberth and Solomon, 1993) as well as for the numerical simulation of the atmosphere (e.g. Bourke, 1972; Daley et al., 1976). However, their popularity as diagnostics tools has been until now largely circumscribed to applications whose domain covers the sphere. On such a domain, a spectral decomposition in terms of triangularly truncated spherical harmonics is natural and very convenient for many reasons. For instance, one of the two transforms required for obtaining the spectral coefficients is the very well known discrete Fourier transform (DFT); this transform is well suited for the global atmosphere because its basis functions are periodic, as are the atmospheric fields, on latitude circles. Moreover, fast numerical algorithms for computing the DFT (called FFT for Fast Fourier Transform) are widely available.

Spectral analysis of atmospheric fields on limited-area grids using Fourier transforms is less popular for two reasons. First, fields on such grids are generally aperiodic and are, in most cases, dominated by large-scale features whose wavelengths are greater than the domain size. To represent such fields with periodic Fourier basis functions, Fourier coefficients corresponding to the high wavenumbers are highly solicited for matching the boundary conditions. As an example, let us consider Fig. 1, which shows a winter snapshot of the 925-hPa specific humidity taken from a simulation produced by the Canadian Regional Climate Model (CRCM) (see Caya and Laprise, 1999, for the model's description). As can be seen, this field contains variance at many scales but is largely dominated by an East-West gradient or trend. To quantify how much information or power is present in the different spatial scales we need to compute its variance spectrum. The solid curve on Fig. 2 shows the spectrum computed with the direct use of the periodic Fourier transform without any prior modification of the field of Fig. 1. We see that this spectrum has a tail that undergoes an upward distortion. This is caused by the aliasing or projection of the large-scale trend on the high-wavenumber components. This distorted spectrum is therefore misleading and it is not representative of the variance inside the domain since a considerable part of it comes from the lateral boundaries and not from the field in general.

To circumvent these deficiencies, Errico (1985) used a method which consists in pre-processing the field to make it periodic by removing its linear trend before the application of a two-dimensional (2D) DFT (detrending-DFT method hereafter). The linear trend is calculated from the difference between the first and last gridpoint field values along each row and column of the grid. Fig. 3 shows the result of detrending the original field of Fig. 1. The benefit of this detrending technique is easily seen in Fig. 2 by comparing the tail of the new spectrum produced by the detrending-DFT method (dashed curve) with the original spectrum tail (solid curve). A side effect of the detrending is the removal of the large-scale gradient across the limited domain as seen in Fig. 3, which affects the large-scale components of the spectrum (Fig. 2). Another side effect of this technique is the pattern of lines generated by the linear detrending as can be seen in Fig. 3. Spectra computed from such massaged fields are sometimes questionable. As mentioned by Errico (1985; 1987) himself, this technique should not be used for fields that are noisier at their boundaries than in the interior of the domain.

Another technique, which is frequently employed for spectral analysis of time series, is the application of a weighting function on the physical field prior to the DFT. This technique, called "windowing", consists in multiplying the physical field by a weighting field of the same dimension but with values equal to unity in the central sub-domain and diminishing to zero when approaching the boundaries. The weighting function used to make the transition from the central sub-domain to the boundaries is often of cosine or Gaussian form. Examples of windowing with 2D spatial atmospheric fields can be found in Turner (1994) and Salvador et al. (1999). These techniques are to some extent similar to that of the detrending-DFT method because they massage the field at or near the boundaries prior to the application of the DFT. But the windowing technique is softer and does not generate a spurious pattern of lines. Although effective for removing the major part of the distortion of the spectrum tail, the application of such windows may not be desirable. In effect, it would modify the spectrum of an already periodic field. Such windowing technique is only appropriate for large-dimension domains, a criterion seldom met by regional climate models.

This paper explores the use of a special type of transform suitable for spectral analysis of data on a limited area. That transform is called the DCT (for Discrete Cosine Transform) and is the core of some data-compression algorithms for digital images. The remainder of this document is organized as follows: Section 2 includes definitions of the direct and inverse DCT, a study of its properties using basic test cases, and a comparison with the detrending-DFT method. Section 3 provides some examples of practical applications including kinetic energy spectra and spectral filtering. The performance, limitations, and usefulness of the DCT for atmospheric applications are discussed in Section 4.

2. The Discrete Cosine Transform (DCT) and power spectra

a. DCT definition

Besides the detrending/windowing techniques, there is a simple way to cure the problem of aperiodic boundary conditions when discrete Fourier-type of transforms are employed. It consists in making periodic the field to be analysed by a symmetrisation process. This process involves simply taking a mirror image of the original function prior to the application of the Fourier transform. It can be shown that this procedure leads to a special Fourier transform called the Discrete Cosine Transform (DCT), first introduced by Ahmed et al. (1974) for digital image processing purposes.

A mathematical derivation of the 1D and 2D-DCT, using the mirror effect, can be found in the Appendix. Other derivations can also be found in Ahmed et al. (1974) and in textbooks dedicated to digital image processing. The DCT has become very popular in the field of image processing (Pratt, 1991; Gonzalez and Woods, 1992) and forms the core of digital image compression algorithms such as those of JPEG and MPEG formats (Pennebaker and Mitchell, 1993). This is due to the capacity of the DCT to treat aperiodic fields while producing spectra where the variance is concentrated in the low-wavenumber components. Thus, only a small number of spectral coefficients are required to retain the major part of the visual information of the image. The compression algorithm consists in preserving only these most important spectral coefficients, therefore reducing the size of the image in terms of computer memory without a dramatic loss of the image quality. There is an important difference between the compression algorithms mentioned above and the application of the DCT in this paper. Here, the DCT shall be applied on grids of the order of 100 by 100 grid points, but in usual image processing the DCT is applied on blocks of 8 by 8 grid points (pixels) forming images of the order of 1000 by 1000 grid points (pixels).

For a two-dimensional field *f (i,j)* of N_i by N_j grid points, the direct and inverse DCT are respectively defined as,

$$F(m,n) = \beta(m)\beta(n)\sum_{i=0}^{i=N_i-1}\sum_{j=0}^{j=N_j-1} f(i,j)\cos\left[\pi m\frac{(i+1/2)}{N_i}\right]\cos\left[\pi n\frac{(j+1/2)}{N_j}\right], \quad (1)$$

and

$$f(i,j) = \sum_{m=0}^{m=N_i-1}\sum_{n=0}^{n=N_j-1} \beta(m)\beta(n)F(m,n)\cos\left[\pi m\frac{(i+1/2)}{N_i}\right]\cos\left[\pi n\frac{(j+1/2)}{N_j}\right], \quad (2)$$

$$\text{with} \quad \beta(m) = \begin{cases} \sqrt{\dfrac{1}{N_i}} & m = 0 \\ \sqrt{\dfrac{2}{N_i}} & m = 1,2,\ldots,N_i-1 \end{cases} \quad \text{and} \quad \beta(n) = \begin{cases} \sqrt{\dfrac{1}{N_j}} & n = 0 \\ \sqrt{\dfrac{2}{N_j}} & n = 1,2,\ldots,N_j-1 \end{cases}. \quad (3)$$

f (i,j) is the field value at gridpoint integer numbers *(i, j)*, and *F(m, n)* is the spectral coefficient corresponding to the *(m,n)* adimensional wavenumbers. A 2D-DCT applied to a physical field *f (i,j)* of N_i by N_j values produces an N_i by N_j array of *F(m, n)* real spectral coefficients.

b. Power spectra construction from the DCT

Now that the 2D-DCT has been defined, let see how it can be used to compute power spectra from two-dimensional meteorological fields. In two dimensions, the total variance is defined as

$$\sigma^2 = \frac{1}{N_i}\frac{1}{N_j}\sum_{i=0}^{i=N_i-1}\sum_{j=0}^{j=N_j-1}\left(f(i,j)-\langle f\rangle\right)^2 \tag{4}$$

with $\langle f \rangle$ the domain average. The total variance can also be computed from the spectral coefficients:

$$\sigma^2 = \sum_{\substack{n=0 \\ (m,n)\neq(0,0)}}^{N_i-1}\sum_{m=0}^{N_j-1}\sigma^2(m,n) \quad \text{with} \quad \sigma^2(m,n) = \frac{F^2(m,n)}{N_i N_j} \tag{5}$$

and the domain average $\langle f \rangle$ from

$$\langle f \rangle = \sqrt{\sigma^2(0,0)} = \frac{F(0,0)}{\sqrt{N_i}\sqrt{N_j}}. \tag{6}$$

We see from (5) that the total variance can be decomposed into spectral variance components forming an $N_i x N_j$ array (excluding the element (0,0)). Figure 4a shows an example of a 2D spectral variance $\sigma^2(m,n)$ array computed by applying the 2D-DCT of the humidity field shown on Fig. 1. Figure 4b is a monthly mean of such arrays.

Since our goal in generating spectra is to evaluate the variance of 2D fields as a function of spatial scales, each two-dimensional wavenumber pair (*m,n*) needs to be associated with a single-scale parameter, namely a wavelength λ. For a square domain, $N_i = N_j = N$ and we have

$$\lambda = \frac{2N\Delta}{k} \tag{7}$$

where Δ is the gridpoint spacing and k the 2D wavenumber defined as

$$k = \sqrt{m^2 + n^2}\,. \tag{8}$$

In the variance arrays of Fig. 4, a given k corresponds to a circle of radius k having for origin the element (m=0, n=0). Each element (m,n) on a given circle has the same wavenumber k. It can be seen from these examples, for which the grid is a square and $\Delta x = \Delta y$, that the power decreases quasi-radially from the largest scale (small wavenumbers) components to the smallest scale (large wavenumbers) components. This is particularly evident for the monthly mean of variance arrays (Fig. 4b) and suggests that the horizontal humidity field has a quasi-isotropic turbulent nature since the variance components depend only on the magnitude of the 2D wavenumber k and not its direction.

There are a few points, specific to the DCT, that are important to note concerning λ. Firstly, the lowest mode (k=1) supported along one axis of the domain corresponds to a half cosine wave (see Fig. A2). Therefore, from (7) the spectral variance of the data that projects onto this mode can be associated to a wavelength of twice the length of the domain along this axis,

$$\lambda_{\max} = 2N\Delta\,. \tag{9}$$

This is a direct consequence of the mirror effect implicit in the DCT. This lowest mode absorbs most of the large-scale trend existing in the field, and could be excluded from the spectra if desired, in order that the next largest mode represented in the spectra would correspond to a full cosine wave.

The second point worth noting is that the highest mode along an axis (k=N-1) corresponds to

$$\lambda_{\min} = 2\Delta \frac{N}{N-1}, \tag{10}$$

which approaches the Nyquist period (2Δ) for sufficiently large N. Thus for simplicity, the variance of the highest wavenumber displayed in the spectra can be associated with a wavelength of nearly twice the gridpoint spacing. To include the possibility of analyzing data on rectangular domains in addition to square domains, Eqs. (7) and (8) are generalized as follows:

$$\lambda = \frac{2\Delta}{\alpha} \tag{11}$$

$$\alpha = \sqrt{\frac{m^2}{N_i^2} + \frac{n^2}{N_j^2}}. \tag{12}$$

where α is a normalized 2D wavenumber. Equation (12) can be seen as a normalization of the m and n wavenumber axes leading to an elliptic shape. With these new definitions, the variance components that should be retained for constructing a spectrum are those for which $0 < \alpha < 1$. More specifically, the variance contributions of the *F(m,n)* coefficients need to be binned accordingly to bands of α. In the case of a square domain, each binning is accomplished by adding all spectral variances existing inside a ring formed by two circles centered on the lower-left corner of the variance array and having specific radii of α and $\alpha + \Delta\alpha$, respectively. The thickness ($\Delta\alpha$) of the ring defines a specific wavenumber band and, consequently, waves of specific wavelengths. If the domain is rectangular, the region of the variance array contributing to a specific wavelength band is the region between two ellipses. The limiting values of α for each wavelength band are determined as follows:

$$\alpha(k) = \frac{k}{\min(N_i, N_j)} \tag{13}$$

and

$$\alpha(k) + \Delta\alpha(k) = \frac{k+1}{\min(N_i, N_j)} \tag{14}$$

with $k = \{1, 2, 3 \ldots \min(N_i - 1, N_j - 1\}$. For the particular case of a rectangular domain, the minimum operators ensure that the number of wavenumber bands is no larger than the number of wavenumbers of any individual variance array axis.

The algorithm for variance binning is as follow:

1- For a given *k*, determine the limits of the contributing band defined by $\alpha(k)$ and $\alpha(k) + \Delta\alpha(k)$ using (13) and (14);

2- For each element in the variance array, compute α using (12) and add its contribution to the variance $\sigma^2(\alpha(k))$ if $\alpha(k) \leq \alpha < \alpha(k) + \Delta\alpha(k)$;

3- Repeat the procedure to sweep all $k = \{1, 2, 3 \ldots \min(N_i - 1, N_j - 1)\}$.

The wavelengths corresponding to each k can be computed from Eqs. (13), (14) and (11). The result of this procedure is a discrete variance distribution as a function of wavenumber k (or normalized wavenumber α) or wavelength λ. It is important to note that this construction of spectra, which is based on physical scales (true wavelength bands) through the use of normalized wavenumbers, is similar to that used in Van Tuyl and Errico

(1989) but is different from Errico (1985), who used wavenumber bands defined by circles instead of ellipses for his rectangular domain.

The procedure described up to now can be applied similarly to variance arrays produced by a standard real 2D discrete Fourier transform (DFT). But there is a fundamental difference between an array of spectral coefficients produced by a DCT versus that produced by a DFT. In the 1D DFT case for instance, each complex spectral component for a given wavenumber is composed of two pieces of information: the cosine part and the sine part, or equivalently the amplitude and the phase. In the 1D-DCT case, each real spectral component consists of only cosines but these can be of full or half wavelength (see Fig. A2). However, the total amount of information is the same in each case. In order to facilitate the comparison of variance spectra produced by the two transforms (DCT and DFT), the consecutive variances $\sigma^2(\alpha(k))$ of the DCT were gathered and summed two by two. The variances are computed as:

$$Var(k) = \begin{cases} \sigma^2(\alpha(2k-1) + \sigma^2(\alpha(2k)) & \text{if DCT} \\ \sigma^2(\alpha(k)) & \text{if DFT} \end{cases}. \tag{15}$$

An alternative gathering for the DCT case could also have been employed:

$$Var(k) = \frac{\sigma^2(\alpha(2k-1)}{2} + \sigma^2(\alpha(2k)) + \frac{\sigma^2(\alpha(2k+1)}{2}. \tag{16}$$

c. DCT properties and test cases.

Before using the 2D-DCT for spectral analysis of meteorological fields, we need to make some basic tests for validating its use. First, we will look to a 1D theoretical spectral response using a continuous form and with a known input analytic function. Then, the same analytic input function will be used to test the discrete form (Eqs. (1), (2) and (3)) and the spectra produced using the procedure explained in the previous Section. We will close this Section with tests that will help to evaluate the spectral analysing performance of the DCT when applied to input functions (including aperiodic ones) for which the power spectra are specified beforehand.

In order to understand how the DCT interprets a given input function in terms of power as a function of scales, let us first consider this analytic input function:

$$h(x) = \cos\left(px + \phi\right), \tag{17}$$

where $0 \leq x \leq \pi$, p is not necessarily an integer, and ϕ is a phase shift. If we use a continuous form of the 1D-DCT and we apply it to $h(x)$:

$$\sigma^2(k, p, \phi) = \left\{ \frac{1}{\pi} \int_0^{\pi} \cos(px + \phi)\cos(kx)dx \right\}^2, \tag{18}$$

we get :

$$\sigma^2(k,p,\phi) = \begin{cases} \left\{ \dfrac{(k-p)\sin(\pi p + \pi k + \phi) - (k+p)\sin(\pi p - \pi k + \phi) + 2p\sin(\phi)}{2\pi(k^2 - p^2)} \right\}^2 & \text{for } k \neq p \\ \left\{ \dfrac{\sin(2\pi k + \phi) - \sin(\phi)}{4\pi k} + \dfrac{\cos(\varphi)}{2} \right\}^2 & \text{for } k = p \end{cases}. \tag{19}$$

Since we are only interested in positive integer values of k, Eq. (19) reduces to:

$$\sigma^2(k,p,\phi) = \begin{cases} \left\{ \dfrac{p\left(\sin(\phi) - (-1)^k \sin(\pi p + \phi)\right)}{\pi\left(k^2 - p^2\right)} \right\}^2 & \text{for } k \neq p \\ \dfrac{\cos(\phi)^2}{4} & \text{for } k = p \end{cases}. \tag{20}$$

There are a couple of points to notice about this equation. Firstly, given an input function with a wavenumber $p \neq k$, the transform responds by returning power at many k wavenumbers. But the k^4 factor in the denominator implies aliasing or "frequency leakage" with a steep slope (-4) for $k > p$. Secondly, the phase shift ϕ also suggests aliasing; there is no provision in the DCT basis functions for a phase shift for a given wavenumber, as there is in those of the DFT.

To understand the implications of these two points let us first consider the case in which there is no phase shift so that the aliasing is generated only by the fact that p is not an integer. In this case, Eq. (20) reduces to

$$\sigma^2(k,p) = \begin{cases} \dfrac{p^2 \sin^2(\pi p)}{\pi^2\left(k^4 - 2k^2 p^2 + p^4\right)} & \text{for } p \text{ not integer} \\ \dfrac{1}{4} & \text{for } p \text{ integer, } k = p \\ 0 & \text{for } p \text{ integer, } k \neq p \end{cases} . \tag{21}$$

Fig. 5 permit the visualization of the aliasing behavior implied by Eq. (21). It displays the power responses as a function of the first 20 integer wavenumbers k and for some selected input wavenumbers p. No two-by-two gathering of variances described by Eq. (15) or (16) has been done. We see that the maximum power (1/4) is reached when $k = p$, but some of the power spreads over other k values when $k \neq p$ due to the aliasing. Maximum aliasing occurs when p is a half integer. Notice that the aliased power decreases rapidly, at a rate of k^{-4}, on the right-hand side of the maxima (for $k > p$).

In the case of an integer wavenumber p, Eq. (20) becomes:

$$\sigma^2(k,p,\phi)=\begin{cases}\dfrac{\cos^2(\phi)}{4} & \text{for } k=p \\ \dfrac{p^2\sin^2(\phi)\left(1-(-1)^{k+p}\right)^2}{\pi^2\left(k^4-2k^2p^2+p^4\right)} & \text{for } k+p \text{ odd} \\ 0 & \text{otherwise}\end{cases}. \tag{22}$$

Equation (22) tells that the power response in the spectrum at $k = p$ is perfect when there is no phase shift, but drops as the phase shift tends to $\pi/2$. Meanwhile, the other components of the spectrum, except for $k + p$ even, receive some power such that the aliasing due to the phase shift also exhibits a k^{-4} power law. Figure 6 illustrates this behavior for an input wavenumber p=3.

Up to this point, we have looked at the basic behavior of the 1D-DCT in an approximated continuous form. The same input function, but discretized and including a ½ gridpoint shift, can be analysed with the discrete form (1D version of Eqs. (1), (2) and (3)). Fig. 7 shows the variance spectra for such an input function having wavenumber p ranging from 6 to 8.2, for different phase shifts (none, $\pi/8$ and $\pi/2$). The discretized 1D domain has 100 grid points. The two-by-two gathering procedure described by the Eq. (16) was used so that the gathered input wavenumber, named pg and displayed on each panel of Fig. 7, varies from 3.0 to 4.1. We see that as the input wavenumber pg increases, the peaks gradually move with it in the wavenumber space, as it should. When the phase shift increases, the peak diminishes but still dominates, which shows how well the 1D-DCT captures the variance present in the input field with a particular wavenumber and phase shift. Finally, the –4 slope predicted from the analysis of the continuous form is still present, except at the extreme end of the spectra where it becomes markedly steeper.

Before applying the DCT to real meteorological cases, we have pushed the validating tests one step further. Since meteorological fields can show a wide continuous range of aperiodicity, we have tested the DCT on synthetic 1D fields having this characteristic. Each field was constructed from a sum of functions similar to that of Eq. (17) and for which each wavenumber and phase shift has a random component. Furthermore, the amplitude of each function contributing to the synthetic field has been scaled to give specific power spectra that were known a priori. The test is designed to evaluate the extent to which the DCT spectral analysis is able to return the correct spectra for aperiodic cases. Figure 8 shows spectra computed from 10,000 synthetic fields having specified spectrum slopes of 0, -1, -2, -3, -4 and -5 on a log-log scale. The spectra have been computed using the 1D-DCT and the 1D DFT for comparison. The gathering procedure of Eq. (16) has been used for the DCT, and will be so used for the rest of the paper. Figs. 8a,c show the results for all cases and Figs. 8b,d show only cases for which the aperiodicity was larger than 3 standard deviations of the field values. It can been seen that the DCT produces reasonable spectra for slopes shallower than –4; for steeper slopes, the aliasing effect discussed previously contaminates the calculated power distribution. On the other hand, the DFT shows a distorted tail for slopes equal to or steeper than –2, especially for strongly aperiodic cases (Figs. 8b,c). Fig. 9 shows the results for positive slopes. In this case, the aliasing appears at the larger scales (small wavenumbers) in both the DCT and DFT. Results are clearly unacceptable for slopes larger than +1. All of these results indicate that the DCT can be safely used to spectrally analyze meteorological fields having spectral slopes between –4 and +1; outside these limits the calculated spectra would be too contaminated by the noise caused by aliasing.

d. Comparison of the DCT and detrending-DFT method

To illustrate to spectral analysis capability of the DCT for 2D real meteorological fields, we show in Fig. 10 the spectra of the humidity field of Fig. 1 using the 2D-DCT, and also the detrending-DFT method proposed by Errico (1985). Given that the field of Fig. 1 is highly aperiodic, the use of the two methods is well motivated. From Fig. 10, we see that both methods removed similarly the distorted tail produced by the direct application of the DFT without detrending.

3. Examples of application of the 2D-DCT.

In this Section, other examples of applications of spectral analyses using the 2D-DCT will be presented. Most of the limited-area fields that will be analysed were simulated by the CRCM.

a. Kinetic energy spectrum

The kinetic energy spectrum is one of the most fundamental spectra to examine in order to understand the dynamical behavior of the atmosphere. At large (global) scales, the stationary (time-mean) component of kinetic energy is known to dominate the flow dynamics (Boer and Shepherd, 1983; Trenberth and Solomon, 1993). On the other hand, the transient kinetic energy component gradually dominates the spectrum at smaller scales. This can be seen in Fig. 11, which shows the vertically integrated kinetic energy spectrum for the total, stationary and transient components, as computed from a set of ECMWF global objective analyses for February 1993. The variance shown is expressed as a function of the total wavenumber N of triangularly truncated spherical harmonic basis functions (up to T213). The total component spectrum exhibits an approximate spectral slope of –3 over an energy cascading sub-range between wavenumber N=10 and N=60. Somewhat unexpectedly, the spectrum gets damped at larger N, due to a reduction of the transient activity of the smallest scales.

Now the 2D-DCT technique is used to produce kinetic energy spectra from the same ECMWF analysis but for a limited-area domain, as opposed to the spectra of Fig. 11 which were produced using spherical harmonics basis functions on the globe. The region covered encompassed a sub-domain of 100x100 grid points, centered over the domain of Fig. 1. The gridpoint spacing is 45 km. Figure 12a shows that the kinetic energy spectra computed using the 2D-DCT exhibits a similar spectral slope behavior to that found in Fig. 11. The spurious tail beyond wavenumber k=24 (λ=187 km; N=213) is an artifact caused by the interpolation of the data from the Gaussian transform grid to the higher-resolution polar-stereographic grid, and should be discarded. Figure 12b shows the corresponding spectra computed from a 45-km gridpoint spacing CRCM simulation of that month (driven by low-resolution NCEP (T32) analyses). Comparing Fig. 12a and 12b, we see that the CRCM gives spectra that are generally similar to those computed from the ECMWF analysis, the difference being that the CRCM transient activities completely dominate the small-scales, even at the extreme end of the spectrum. Finally, Fig. 12c displays the spectra of the total component of the CRCM and the ECMWF. It can be seen that even though the CRCM spectrum is also somewhat damped at its end, it contains more variance than does the ECMWF, probably due to the CRCM's higher resolution.

b. Scale separation using DCT spectral filtering

An objective technique for separating horizontal meteorological fields into different scales can be easily designed based on the DCT. As we saw, the direct application of the 2D-DCT on a physical field produces an array of spectral variances in which the spatial scales are related to the 2D wavenumbers k (e.g. Fig. 4). Low-pass, high-pass or any bandpass filtering can easily be performed by applying a 2D transfer function onto the 2D spectral variance components. This is done by multiplying, element by element, the spectral variance array by a transfer function array with values between 0 and 1. Thereafter, an inverse transform is applied to rebuild the filtered physical field.

The choice of the transfer function is very important. If the cutoff is too abrupt, Gibbs phenomena will appear. Sardeshmukh and Hoskins (1984) showed how this shortcoming may be minimized by choosing a soft cutoff, i.e. a gradually varying transfer function. In this paper, we use a taper that follows a squared cosine. Fig. 13 shows an example of a transfer function, also commonly called the amplitude response of the filter. Even though Fig. 13 shows the transfer function as a function of a unidimensional wavelength, it is applied in the 2D wavenumber space (m,n) with the amplitude response varying radially from the lower-left corner of the spectral variance array. For this low-pass filter, all scales larger than 1000 km are preserved and all scales shorter than 500 km are removed. Fig. 14a shows the results of the application of this filter on the humidity field of Fig. 1. As expected, only the largest-scale features survived the filtering. The small-scale content (Fig.

14b) of the original field can be obtained by subtracting this filtered field from the original field (Fig. 1). We see that the method is effective in extracting the mesoscales from the original field. It is interesting to note that no Gibbs phenomena are apparent as would be the case if we had used the DFT without a taper. In the DFT case, the field (not shown) is largely dominated by Gibbs waves with their maximum amplitudes along the lateral boundaries. These spurious waves are simply the physical representation of the distorted tail seen in the DFT curve in Fig. 2.

For the second example of extraction of mesoscales by filtering, we chose a more difficult case for the DCT. We mentioned that the DCT circumvents the aperiodicity problem of the DFT that generates Gibbs waves. But it is still possible that these spurious Gibbs waves may appear with a periodic field if the slopes (derivatives) of that field are large at the boundaries. In effect, such a field, even though periodic in terms of field values, necessitates high-frequency spectral components to meet these slopes. This is even more apparent when small-scale variances inside the domain are not predominant. To illustrate this effect, let us first look at Fig. 15, which shows a simulated monthly mean mean-sea-level pressure field. As can be seen, this field has little visible small-scale variance because the time averaging procedure removed most of it. Nevertheless, stationary mesoscale features due to surface forcings should be present although they are not easy to see. Fig. 16a shows how spectral filtering using the 2D-DCT isolates the mesoscale components; in this case the filtering has also generated strong Gibbs oscillations that are very visible near the left boundary. An easy way to alleviate this Gibbs problem is to diminish the slopes in the direction normal to the lateral boundaries. Fig. 16b shows how a simple smoothing, applied over only 5 points in normal directions starting from the boundaries, removed the spurious phenomenon while having little impact on the mesoscale features of interest farther inside the domain. It should be noted that this periodicity issue in the slopes at the boundaries is not unique to the DCT but can also be seen with the use of the DFT, even after detrending the input field.

4. Discussion

a. Variance spectra

Methods for avoiding the spectral tail distortion caused by the application of the DFT on atmospheric fields defined on limited-area domains have been the topic of several publications. These include papers (e.g. Errico, 1985; Errico, 1987), appendices of papers (e.g. Barnes, 1986; Van Tuyl and Errico, 1989) and a thesis (Turner, 1994). None of these have shown that the detrending technique was totally satisfactory. In the present paper, we abandoned the DFT in favor of the DCT as a way to solve the distortion problem. After providing the 1D and 2D-DCT definitions and describing how a spectrum can be constructed from the DCT spectral coefficients, the reasons why the DCT can be beneficial for spectral analysis on limited-area domains were investigated methodically in Section 2c. It was shown that, with the DCT, the aliasing caused by aperiodicity (or trend) projects either on the first (lowest mode) half-cosine basis function and/or on smaller scales following approximately a -4 slope. This implies that for atmospheric fields with natural spectral slopes no steeper than -4, the true spectral variance of the field remains above the noise level generated by the aliasing. On the other hand, fields possessing "blue" spectra (positive slopes), have the large-scale portion of the spectrum distorted, but not the small-scale portion. Therefore, it appears (from Figs. 8 and 9) that the use of the DCT for producing spectra is justified for fields having spectral slopes between +1 and –4. Because most of the atmospheric fields have their spectral slopes within this range, the use of the DCT seems appropriated and valuable.

In Section 2d, we saw that, for a low-level simulated specific humidity field, the DCT prevented the occurrence of a spuriously distorted spectrum tail, as did the detrending-DFT method. In effect, the two approaches yielded very similar spectra for the small-scale components. But the detrending-DFT method reduces the spectral variance of the largest scale. This is not surprising since detrending acts as a damping agent on the largest scale present in the physical field.

b. Spectral filtering

The advantage of a spectral filter, such as the one employed in this paper, is that the control on the wavelength band to be filtered can be easily obtained. This is not the case with gridpoint (digital) filters such as a simple moving-averaging-box filter (e.g. Giorgi et al., 1993; Takle et al., 1999), a Shuman filter (Shuman, 1957) or, to some extent, a Barnes filter (see Pauley (1990) for response analyses, and Maddox (1979) and Weygandt (1994) for a scale separation usage of this filter). With gridpoint filters, the scale selection, i.e. the position *and* the sharpness of the amplitude response transition, is difficult to obtain at the same time without sacrificing one for the other. Some high-order digital filters such as those described in Raymond (1989) and Raymond and Gardner (1991) do possess the above control on the amplitude response but they need matrix inversion algorithms because of their implicit nature. No such algorithm is needed for the DCT, and a fast DCT version can be used for the spectral filtering, thus making this approach computationally attractive (see the appendix for references). For the cases presented in this paper, the fast 2D-DCT filter was four times faster than a Shuman filter, which needed at least 100 iterations for removing scales smaller than 500 km. It should be noted that these relative performances may be dependent on the computer architecture.

To further compare spectral and digital filtering, there are two interesting points to note. Firstly, high-order (greater than second order) digital filters can, as spectral filters, create fictitious extrema (Gibbs effects) near strong discontinuities inside the domain unless a special constraint is included in the scheme (e.g. Xue, 2000). For our spectral DCT filtering, a taper was used in the spectral space for attenuating these Gibbs ripples. Secondly, digital filters on limited-area domains necessitate special attention near and at the lateral boundaries. Either the order of the scheme, in the normal direction to the boundaries, must be diminished as the stencil approaches the border, or fictious data has to be extrapolated for the part of the stencil that falls outside the domain. The first option is not optimal since a lower order scheme means a lower scale selective filter and can produce spurious effects deep inside the domain (e.g. Achtemeier, 1986; Pauley, 1990). Raymond (1989) chose the second option in employing a reflecting boundary condition to keep the high order of his filter throughout the domain. Interestingly, this reflecting boundary condition is analogous to the mirror effect implicit in the DCT.

In Section 3b we showed examples of spectral filtering using the DCT. The DFT in conjunction with the detrending method can also be used for scale separation purposes (e.g. Errico, 1985; Van Tuyl and Errico, 1989). However, detrending can introduce fictitious small-scale features especially when the field is noisy at the boundaries. In effect, once the large-scale field has been produced by filtering the detrended field, it needs to be "re-trended" in order to get the real large-scale component of the original field. During this process the small-scale noise created by the detrending is re-introduced into what should be a field containing only large scales. The use of the DCT avoids this shortcoming.

As for other spectral transforms using global (as opposed to local) basis functions, fields that contain few and localized features may be difficult to analyze. This is because they may (and probably will) project variance on many scales when in fact the basis functions were simply not spatially compact enough to be representative of those features. For such particular fields other methods, such as a spatial 2D-wavelet analysis, might be more appropriate since wavelet basis functions are localized in space. The use of 2D-wavelet analysis for atmospheric purposes such as those described in this paper is still in its infancy and studies involving 2D spatial fields are rare. Grotjahn and Castello (2000) reported success in 2D scale separation for sea-level data but not for data at upper levels. Nevertheless, success has been reported in studies of other 2D geophysical fields (e.g. Bergeron et al., 1999) and the investigation of applications to turbulence has begun (Farge, 1992).

c. Other applications

The application of the DCT for the purpose of power spectra production and spectral filtering of 2D atmospheric fields was shown in Section 3. The DCT has also been used for diagnosing the CRCM climate simulations (Denis et al., 2001), and in short-term predictability studies (Laprise et al., 2000; de Elía et al., 2001). The DCT is also used in the revised nesting scheme of the CRCM using nudging of large scales, following the initial work of Biner et al. (2000). The weather radar research group of McGill University is also exploring the use of the DCT in radar applications. Work is in progress for making use of the DCT in a direct numerical solver of a LAM version of the Canadian Global Environmental Model. Finally, it is worth noting that the use of cosine basis functions, although not exactly following the DCT definition presented here, can be found in some limited-area spectral model formulations (e.g. Juang and Kanamitsu, 1994; Cocke and LaRow, 2001).

5. Conclusions

The main objectives of this paper were to introduce and give a broad assessment of the use of the discrete cosine transform (DCT) for spectral decomposition of atmospheric fields on limited-area domains. The principal conclusions that can be drawn are the following:

- Variance spectra constructed with the 2D-DCT
  - avoid the aperiodicity issue encountered with the direct application of the discrete Fourier transform (DFT). In effect, the DCT does not produce the characteristic distorted spectral tails as does the DFT when applied on aperiodic fields.
  - compare favorably with the detrending-DFT method (Errico, 1985), which also removes the distorted spectral tail, but at the price of modifying the spectra throughout the wavenumber range.
  - are reliable only for fields having spectral slopes between –4 to +1.

- Spectral filtering with the 2D-DCT
  - is effective for scale separation purposes such as extraction of mesoscale features.

- can be made very scale selective. A bandpass filter can be easily defined throughout the wavenumber range.
- avoids the Gibbs phenomenon caused by the aperiodicity of the field values at the lateral boundaries but can still produce Gibbs oscillations due to the aperiodicity of the field slopes normal to the boundaries. These latter undesirable oscillations can be largely prevented by applying a simple smoothing near the boundaries before the spectral filtering.

As far as the authors are aware, the use of the DCT for spectral decomposition of two-dimensional atmospheric fields on limited-area domains is novel. This paper tentatively exposed its strengths and limitations but it is through a more widespread usage that its real value will be revealed.

Acknowledgements

This work has been financially supported by funding from the USDOE Climate Change Prediction Program (CCPP) and the UQAM regional climate modelling group. We gratefully acknowledge the Meteorological Service of Canada for granting an education leave to the first author during this study and for providing access to its facilities. We are thankful to the UQAM regional climate modelling staff for their invaluable technical help with the Canadian RCM. Finally, we especially would like to thank Mr. Sébastien Riette for testing and improving the program for making spectra, and also Drs Ramón de Elía, Bernard Dugas and Daniel Caya for stimulating discussions.

Appendix

Derivation of the Discrete Cosine Transform

In this appendix we show that the 1D-DCT can be derived by using a "mirror image" artifice. A visual representation of a 1D-DCT basis function set is also given.

Let $f(i)$ be a real function with $i=0,..,N-1$ known on N the number of grid points. The first step consists in building a periodic function $f_s(i)$ by symmetrizing $f(i)$. This is done by taking the position $i=-1/2$ as a mirror, i.e.:

$$f_s(i)=\begin{cases} f(i) & i\geq 0 \\ f(-1-i) & i<0 \end{cases} \quad \text{with now} \quad i=-N,..,0,..N-1. \tag{A1}$$

The result of this procedure is shown in Fig. A1. Note that the new field has now $2N$ grid points.

The second step consists in applying to this new function a discrete Fourier transform centered on $i=-1/2$:

$$F_s(m)=\frac{1}{2N}\sum_{i=-N}^{i=N-1} f_s(i)\exp\left\{-2\pi \mathrm{i} m\frac{(i+1/2)}{2N}\right\} \tag{A2}$$

where $\mathrm{i}=\sqrt{-1}$ and $F_s(m)$ are the complex Fourier amplitudes. The Eq. (A2) can be rewritten as:

$$F_s(m)=\frac{1}{2N}\sum_{i=-N}^{i=N-1} f_s(i)\cos\left[2\pi m\frac{(i+1/2)}{2N}\right]-\frac{\mathrm{i}}{2N}\sum_{i=-N}^{i=N-1} f_s(i)\sin\left[2\pi m\frac{(i+1/2)}{2N}\right], \tag{A3}$$

By rewriting the summations in two parts, we get:

$$F_s(m) = \frac{1}{2N}\sum_{i=-N}^{i=-1} f_s(i)\cos\left[2\pi m\frac{(i+1/2)}{2N}\right] + \frac{1}{2N}\sum_{i=0}^{i=N-1} f_s(i)\cos\left[2\pi m\frac{(i+1/2)}{2N}\right] - \frac{i}{2N}\sum_{i=-N}^{i=-1} f_s(i)\sin\left[2\pi m\frac{(i+1/2)}{2N}\right] - \frac{i}{2N}\sum_{i=0}^{i=N-1} f_s(i)\sin\left[2\pi m\frac{(i+1/2)}{2N}\right]. \tag{A4}$$

Because $f_s(i)$ is a symmetrical function and the terms involving the sines are anti-symmetric, the two last summations vanish and hence it turns out that the $F_s(m)$ are real. Moreover, also by the property of symmetry, the two first terms are equal. Therefore

$$F_s(m) = \frac{1}{N}\sum_{i=0}^{i=N-1} f_s(i)\cos\left[\pi m\frac{(i+1/2)}{N}\right]. \tag{A5}$$

Since on the interval $i=0,..,N-1$, $f_s(i) = f(i)$, we get:

$$F(m) = \frac{1}{N}\sum_{i=0}^{i=N-1} f(i)\cos\left[\pi m\frac{(i+1/2)}{N}\right]. \tag{A6}$$

Defined this way, we obtain for $m=0$:

$$F(0) = \frac{1}{N}\sum_{i=0}^{i=N-1} f(i), \tag{A7}$$

i.e. the domain average.

The inverse transform is obtained from (A6) by multiplying both sides by $\cos\left[\pi m\frac{(i'+1/2)}{N}\right]$ and summing over m:

$$\sum_{m=-N}^{m=N} F(m)\cos\left[\pi m\frac{(i'+1/2)}{N}\right] = \frac{1}{N}\sum_{m=-N}^{m=N}\sum_{i=0}^{i=N-1} f(i)\cos\left[\pi m\frac{(i+1/2)}{N}\right]\cos\left[\pi m\frac{(i'+1/2)}{N}\right]. \tag{A8}$$

Using the orthogonality property of the cosine terms, the right-hand side reduces to $f(i')$. Therefore,

$$f(i) = \sum_{m=-N}^{m=N} F(m) \cos\left[\pi m \frac{(i+1/2)}{N}\right] \tag{A9}$$

after dropping the primes.

Because $f(i)$ is symmetrical, the amplitudes $F(m)$ must satisfy

$$F(-m) = F(m), \tag{A10}$$

giving

$$f(i) = F(0) + 2\sum_{m=1}^{m=N} F(m) \cos\left[\pi m \frac{(i+1/2)}{N}\right]. \tag{A11}$$

Since for $m = N$ we have

$$\cos\left[\pi m \frac{(i+1/2)}{N}\right] = 0, \tag{A12}$$

the last member can be dropped from the summation of (A11) to give

$$f(i) = F(0) + 2\sum_{m=1}^{m=N-1} F(m) \cos\left[\pi m \frac{(i+1/2)}{N}\right]. \tag{A13}$$

By comparing (A6) and (A13) we see that the transform does not create nor destroy information because there are *N* real values of *f(i)* in the physical space and *N* real values of *F(m)* coefficients in the spectral space.

Equation (A13) can be rewritten as follow:

$$f(i) = \sum_{m=0}^{m=N-1} \alpha(m) F(m) \cos\left[\pi m \frac{(i+1/2)}{N}\right] \tag{A14}$$

with $\alpha(m) = \begin{cases} 1 & m = 0 \\ 2 & m = 1, 2, \ldots, N-1. \end{cases}$

The basis functions

$$\cos\left[\pi m \frac{(i+1/2)}{N}\right] \tag{A15}$$

form a set of independent functions by checking the orthogonality condition:

$$\sum_{i=0}^{i=N-1} \cos\left[\pi m \frac{(i+1/2)}{N}\right] \cos\left[\pi m' \frac{(i+1/2)}{N}\right] = \begin{cases} N & m = m' = 0 \\ \frac{N}{2} & m = m' \neq 0 \\ 0 & m \neq m \end{cases} . \tag{A16}$$

The transform can be made orthonormal by replacing $\alpha(m)$ with:

$$\beta(m) = \begin{cases} \sqrt{\frac{1}{N}} & m = 0 \\ \sqrt{\frac{2}{N}} & m = 1,2,\ldots,N-1 \end{cases} \tag{A17}$$

to get:

$$\sum_{i=0}^{i=N-1} \beta(m)\cos\left[\pi m \frac{(i+1/2)}{N}\right] \beta(m)\cos\left[\pi m' \frac{(i+1/2)}{N}\right] = \begin{cases} 1 & m = m' \\ 0 & m \neq m \end{cases} . \tag{A18}$$

Finally, the direct and inverse transforms in one dimension are written as follows:

$$F(m) = \beta(m) \sum_{i=0}^{i=N-1} f(i)\cos\left[\pi m \frac{(i+1/2)}{N}\right] \tag{A19}$$

$$f(i) = \sum_{m=0}^{m=N-1} \beta(m)F(m)\cos\left[\pi m \frac{(i+1/2)}{N}\right] \tag{A20}$$

with $\beta(m) = \begin{cases} \sqrt{\frac{1}{N}} & m = 0 \\ \sqrt{\frac{2}{N}} & m = 1,2,\ldots,N-1 \end{cases}$

Figure A2 shows the various possible modes of the cosine functions (A15) evaluated at grid points $i=0..N-1$ with $N=8$. We notice that except for mode 0, the values at points 0 and $N-1$ never reach $+1$ or -1. This would not have been the case without the half gridpoint shift in symmetrizing the function as reflected by the $1/2$ term in (A19)-(A20). This is why these equations are sometimes called discrete shifted cosine transforms. The shift is visible in Fig. A2 because the evaluation of the cosine begins at $i=-1/2$ and ends at $i=N-1/2$.

The corresponding transforms of Eqs. (A19)-(A20) for the two-dimensional case (on N_i by N_j grid points) are:

$$F(m,n) = \beta(m)\beta(n) \sum_{i=0}^{i=N_i-1} \sum_{j=0}^{j=N_j-1} f(i,j) \cos\left[\pi m \frac{(i+1/2)}{N_i}\right] \cos\left[\pi n \frac{(j+1/2)}{N_j}\right] \qquad \text{(A21)}$$

$$f(i,j) = \sum_{m=0}^{m=N_i-1} \sum_{n=0}^{n=N_j-1} \beta(m)\beta(n) F(m,n) \cos\left[\pi m \frac{(i+1/2)}{N_i}\right] \cos\left[\pi n \frac{(j+1/2)}{N_j}\right] \qquad \text{(A22)}$$

$$\text{with} \quad \beta(m) = \begin{cases} \sqrt{\dfrac{1}{N_i}} & m=0 \\ \sqrt{\dfrac{2}{N_i}} & m=1,2,\ldots,N_i-1 \end{cases} \quad \text{and} \quad \beta(n) = \begin{cases} \sqrt{\dfrac{1}{N_j}} & n=0 \\ \sqrt{\dfrac{2}{N_j}} & n=1,2,\ldots,N_j-1 \end{cases} . \qquad \text{(A23)}$$

A very useful property is the separability of these two-dimensional transforms. In effect, a 2D transform can be obtained conveniently by the successive application of two 1D transforms. A computationally fast version of the DCT can be built from existing 1D FFT computer code (Press, 1992). But, as for the FFT, it is easy to find DCT code in the public domain on the Internet. Finally, computing and visualization programming environments such as MATLAB (1998) provides readily useable 1D-DCT and 2D-DCT routines.

References

Achtemeier, G. L., 1986: The impact of data boundaries upon a successive corrections objective analysis of limited-area datasets. *Mon. Wea. Rev.*, **114**, 40-49.

Ahmed, N., T. Natarajan, and K. R. Rao, 1974: Discrete Cosine Transform. *IEEE Trans. Computers*, **C-23**, 90-93.

Barnes, L. S., 1986: On the accuracy of omega diagnostic computations. *Mon. Wea. Rev.*, **114**, 1664-1680.

Bergeron, S. Y., A. P. Vincent, D. A. Yuen, J. S. Tranchant, and C. Tchong, 1999: Viewing seismic velocity anomalies with 3-D continuous Gaussian wavelets. *Geophys. Res. Lett.*, **26**, 2311-2314.

Biner, S., D. Caya, R. Laprise, and L. Spacek, 2000: Nesting of RCMs by imposing large scales, 7.3-7.4. In: Research activities in Atmospheric and Oceanic Modelling, WMO/TD - No. 987, Report No. 30.

Boer, G. J., and T. G. Shepherd, 1983: Large-scale two-dimensional turbulence in the atmosphere. *J. Atmos. Sci.*, **40**, 164-184.

Bourke, W., 1972: An efficient one-level primitive equation spectral model. *Mon. Wea. Rev.*, **100**, 683-689.

Caya, D., and R. Laprise, 1999: A semi-implicit semi-Lagrangian regional climate model: The Canadian RCM. *Mon. Wea. Rev.*, **127**, 341-362.

Cocke, S., and T. E. LaRow, 2001: Seasonal predictions using a regional spectral model embedded within a coupled ocean–atmosphere model. *Mon. Wea. Rev.*, **128**, 689–708.

Daley, R., C. Girard, J. Henderson, and I. Simmonds, 1976: Short-term forecasting with a multi-level spectral primitive equation model. *Mon. Wea. Rev.*, 99-134.

de Elía, R., R. Laprise, and B. Denis, 2001: Scale dependent predictability of a limited-area model. *Submited to Mon. Wea. Rev.*

Denis, B., R. Laprise, D. Caya, and J. Côté, 2001: Downscaling ability of one-way nested regional climate models: the big-brother experiment. *To appear in Clim. Dyn.*

Errico, R. M., 1987: A comparison between two limited-area spectral analysis schemes. *Mon. Wea. Rev.*, **115**, 2856-2861.

Errico, R. M., 1985: Spectra computed from a limited-area grid. *Mon. Wea. Rev.*, **113**, 1554-1562.

Farge, M., 1992: Wavelet transforms and their applications to turbulence. *Annu. Rev. Fluid Mech.*, **24**, 395-457.

Giorgi, F., M. R. Marinucci, and G. T. Bates, 1993: Development of a second-generation regional climate model (RegCM2). Part II: Convective processes and assimilation of lateral boundary conditions. *Mon. Wea. Rev.*, **121**, 2814-2832.

Gonzalez, R. C., and R. E. Woods: 1992, *Digital image processing / by Rafael C. Gonzalez, Richard E. Woods*, Addison-Wesley, 716 pp.

Grotjahn, R., and C. Castello, 2000: A study of frontal cyclone surface and 300-hPa geostrophic kinetic energy distribution and scale change. *Mon. Wea. Rev.*, **128**, 2865-2874.

Juang, H.-M. H., and M. Kanamitsu, 1994: The NMC nested regional spectral model. *Mon. Wea. Rev.*, **122**, 3-26.

Laprise, R., M. K. Ravi Varma, B. Denis, D. Caya, and I. Zawadzki, 2000: Predictability in a nested limited-area model. *Mon. Wea. Rev.*, **128**, 4149-4154.

Maddox, R. A., 1979: An objective technique for separating macroscale and mesoscale features in meteorological data. *Mon. Wea. Rev.*, **108**, 1108-1121.

Matlab, 1998: Matlab/The language of Technical Computing, version 5.2, The Mathworks, Inc.

Pauley, P. M., 1990: On the evaluation of boundary errors in the Barnes objective analysis scheme. *Mon. Wea. Rev.*, **118**, 1203-1210.

Pauley, P. M., and X. Wu, 1990: The theoretical, discrete, and actual response of the Barnes objective analysis scheme for one- and two-dimensional fields. *Mon. Wea. Rev.*, **118**, 1145–1164.

Pennebaker, W. B., and J. L. Mitchell, 1993: *JPEG still image data compression standard/ William B. Pennebaker, Joan L. Mitchell*, Van Nostrand Reinhold, 638 pp.

Pratt, W. K., 1991: *Digital image processing / William K. Pratt*, Wiley, 698 pp.

Press, W. H., 1992: *Numerical recipes in FORTRAN: the art of scientific computing*, Cambridge University Press, 963 pp.

Raymond, W. H., 1989: High-order, high-pass implicit filters for evaluating information within finite areas. *Mon. Wea. Rev.*, **117**, 2772-2781.

Raymond, W. H., and A. Gardner, 1991: A review of recursive and implicit filters. *Mon. Wea. Rev.*, **119**, 477-495.

Salvador, R., J. Calbó, and M. M. Millán, 1999: Horizontal grid size selection and its Influence on mesoscale model simulations. *J. Appl. Meteor.*, **38**, 1311–1329.

Sardeshmukh, P. D., and B. J. Hoskins, 1984: Spatial smoothing on the sphere. *Mon. Wea. Rev.*, **112**, 2524-2529.

Shuman, F. G., 1957: Numerical methods in weather prediction: II. Smoothing and filtering. *Mon. Wea. Rev.*, 357-361.

Takle, E. S., W. J. Gutowski, Jr., R. W. Arritt, Z. Pan, C. J. Anderson, R. R. da Silva, D. Caya, S.-C. Chen, F. Giorgi, J. H. Christensen, S.-Y. Hong, H.-M. H. Juang, J. Katzfey, W. M. Lapenta, R. Laprise, G. E. Liston, P. Lopez, J. McGregor, R. A. Pielke, Sr., and

J. O. Roads, 1999: Project to Intercompare Regional Climate Simulations (PIRCS): Description and initial results. *J. Geophys. Res.*, **104**, 19443-19461.

Trenberth, K. E., and A. Solomon, 1993: Implications of global atmospheric spatial spectra for processing and displaying data. *J. Climate*, **6**, 531-545.

Turner, S., 1994: Analyse spectrale des données du modèle régional du climat de l'UQAM: Masters thesis, Université du Québec à Montréal, Sciences de l'Atmosphère, Montréal, 113 pp. [Available from: Département des Sciences de la Terre et de l'Atmosphère, Université du Québec à Montréal, C.P. 8888, Succursale "Centre-Ville," Montreal, PQ, H3C 3P8, Canada.]

Van Tuyl, A. H., and R. M. Errico, 1989: Scale interaction and predictability in a mesoscale model. *Mon. Wea. Rev.*, **117**, 495-517.

Weygandt, S. S., 1994: Quantification of predictive skill for mesoscale and synoptic-scale meteorological features as a function of horizontal grid resolution. *Mon. Wea. Rev.*, **122**, 57-71.

Xue, M., 2000: High-order monotonic numerical diffusion and smoothing. *Mon. Wea. Rev.*, **128**, 2853-2864.

Figures

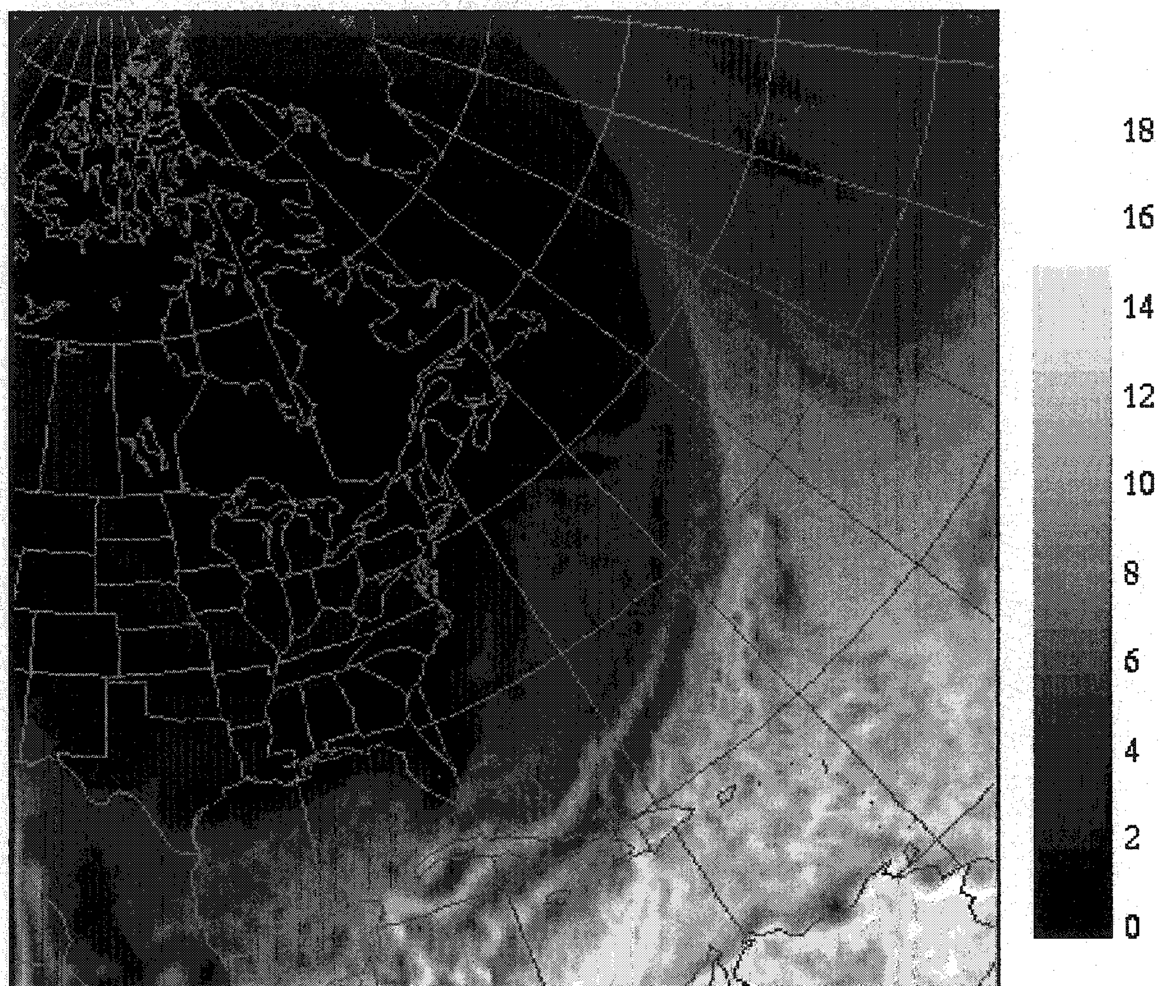

Fig. 1. Instantaneous field of 925-hPa specific humidity (g/kg) simulated by the CRCM in winter. The field is defined on a 180x180 gridpoint domain. The gridpoint spacing is 45 km.

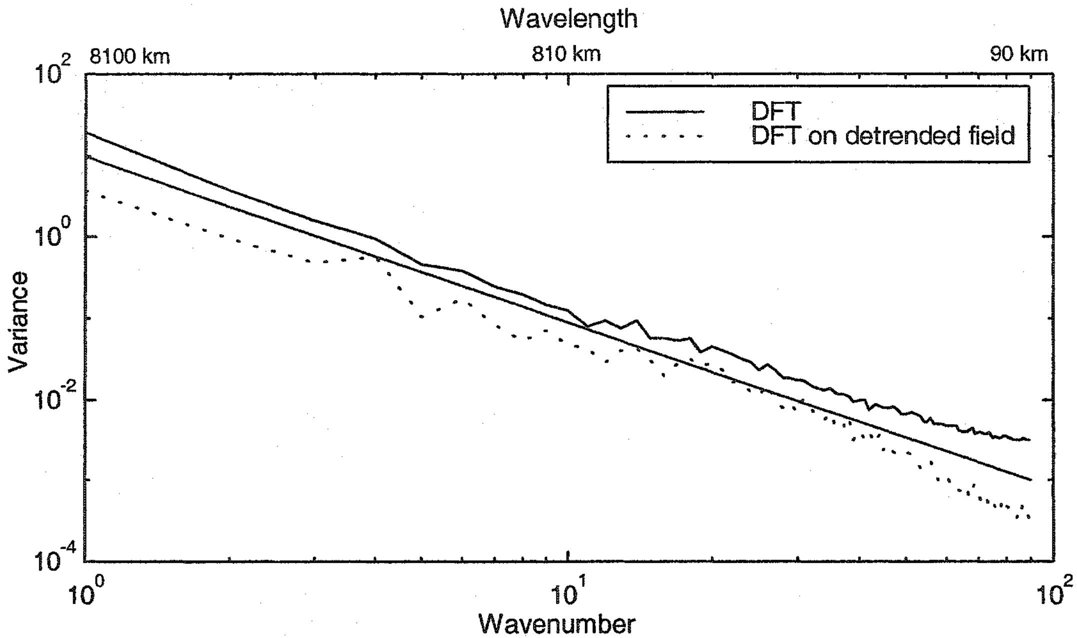

Fig. 2. Variance spectra of the 925-hPa specific humidity field. The solid curve corresponds to the direct use of periodic discrete two-dimensional Fourier transforms (DFT) and the dashed curve corresponds to the application of the DFT after the field has been detrended. The straight line is a reference line with a slope of -2. The units of the variance axis are $(g/kg)^2$.

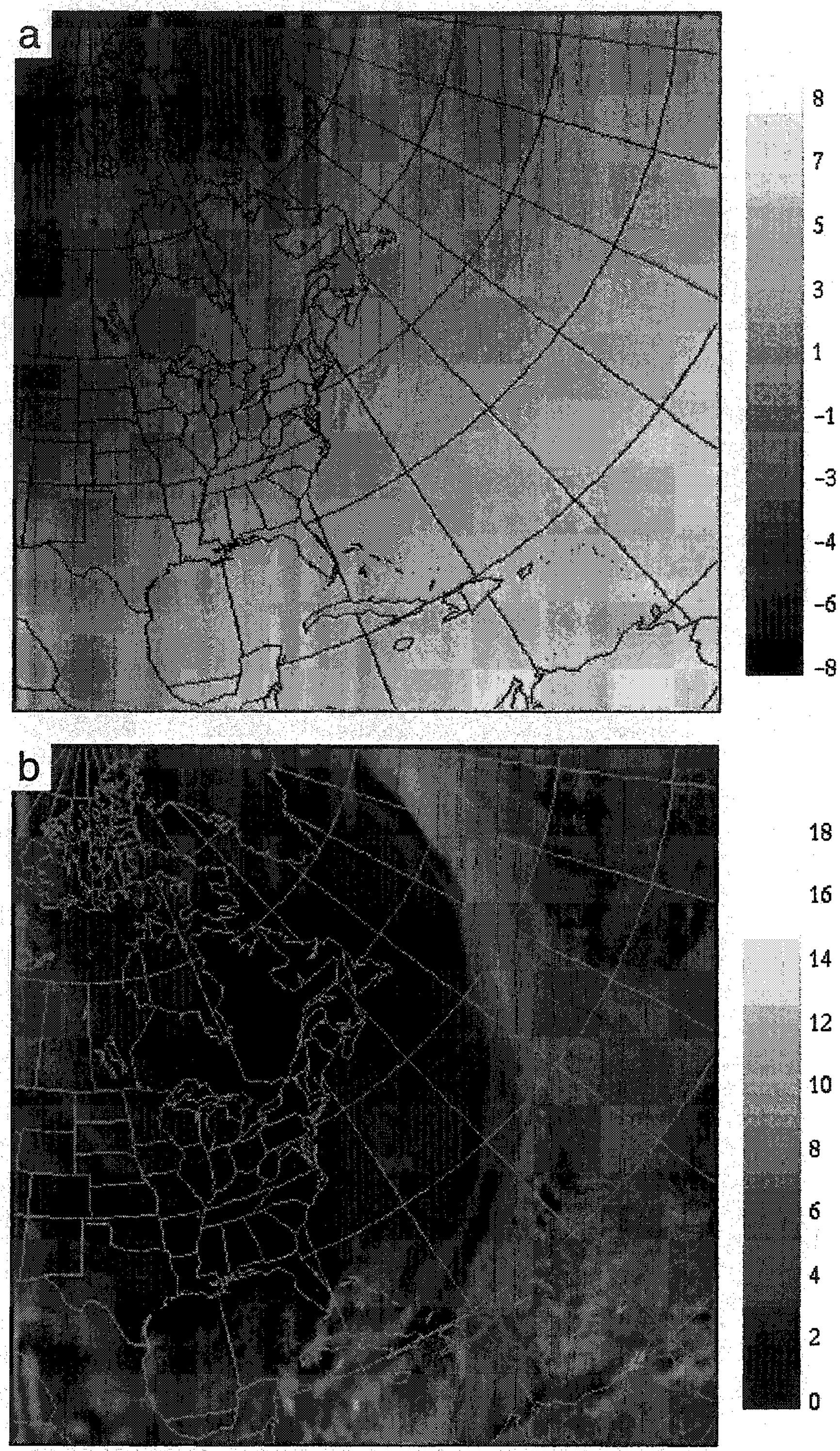

Fig. 3. Trend component (a) that is removed from the humidity field (Fig.1) to get the detrended field (b) used as input for the detrending-DFT method. The line pattern is not generated by a printing problem but by the detrending itself.

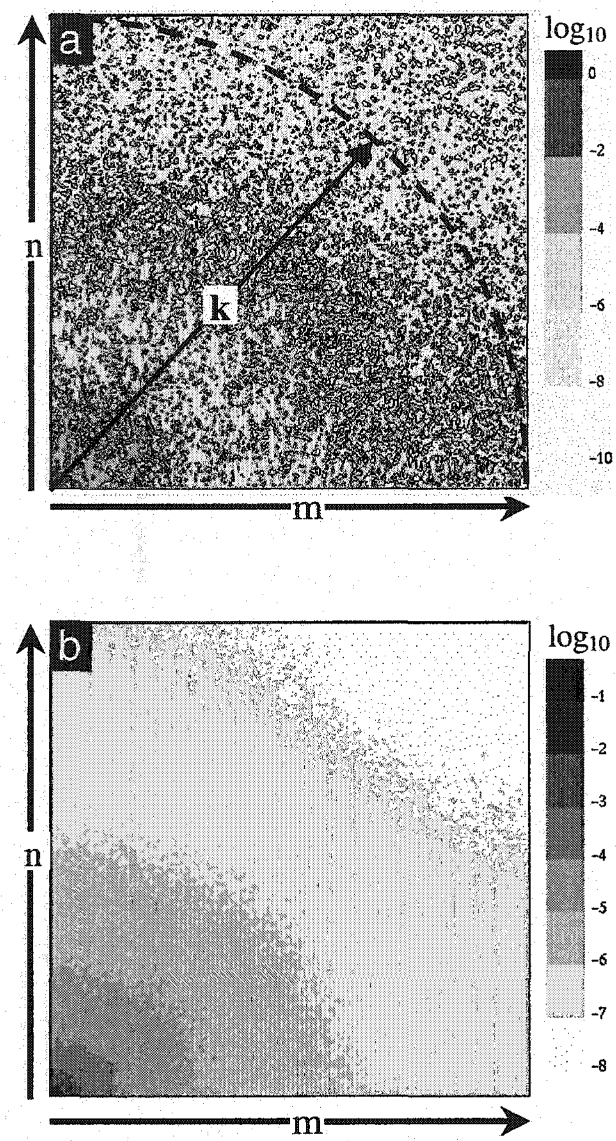

Fig. 4. Examples of a 2D variance array obtained by the application of the 2D-DCT on low-level specific humidity. Plot a) is computed from the field on Fig. 1, and b) is a monthly mean of such 2D arrays. A gray scale is used to display the logarithm of the square of the spectral coefficients. The spectral indices *m* and *n* follow the abscissa and ordinate axes, respectively.

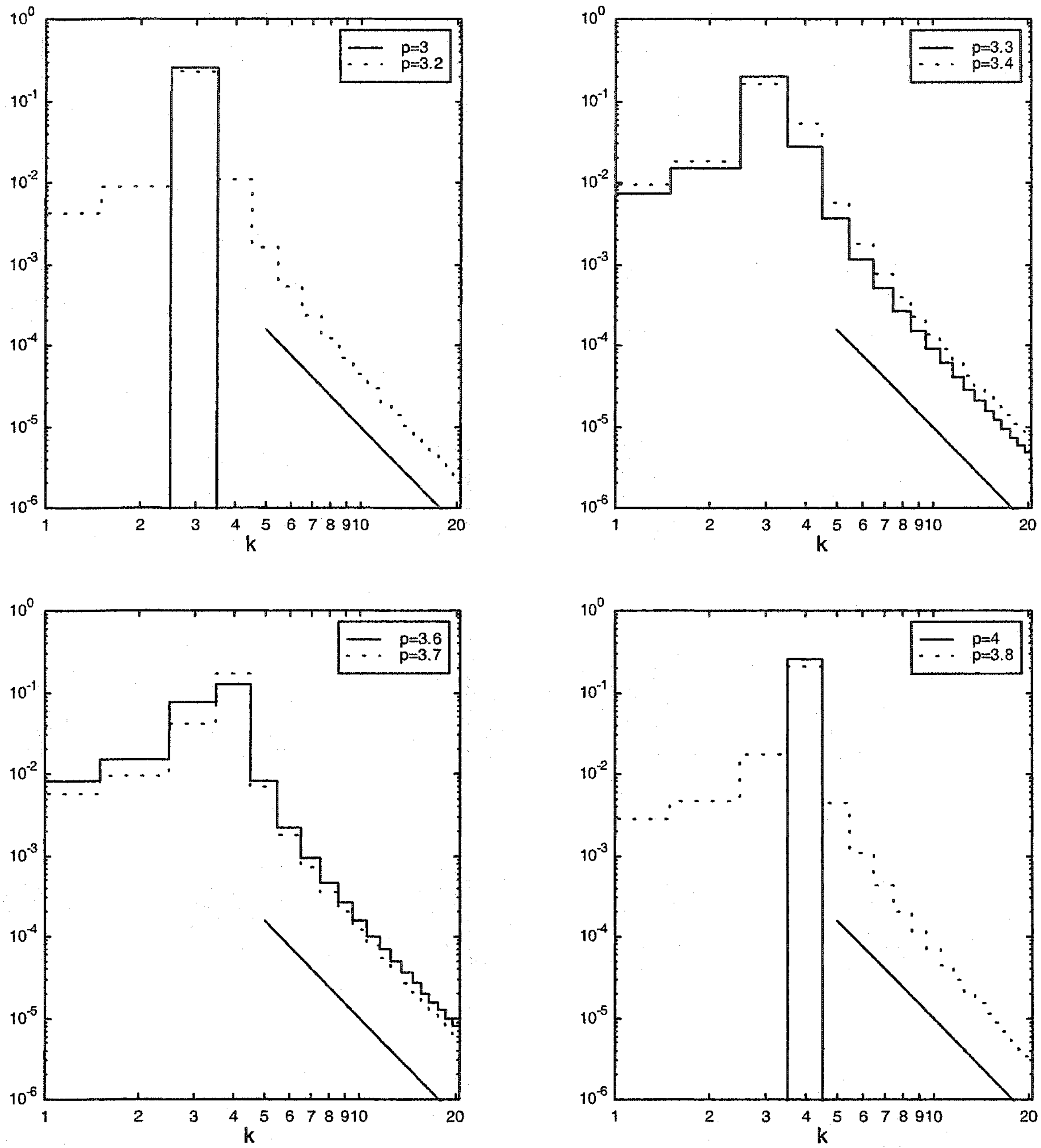

Fig. 5. Power responses of the continuous DCT applied to $h(x) = \cos(px)$ (see Eq. (21)). The responses are shown as a function of wavenumber k and for selected input wavenumber p. A line with a slope of -4 is also drawn for comparison.

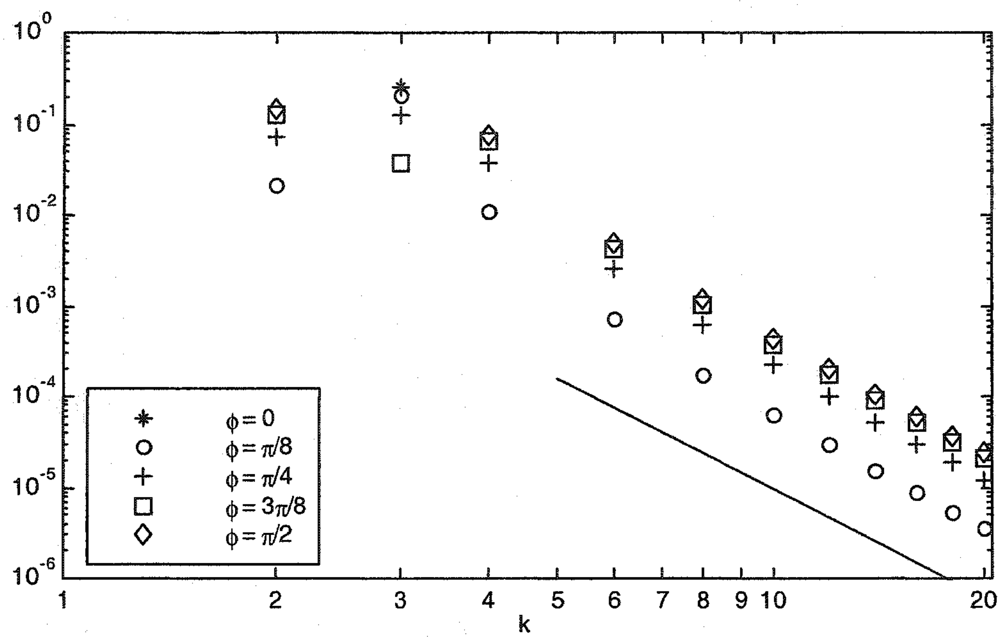

Fig. 6. Example of the influence of phase shifts on power spectra. The input function is $h(x)=\cos(px+\phi)$ with wavenumber $p=3$ and phase shifts of $\phi = 0, \pi/8, \pi/4, 3\pi/8$ and $\pi/2$. A line with a slope of -4 is also drawn for comparison.

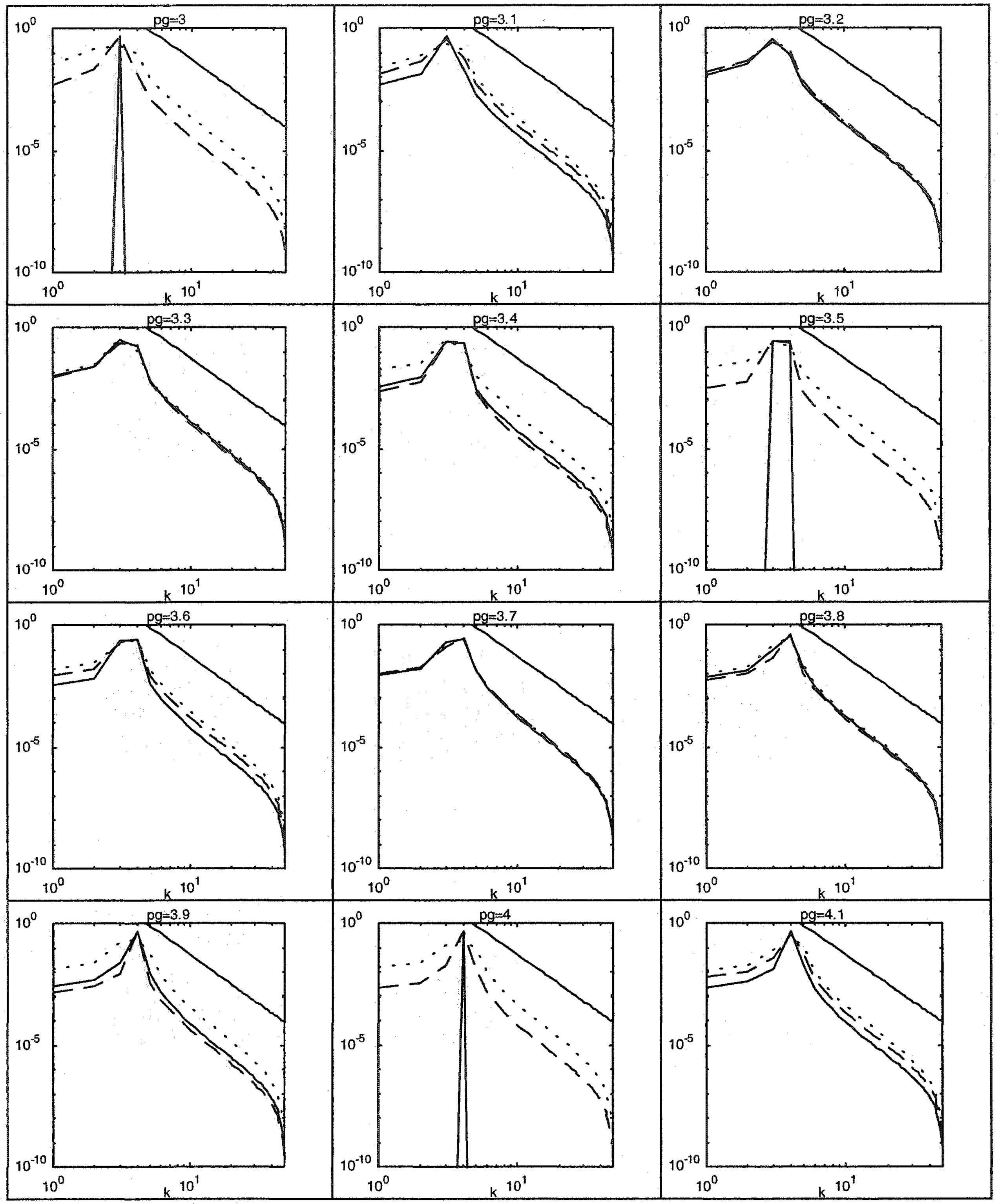

Fig.7. Variance spectra of $h(x)=\cos(px+\phi)$. The wavenumber p varies from 6 (pg=3) on the upper-left panel to 8.2 (pg=4.1) on the lower-right panel. On each panel, three phase shifts ϕ are shown; solid curve: $\phi=0$, dashed curve: $\phi=\pi/8$, dotted curve: $\phi=\pi/2$. The straight line at the upper-right corners is a reference line with a slope of -4.

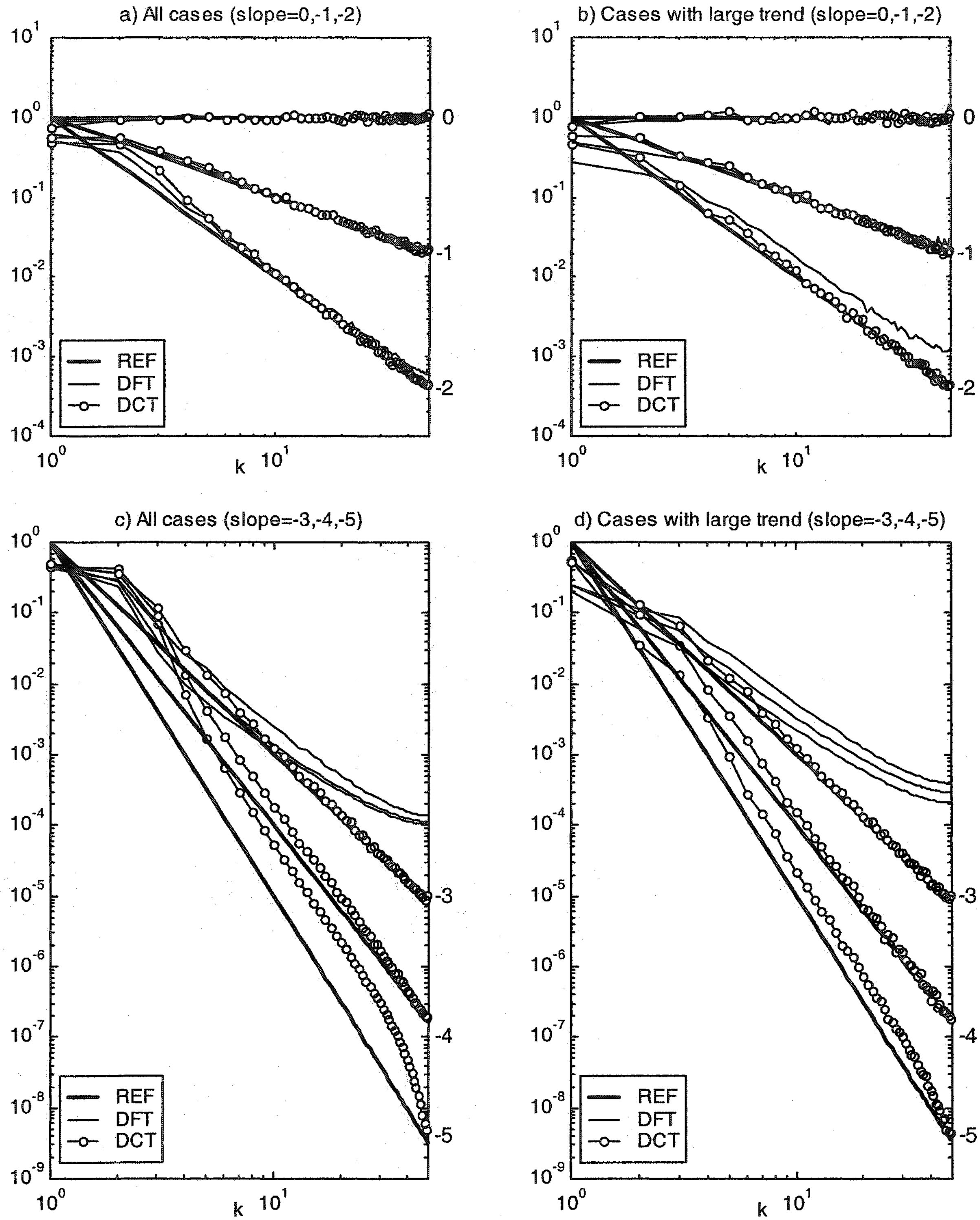

Fig. 8. Variance spectra from the DCT and DFT of 1D fields having prescribed spectral slopes of zero, -1, -2 (a, b) and -3, -4, -5 (c, d). Panels (a) and (c) includes all cases. Panels (b) and (d) include only cases with large trends (aperiodicity larger than 3 standard deviations). The heavy solid lines are reference slopes with values marked at the right on each plot.

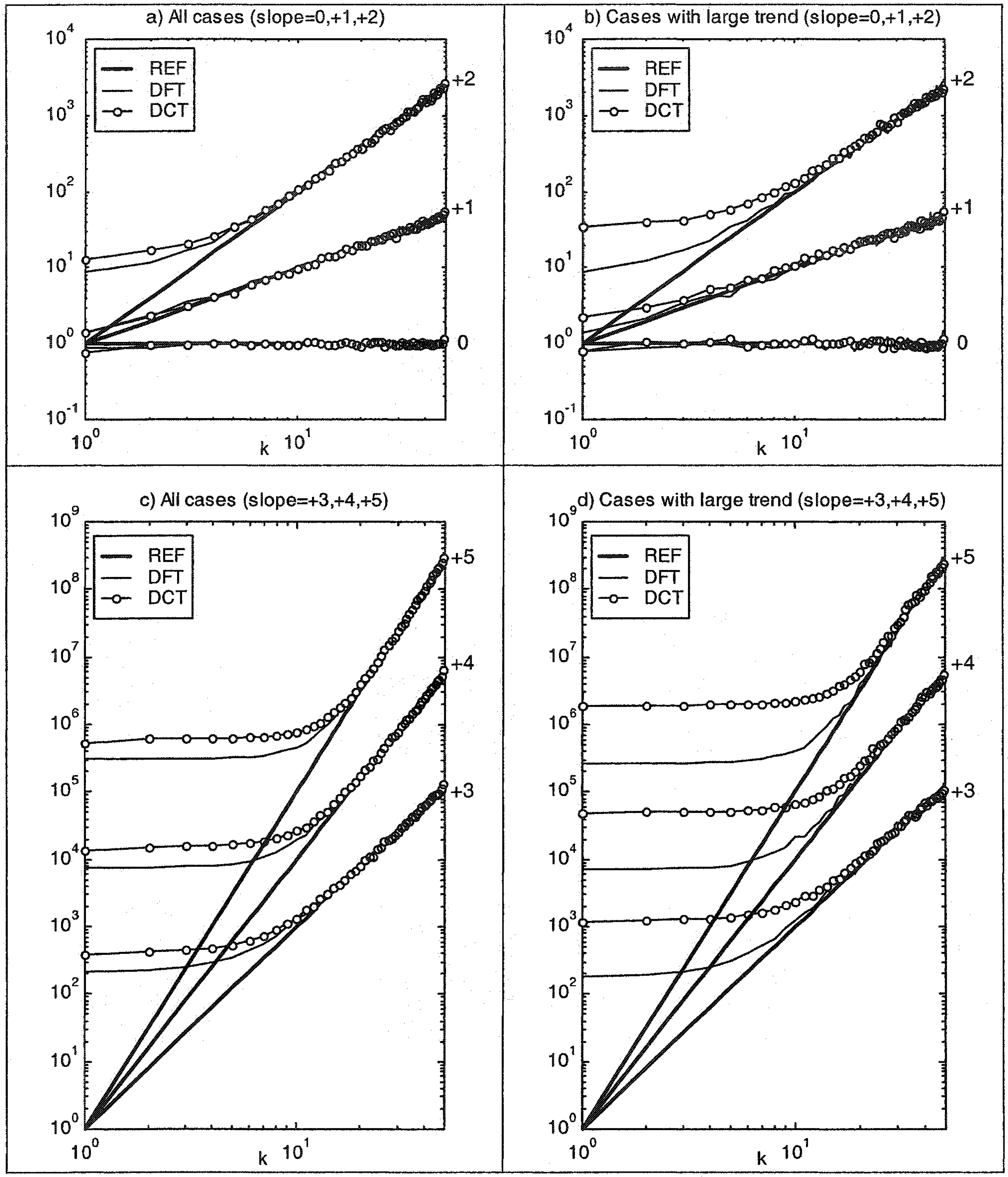

Fig. 9. As for Fig. 8, but for spectra of 1D fields having prescribed spectral slopes of zero, +1, +2 (a, b) and +3, +4, +5 (c, d).

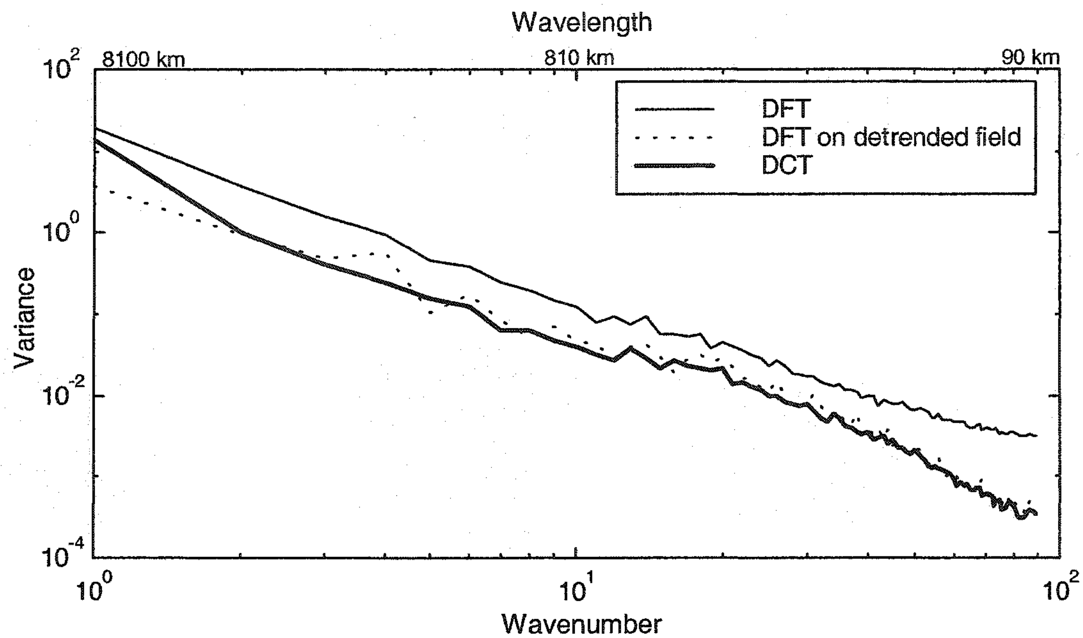

Fig. 10. Variance spectrum of the 925-hpa humidity field (shown in Fig. 1) computed using the DCT (bold solid curve), and the DFT with and without detrending (thin dashed and solid curves, respectively). The units of the variance axis are $(g/kg)^2$.

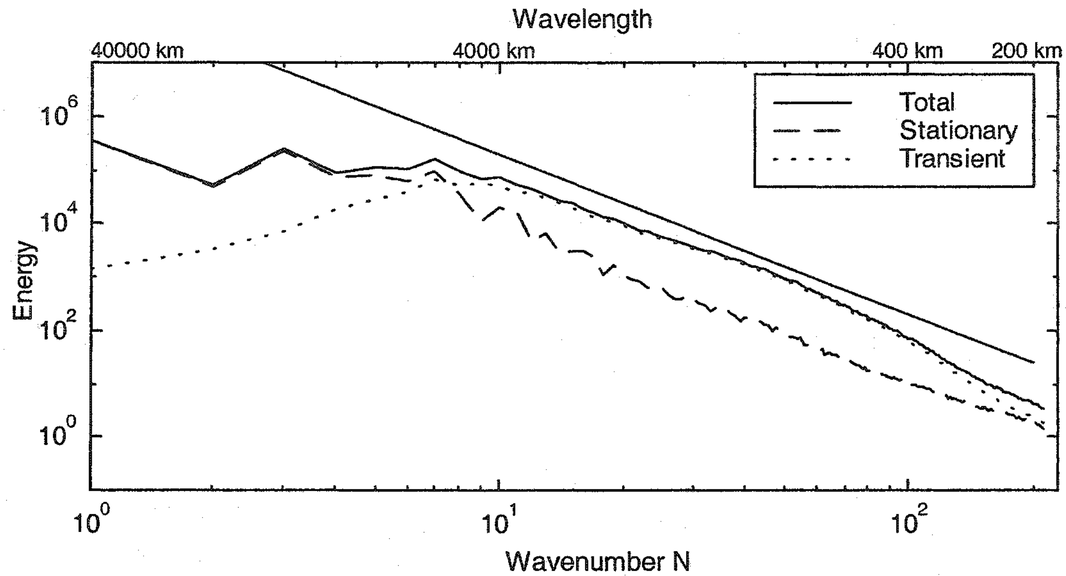

Fig. 11. Vertically integrated kinetic energy spectra for the ECMWF global analysis of February 1993. Shown are the total (solid curve), stationary (long dashed curve) and transient (short dashed curve) components. The straight line is a reference line with a slope of -3. The wavenumbers N are the total wavenumbers of spherical harmonics. The wavelengths corresponding to the wavenumbers N are indicated on upper axis. Units are J/m^2.

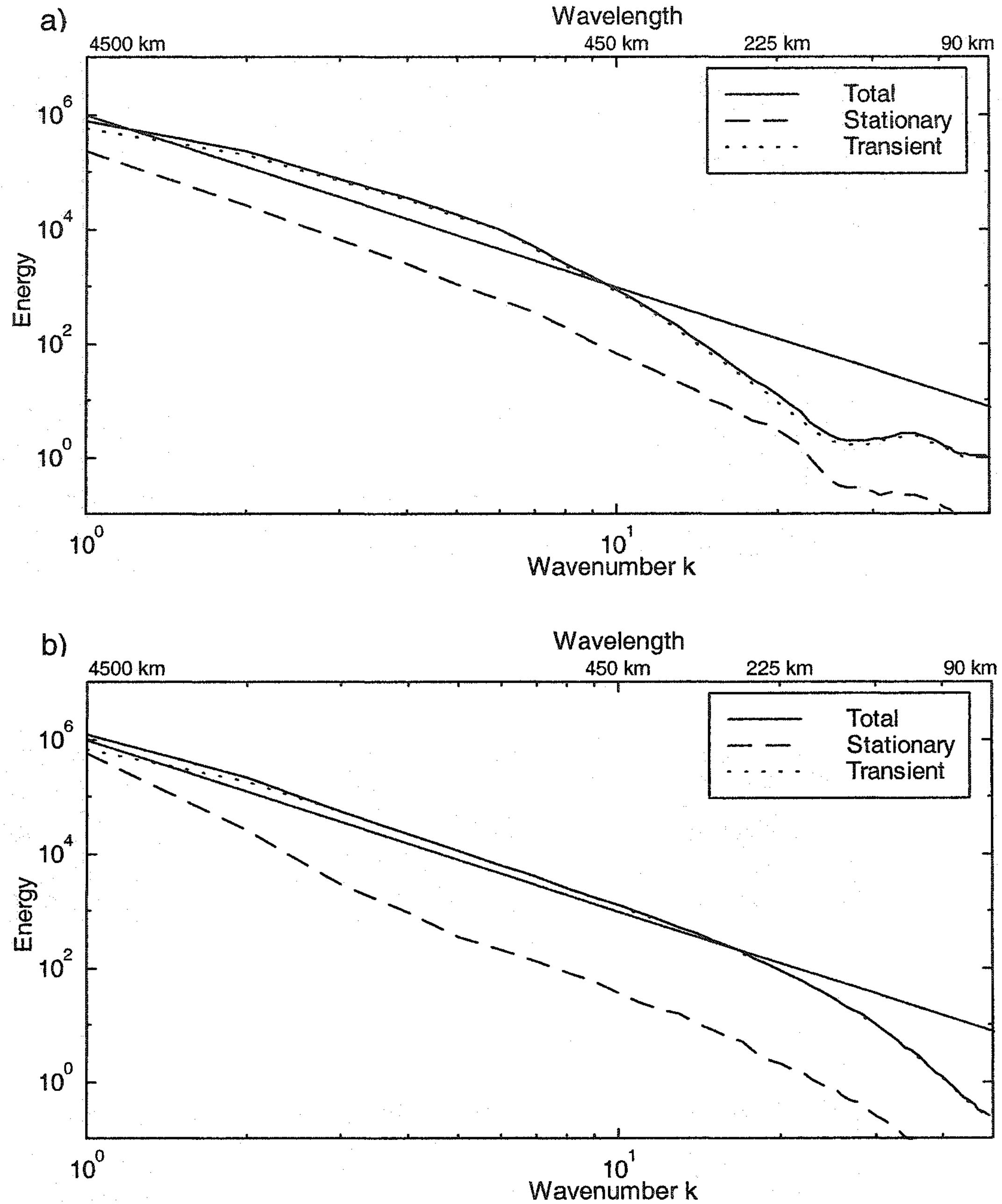

Fig. 12. Vertically integrated kinetic energy spectra computed using the 2D-DCT over a limited area. ECMWF analysis data were used in a) and simulated data produced by the CRCM were used in b). Both are shown on the same plot in c) but for the total component only. The straight line is a reference line with a slope of -3. Units are J/m^2.

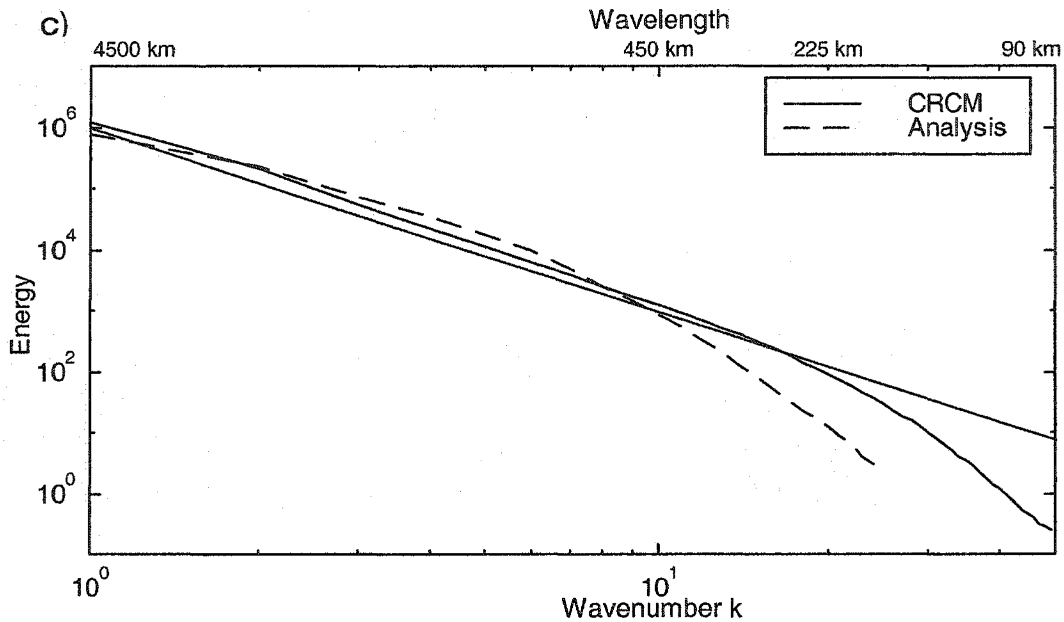

Fig. 12. (continued)

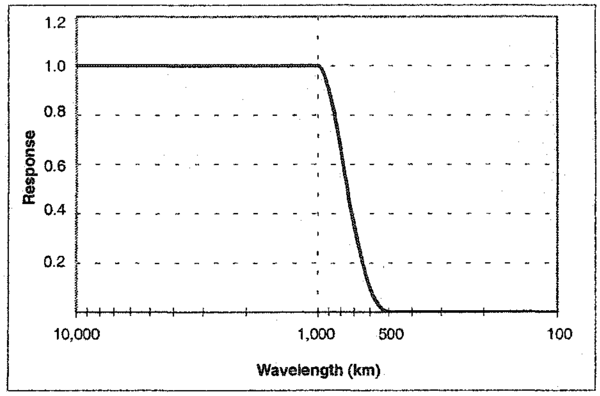

Fig. 13. Response of the spectral filter used for low-pass filtering of the field shown in Fig. 1.

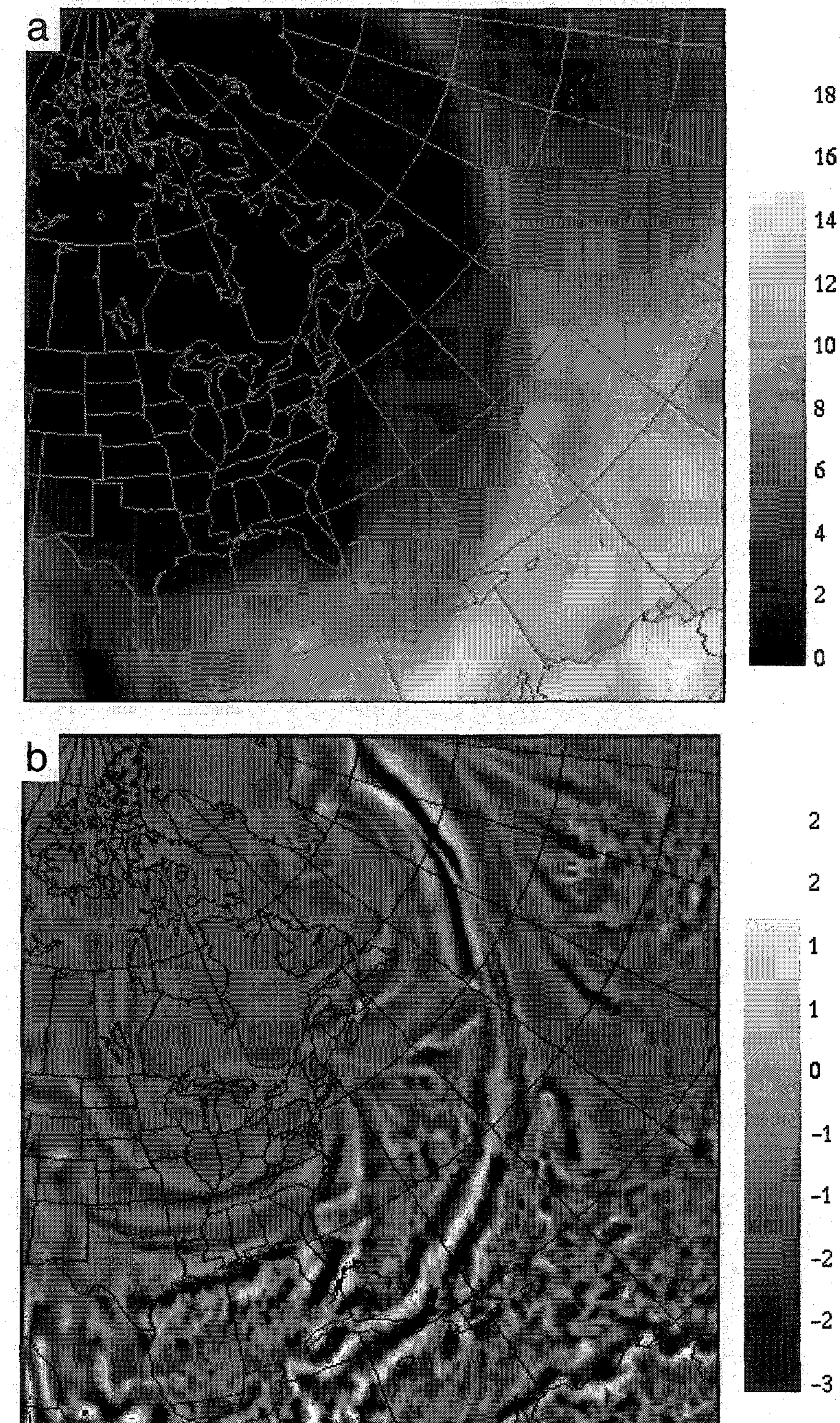

Fig. 14. Band-pass filtering of the humidity field of Fig. 1 for a) Large and synoptic scales, b) mesoscales. Units are g/kg. NB: the gray scales of the two panels are different.

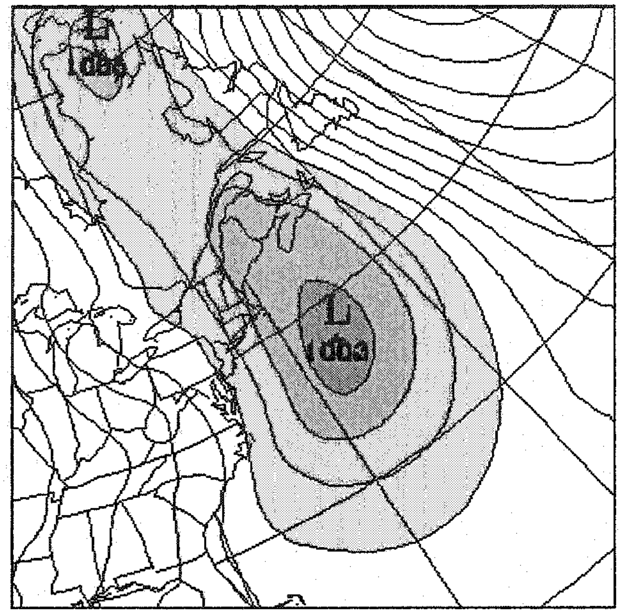

Fig. 15. Monthly mean of mean-sea-level pressure. Contours are at 2 hPa intervals. Areas with values smaller than 1010 hPa are shaded.

a) b)

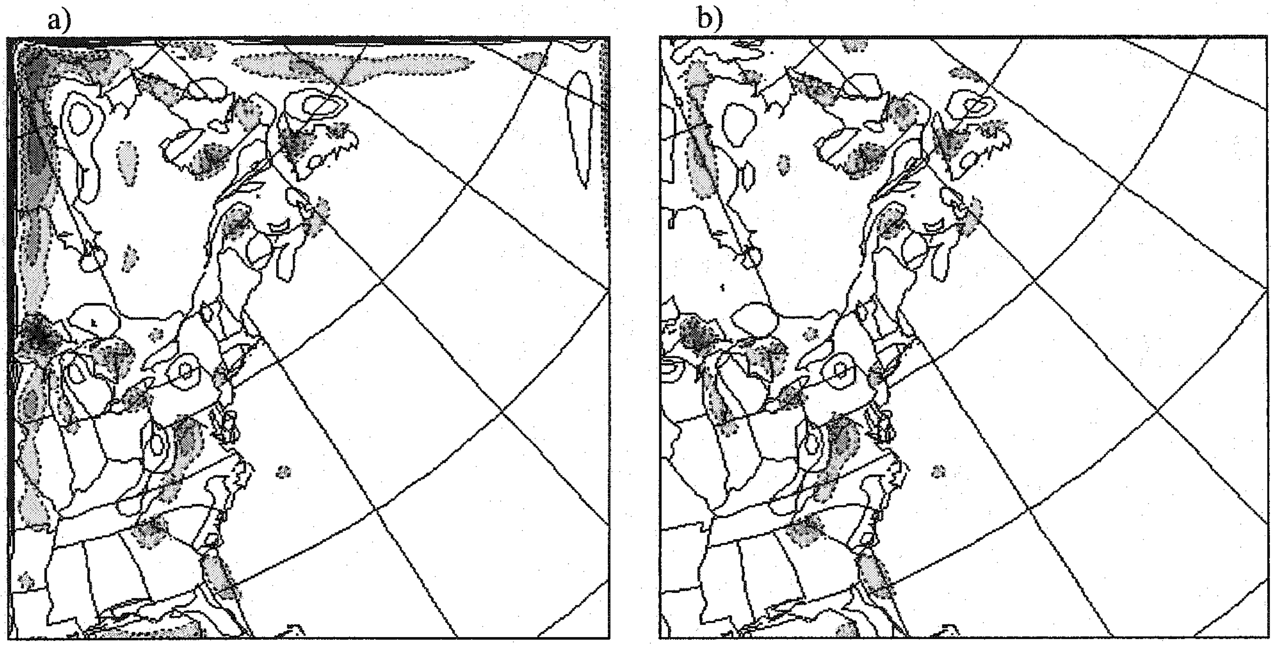

Fig. 16. Small-scale component of the monthly mean of mean-sea-level pressure without (left panel) and with (right panel) boundary smoothing before the 2D-DCT application. Contour intervals are every 0.1 hPa. The zero contour is omitted. Regions with values smaller than -0.1 hPa are shaded.

Figures of the Appendix

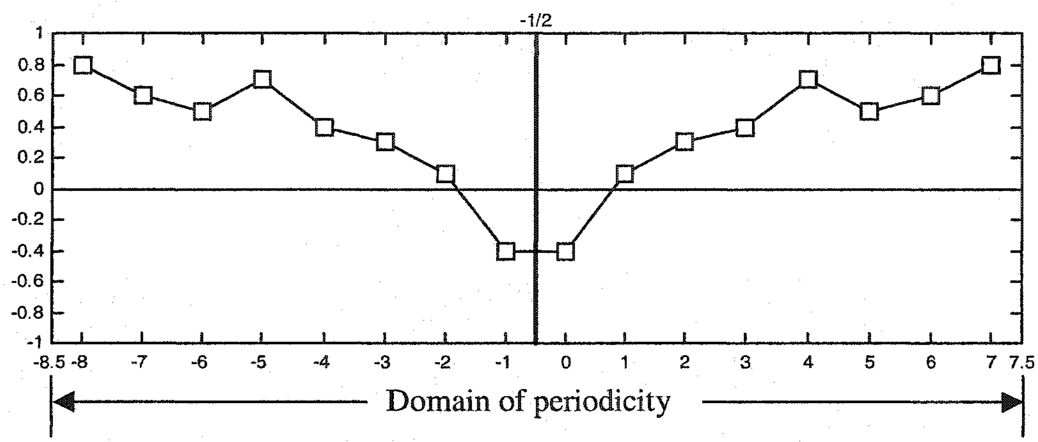

Fig. A1. New function $f_s(j)$ created by symmetrization of the function $f(j)$. In this example the original function $f(j)$ had 8 grid points (on the right-hand side).

Symmetrical (even) Anti-symmetrical (odd)

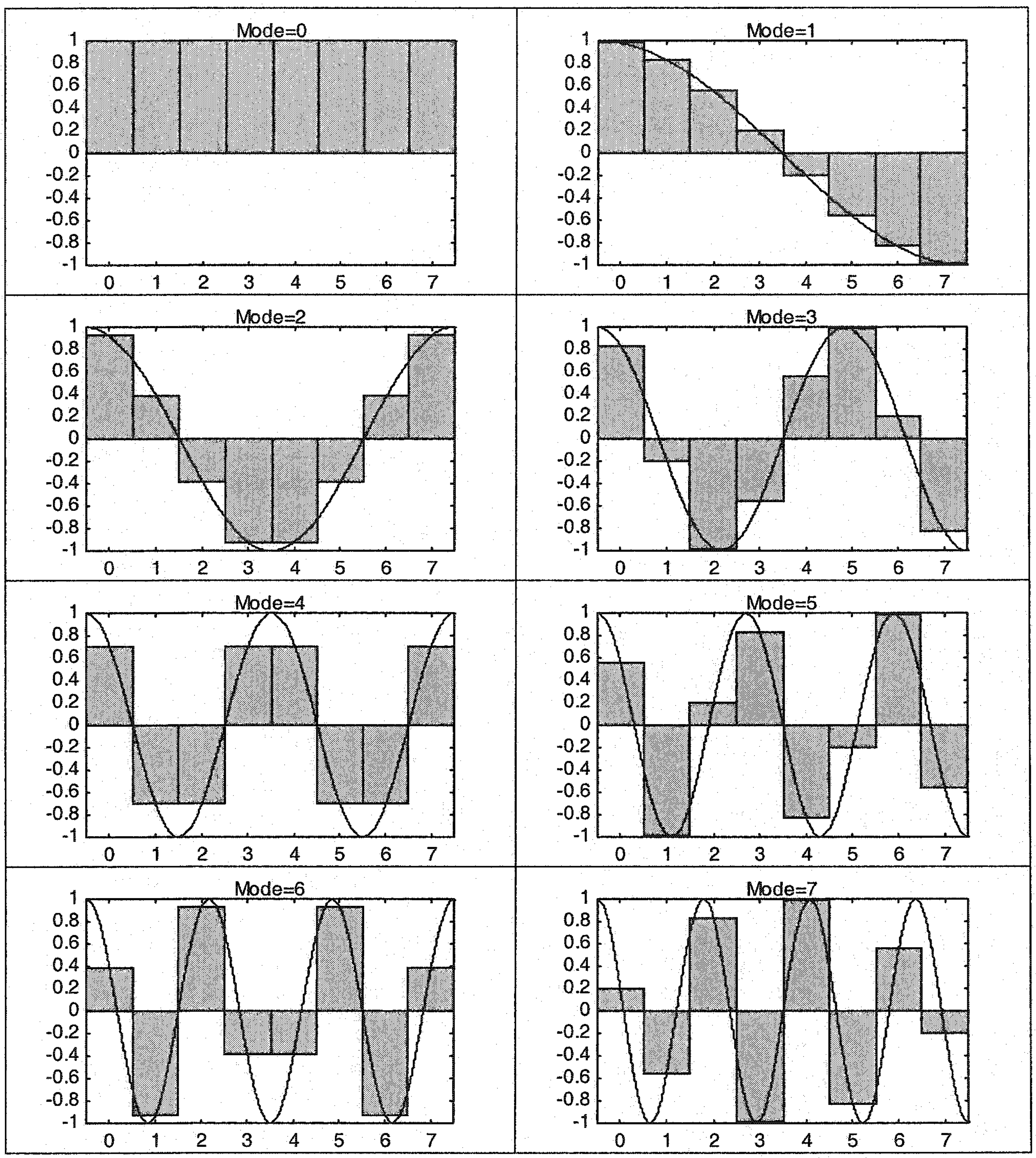

Fig. A2: The possible modes of the cosine basis functions with 8 grid points. The gray bars represent the discrete form of Eq. (A14), i.e. the values at grid points $i=0...N-1$ with $N=8$. For comparison, their continuous forms are shown by the thin curves.

Chapter III

Downscaling Ability of One-way Nested Regional Climate Models: The Big-Brother Experiment

This Chapter contains the full description of the Big-Brother Experiment (BBE). In introduction, a comprehensive review of the main issues concerning the use of one-way nesting RCM is given as well as the rational of using a perfect-prognosis approach (the BBE) for evaluating the downscaling ability of one-way RCMs. Results for a one-winter month are exposed and discussed. The paper contained in this Chapter has been accepted for publication in the journal *Climate Dynamics*. Comments of the reviewers are given at the end.

Downscaling Ability of One-way Nested Regional Climate Models: The Big-Brother Experiment

Bertrand Denis[*+#],
René Laprise[*],
Daniel Caya[*] and
Jean Côté[#]

[*] *Département des sciences de la Terre et de l'Atmosphère, Université du Québec à Montréal, Montréal, Québec, Canada*

[+] *Department of Atmospheric and Oceanic Sciences, McGill University, Montréal, Québec, Canada*

 # Recherche en Prévision Numérique, Meteorological Service of Canada, Dorval, Québec, Canada

Accepted for publication in *Climate Dynamics*

30 July 2001

Corresponding author address:

Bertrand Denis
Recherche en Prévision Numérique
2121 Route Transcanadienne
Dorval, Québec
Canada
H9P 1J3

Email Bertrand.Denis@ec.gc.ca

Abstract

A methodology is developed for testing the downscaling ability of nested regional climate models (RCMs). The proposed methodology, nick-named the Big-Brother Experiment (BBE), is based on a "perfect-prognosis" approach and hence does not suffer from model errors nor from limitations in observed climatologies. The BBE consists in first establishing a reference climate by performing a large-domain high-resolution RCM simulation: this simulation is called the Big Brother. This reference simulation is then degraded by filtering short scales that are unresolved in today's global objective analyses (OA) and/or global climate models (GCMs) when integrated for climate projections. This filtered reference is then used to drive the same nested RCM (called the Little Brother), integrated at the same high-resolution as the Big Brother, but over a smaller domain that is embedded in the big-brother domain. The climate statistics of the Little Brother are then compared with those of the Big Brother over the little-brother domain. Differences can thus be attributed unambiguously to errors associated with the nesting and downscaling technique, and not to model errors nor to observation limitations.

The results of the BBE applied to a one-winter-month simulation over Eastern North America at 45-km grid-spacing resolution show that the one-way nesting strategy has skill in downscaling large-scale information to the regional scales. The time mean and variability of fine-scale features in a number of fields, such as sea level pressure, 975-hPa temperature and precipitation are successfully reproduced, particularly over regions where small-scale surface forcings are strong. Over other regions such as the ocean and away from the surface, the small-scale reproducibility is more difficult to achieve.

1. Introduction

The Intergovernmental Panel on Climate Change (IPCC) acknowledged that global climate models (GCMs) outputs were of too coarse resolution for being directly used in regional climate change impact studies (Houghton et al. 1990). A decade later and despite the increase of computing power, most multi-decadal GCM simulations can still be considered low resolution, i.e. 500-300 km of grid-point spacing (Houghton et al. 2001). Due to their limited resolution, GCMs only support large-scale and synoptic-scale atmospheric features. Because of these resolution limitations, regional climate models (RCMs) have been developed during the last decade for downscaling GCM simulations at the regional and local scales (see McGregor (1997) and Giorgi and Mearns (1999) for a review). The hypothesis behind the use of high-resolution RCMs is that they can provide meaningful small-scale features over a limited region at affordable computational cost compared to high-resolution GCM simulations.

Small-scale features develop in a high-resolution RCM due to three types of sources: (1) The surface forcings, (2) the nonlinearities present in the atmospheric dynamical equations, and (3) hydrodynamic instabilities. The type 1 is thought to be the one that RCMs exploit the most. The intensity of those forcings plays a great role in determining surface regional climates; for instance, the Great Lakes region and the Rocky Mountains are striking examples of land-sea contrast and topographical forcings, respectively. Although it is correct to think that a better representation of small-scale forcings such as topography and other surface heterogeneities are responsible for the increase of details in high-resolution simulations, the nonlinear dynamics (type 2) also play an important role.

Low-level mesoscale frontogenesis in response to upper-level synoptic-scale dynamical forcing are manifestations of these interactions. Internal atmospheric dynamics exhibit a nonlinear downscale cascade (from large to small scales) by stirring and stretching the flow, and this phenomenon would occur even in the absence of surface forcings. Shear and buoyancy in the flow can also, through hydrodynamic instabilities (type 3), produce mesoscale features without the help of surface forcings. The high resolution used by RCMs allows for a better representation of these three types of sources, in addition to the increased accuracy of the numerical scheme employed to solve the governing equations of the climate system. The value-added information that is expected from RCMs should come not only from the finer spatial details but also from better-simulated temporal variabilities. This variability aspect is often a weakness in GCMs (Houghton et al. 2001). For example, it is known that most GCMs produce too frequent light precipitation (drizzle) and too few events of intense precipitation.

The most popular strategy used to get high resolution over a region of interest is the so-called «nesting» strategy, and more specifically the one-way nesting strategy. With this approach, a limited-area mesoscale model is «driven» by low-resolution data previously produced by either a model run over a global domain (GCM) (e.g., Walsh and McGregor 1995; Ji and Vernekar 1997; Laprise et al. 1998; Christensen et al. 1998; Leung and Ghan 1999) or by analyses of observations (e.g., Seth and Giorgi 1998; Takle et al. 1999; Hong and Leetmaa 1999). As the expression "one-way" suggests, no feedback is permitted from the RCM back to the driving data.

There are number of issues concerning the use of nested limited-area models (LAMs) as a climate downscaling technique. Most of them are summarized below and explained in more details by Warner et al. (1997) in the context of short-term weather predictions, and in Giorgi and Mearns (1999) who discussed their outcomes for regional climate modelling:

1. Numerical nesting: mathematical formulation and strategy
2. Spatial resolution difference between the driving data and the nested model
3. Spin-up
4. Update frequency of the lateral boundary conditions (LBCs)
5. Physical parameterizations consistencies
6. Horizontal and vertical interpolations errors
7. Domain size
8. Quality of the driving data
9. Climate drift or systematic errors

It should be noted that while these issues concern directly the one-way nesting, some of them are also shared by other RCM approaches such as global variable-resolution models (e.g., Déqué et al. 1998, Fox-Rabinovitz et al. 2000).

a. Issue 1: Numerical nesting: mathematical formulation and strategy

Briefly, the first issue has to do with the mathematical well-posedness of the boundary-value problem and the nesting formulation employed. Readers are referred to Staniforth (1997) for a theoretical discussion and to Davies and Turner (1977), Baumhefner and Perkey (1982), Robert and Yakimiw (1986) and Yakimiw and Robert (1990) for basic validation experiments of some nesting formulations.

In addition to controlling the evolution of the large scales in the RCM, the nesting strategy should be able to handle properly the synoptic systems that enter and leave the region of interest. Noises that could originate from the nesting zone should not contaminate the whole domain of interest. Seth and Giorgi (1998) showed that the lack of feedback or interactive boundary adjustment of the one-way nesting strategy could be detrimental to the simulated climatology.

b. *Issue 2: Spatial resolution difference between the driver and the nested model*

The second issue is related to the following question: What is the maximum resolution jump between the driving data and the driven model that can be used? Usually the ratio is between 2 and 5 but sometimes as high as 10. When this ratio is thought to be too large, multiple nesting is sometimes used. Such multiple nesting, also called multiple "cascade", was used for example by Christensen et al. (1998). They nested a 19-km horizontal resolution RCM into an RCM at 57-km resolution, which was itself driven by a low-resolution GCM.

c. *Issue 3: Spin-up*

The third issue concerns the spin-up period of the RCM, i.e. the time that the model takes to achieve its climate equilibrium. Since the climate system has many components with different response time scales, different spin-up periods can be defined. The longest spin-up period appears to be related to the surface hydrology due to the deep soil temperature and moisture content. The spin-up period in that case is of the order of months to years. At the other end of the spectrum, fine-scale atmospheric features responding to fast dynamical and thermo-dynamical forcings have much shorter response time scales. In this study we will have a look to that fast spin-up period: What is the spin-up period needed to generate fine-scale atmospheric features?

d. *Issue 4: Update frequency of the LBCs*

This issue has to do with the temporal resolution of the dataset used to drive the nested RCM. For example, the driving data may have been archived at 00:00 GMT and 12:00 GMT only. Because LAMs have a much shorter time-step than a GCM, of the order of a few minutes for a grid-point spacing of 50 km, linear interpolations in time are used between the archival times. Nevertheless, the effective nesting period resolution in that case remains 12 hours, which could be too coarse to capture fast moving synoptic systems that should enter into the LAM domain. As a rule of thumb, the update period should be smaller than one quarter of the ratio of the length scale to the phase speed of the meteorological phenomena that we want to get correctly in the LAM domain. For instance, a typical synoptic system having a horizontal size of 1000 km and a phase speed of 50 km/h would require an updating frequency of at least 5 hours.

e. *Issue 5: Physical parameterizations consistencies*

This issue has to do with this question: Should the physical parameterization be the same between the driving and the driven model? The use of different physical parameterizations in the driver model and the nested one could potentially generates undesirable errors close to the boundaries. For instance, the application of two different parameterizations at neighbouring grid points (one in the limited area and the other one outside) could lead to unphysical forcing gradients. To counterbalance this, the dynamics might respond by generating spurious noise. This problem can be reduced if the same parameterization is used, but even then, the parameterized forcing may differ due to its possible sensitivity to the different resolutions. However, because of the difference of scales, one might want to use parameterizations more appropriate to each model resolution.

f. Issue 6: Horizontal and vertical interpolation errors

This issue concerns errors, inconsistencies and imbalances that can be generated by interpolations necessary to do the nesting. In the horizontal, the grid-point spacing and often the map projections on which the driving data are generated are different from the one used by the RCM. The same happens in the vertical, vertical interpolations are needed to go from one system of coordinates to the other one. For instance, Caya and Laprise (1999) reported that spurious supersaturation could be generated by the suite of interpolations to link their GCM and RCM. Differences between the topographic fields due to the different resolutions imply that extrapolations below the surface of the driving model have to be performed. The extrapolated data are then fictitious and the total fluxes through the lateral boundary are thus difficult to conserve.

g. Issue 7: Domain size

This issue concerns the different simulated climate solutions that can result from just changing the domain size. This issue is probably the one that has received the most attention by RCM users. Jones et al. (1995) studied the influence of lateral boundary forcing on one-way nested RCM simulations using domains of different sizes. Their goal was to find the optimum domain size for which the RCM`s large-scale circulation was constrained to follow the driving GCM, but also for which the finer scales had enough space to develop. From four different domain sizes, they showed that the largest was too large and resulted in a significant deviation from the GCM solution. On the other hand, lateral boundaries of the smallest domain exerted too strong control on the solution, so that the temporal variability (storminess of the flow) did not increase compared to the GCM as it did for the larger domains. In a study of climate change using an RCM, Jones et al. (1997) found that in the summer season the large-scale RCM solution diverged from the GCM. They suggested that a smaller domain size could avoid this, but at the price of weaker mesoscale features generated by the RCM. In another study investigating the effect of the domain size on summer precipitation, Seth and Giorgi (1998) reached similar conclusions using analysed observations as driving data. They found that with the smaller domain size, the precipitation field was closer to that observed but the sensitivity to the internal forcing was better with the larger domain. Jacob and Podzun (1997) also studied the sensitivity of precipitation to the domain size. They showed that two different domain sizes could yield totally different precipitation field solutions. In comparison, difference in initial conditions led to smaller discrepancies. This showed how the nesting issue for RCMs is more a boundary value problem than an initial value problem as it is the case for short-range forecasting. If one sees a one-way nested RCM has a downscaling tool, the domain has to be of the appropriate size to leave the room needed for the tool to freely produce the expected «value-added» small-scale information. The sensitivity of the solution to the domain size seen with RCMs using lateral boundary nesting techniques is due to the ineffectiveness of the nesting for controlling the large scales over the whole domain. To circumvent this, an alternative technique called "spectral nudging" or "large-scale driving" can be used (e.g., Waldron et al. 1996, von Storch et al. 2000 and Biner et al. 2000). With this technique, the large-scale portion of the RCM solution over its whole domain is relaxed to the driver solution.

h. Issue 8: Quality of the driving data

This issue has basic implications in the concept of nested RCMs because even with a perfect model and a prefect nesting scheme, the quality of the driving data used is very important. In the case of a GCM driving an RCM, if the simulated GCM large-scale circulation is wrong, good results cannot be expected from the RCM. In other words, «garbage in» => «garbage out. Risbey and Stone (1996) underlined this issue and argued that, even with a high-resolution GCM (NCAR CCM2 at T106), the jet-stream position over the North-American West Coast is too incorrectly positioned to expect skilful RCM simulations over parts of California.

To estimate the contributions of the driving GCM circulation and the internal RCM physics to the total RCM errors, Noguer et al. (1998) compared an RCM simulation driven by a stand-alone GCM with another RCM simulation driven by a GCM that was strongly relaxed to operational analyses. This later GCM had very little systematic error compared to the freer stand-alone GCM. They found that 80-90% of the sea level pressure RCM error variance originated from the driving data itself. More surface-forced fields such as surface air temperature and precipitation were less influenced by systematic errors in the imposed circulation than by the internal physics, specially during summer conditions.

i. Issue 9: Climate drift or systematic errors

This last issue concerns a fundamental question: Can RCMs be run for a long time without generating systematic errors or climate drifts? Even though the lateral nesting exerts a strong control on the large scales inside the domain, an RCM can develop biases due to weaknesses in its formulation: inadequate resolution, non-conservative numerics, incomplete physical parameterizations and intrinsic weaknesses of the nesting strategy. In fact, all of the previously eight issues can contribute to systematic errors in an RCM simulation.

As we can see, the use of the one-way nesting strategy involves a number of important issues. These issues have brought up skepticism in the climate modelling community concerning the reliability of regional climate simulations using the nesting strategy. The working group on numerical experimentation (WGNE) of the World Climate Research Programme (WCRP) has also expressed scepticism and, as it is its role, has asked the regional climate modelling community to make *clean* experiments to show the proof-of-concept of the regional climate modelling using the one-way nesting strategy (CAS/JSC

WGNE 1999, 2000).This study is about one such experiment. More precisely, the main objective of this study is to test the hypothesis under which RCM are employed, that is:

> "One-way nested RCMs can accurately simulate fine-scale climate features when driven by large-scale information only."

The experimental framework that we have set-up to validate this hypothesis has been constructed to focus on issues number 1,2,3 and 9, namely the numerical nesting formulation, the effect of the resolution jump, the spin-up and systematic errors.

The rest of the paper is organised as follow: In section 2, the experimental design for validating fine-scale features is given. Section 3 contains the results, which are followed by a discussion (section 4), and conclusions (section 5).

2. Experimental design

Since the goal of this study is the assessment of downscaling ability of the one-way nesting strategy for regional climate modelling, the experimental design must permit validation of small-scale features. Validation of the RCM's small scales using low-resolution GCM output as driving data and climate reference is impossible because the small scales generated by the RCM are absent from the GCM. The replacement of the GCM by objective analyses produced by an assimilation system, such as the NCEP analyses, does not help since those analyses are also of a too coarse resolution and are not free of observation analysis and data-assimilation model errors. Data from other sources can be used, but they are restricted to regions with high-density observational networks near or at the surface, and for a limited number of variables such as precipitation and surface air temperature. Because of that, validation of the small scales over the oceans is almost impossible for instance. Finally, the use of perfect and high-resolution analyses would not resolve the problem of discriminating between errors due exclusively to the nesting strategy and errors due to the rest of the model formulation.

a. The big-brother experiment

In order to circumvent these validation issues we have adopted a perfect-prognosis approach, nick-named the Big-Brother Experiment (BBE). In this approach, the first step consists in running a global high-resolution model to produce a high-resolution reference dataset. Then, the small scales existing in that reference dataset are filtered to generate a low-resolution dataset needed to drive the nested RCM. Therefore only the large and medium scales would be used to feed the "little-brother" RCM such as to mimic the nesting of an RCM by a GCM. The reference dataset (before filtering) however would contain small scales against which the RCM small scales could be validated.

Fig. 1 shows a flowchart of this approach. The objective is to see how the little-brother simulation is capable to reproduce the big-brother small scales when it is guided with only the large and medium scales of its Big Brother. The clear advantage of this BBE is that since the model resolutions, physics, dynamics and numerics are the same and therefore the model errors are also the same, the differences can be indubitably attributed to the nesting strategy.

An obvious disadvantage of this big-brother experiment is the high computational cost of running the global high-resolution simulation. For this reason, we used a modified version of this experiment that does not employ a global model but the same RCM for both the Big and Little Brother. The Big Brother was run over a much larger domain than the Little Brother but still smaller compared to a global domain. Fig. 2 shows the flowchart of what we have baptised «the poor-man big-brother experiment».

The details of our poor-man BBE set-up, including a brief model description, the nesting scheme, the domain locations and the spatial filtering used for the preparation of the LBCs are given in the next section.

b. Details of the experimental set-up

The RCM we employed to do our poor-man big-brother experiment is the Canadian Regional Climate Model (CRCM) (Caya and Laprise 1999). It is a limited-area grid-point non-hydrostatic model that uses a three-time-level semi-Lagrangian semi-implicit time marching scheme. The timestep used in our experiments was 15 minutes. The one-way nesting technique has been developed by Robert and Yakimiw (1986) and Yakimiw and Robert (1990) and is inspired from Davies (1976). A nine-point wide region along the lateral boundaries defines the so-called nesting zone in which the horizontal velocity components of the CRCM are relaxed to the driver model's ones. A complete description of the dynamical formulation of the CRCM including the nesting implementation can be found in Bergeron et al. (1994) and Laprise et al. (1997). The physical parameterizations is similar to what can be found in Caya and Laprise (1999) except for the moist convection scheme, which now follows the Kain and Fritsch (1990) formulation. The time evolution of the sea-surface temperature (SST) was imposed by linearly interpolating monthly mean climatological data. Because of that, there were no fine-scale structures in the SST field.

Fig. 2 shows that the realisation of the poor-man version of the big-brother experiment involved two RCM integrations. The Big Brother had a large domain of 196x196 grid-points. Its output data served to drive the second integration (Little Brother) on a smaller domain (100x100) placed at the centre of the BB domain. The grid-point spacing for *all* simulations was 45 km on a polar-stereographic projection true at 60-deg. North. Fig. 3 shows the layout of the domains. Also shown are the topographic field, and the land/open-water/sea-ice mask.

In the vertical, 18 model levels (defined by a geometric scaled-height terrain-following vertical coordinate) were used, and were the same in both the Little and Big Brother. Having the same vertical model levels in both the Little and the Big Brother simulation reduced the importance of the issue 6 concerning the interpolation. Nevertheless, big-brother RCM data were interpolated from its model levels to pressure levels followed by another interpolation to the model levels. This was done to mimic the GCM-RCM mode of operation used by the CRCM system.

All the integrations have been produced for one month, February 1993. This winter month has been chosen because of the strong storm activity along the North-American Eastern Seaboard. The Big Brother was driven by the NCEP analyses archived every 12 hours. The big-brother output were saved every 3 hours for the nesting of the Little Brother. This gave an effective time-resolution of nesting that is higher than what is usually seen with RCM simulations at this spatial resolution. The goal was to reduce the impact of problems discussed in issue 4 concerning the update frequency of driving data.

Since the Little Brother has to be guided by the Big Brother with only the medium and large-scale meteorological information, the horizontal small-scale content of the big-brother output was filtered out. The filtered data served for the lateral nesting as well as for the initial conditions of the Little Brother. The filter used is a Fourier type of filter suitable for non-periodic data and is described in Denis et al. (2001). In order to mimic the resolution of operational GCMs, all disturbances having wavelengths smaller than 500 km have been removed while wavelengths greater than 1000 km were left unaffected by the filter. Fig. 4 shows the filter response curve. The resolution jump between the filtered driving data and the shortest resolvable wavelength of the little-brother is therefore at least 6, i.e. ~ 500 km / (2x45 km). Finally, it should be noted that the runs were produced in a "climate" mode, i.e. the initial conditions were set only once at the beginning of the one-month integration; no further initialisation was made at later times during the month.

This configuration of our poor-man BBE should permit a clean validation of the RCM small scales to address the issues 1 to 3 and 9; i.e. the numerical nesting formulation, the effect of the resolution jump, the spin-up and systematic errors.

3. Results

We will analyse the simulation from two points of view. The first will focus on the first few days of the experiment to scrutinize how well the Little Brother regenerates the small scales from the low-resolution initial and lateral boundary conditions. This will help us to assess first order shortcomings related to the first three issues, i.e. the nesting formulation, the resolution jump and the spin-up. Secondly, we will present one-month "climate" statistics which should be more revealing of any systematic errors (issue 9) produced by the nesting, in addition of giving us a better sample of meteorological systems occurring during the month.

a. Small-scale generation and spin-up.

In this subsection, we analyse the atmospheric spin-up by subjectively comparing the evolution of the moisture field at 700 hPa and the relative vorticity/geopotential height at 1000 hPa. We will close this subsection by a quantitative analysis of the spin-up as a function of scales for the kinetic energy at low levels.

i. Specific humidity at 700 hPa

Fig. 5 shows the atmospheric spin-up time series for the 700-hPa specific humidity field. The reference simulation, the Big Brother, is shown on the left column. The Little Brother is on the right column within the inner squares; outside these squares the filtered Big Brother is shown to allow a visual evaluation of the lack of fine scales at the lateral boundaries. The squares are also drawn on the big-brother column to ease the comparison. The Big Brother has been started five days prior to the little-brother initial time (T= 0 hour) to allow for the development of its own flow from the NCEP analyses. As it can be seen at the initial time, the little-brother initial conditions contain only scales larger than 500 km. The comma-like feature associated with a low-pressure system over the southeast of the Great Lakes and the moist comma tail over the southern part of the little-brother domain has been smoothed. Even more noticable is the removal of sharpness of the moist line oriented southwest-northeast over the right side of the domain; mesoscale disturbances along this line have also been removed by the filter.

After 24 hours, some fine-scale features have started to reappear. The southwest-northeast sharpness of the comma tail has been regenerated and its position is good. The moist line has also been partly re-tightened but mesoscale disturbances on it have not yet redeveloped their full amplitudes. At 48 hours, the comma has been fully redeveloped except for the part of the tail that is in the relaxation zone. That zone also affects the north-south moist line. At 72 hours, the two features we have been following are now compressing against each other over the right side of the domain. Another system that has beginning entering on the left side of the domain at 48 hours is now centred over southern Québec. At this point, this system has still somewhat less well-defined edges in the little-brother case but its position is good. At 96 hours, the patterns are rather similar even for some small-scale features. The inspection of the rest of the month showed that the large-scale features were generally very well reproduced in terms of shapes and positions. The amplitude of small-scale features were also regenerated but their exact positions and shapes were less well forecast in a deterministic sense. Small-scale features over the ocean having convective sources had more stochastic behaviour while those such as sharp fronts that were dynamically linked to the large scales were better deterministically reproduced.

ii. Relative vorticity and geopotentiel height at 1000 hPa

Fig. 6 shows the first 4 days of the 1000-hPa relative vorticity and geopotentiel height fields. The time sequence corresponds to Fig. 5 but in this case only the little-brother domain is shown to get a closer view. We chose to show the relative vorticity field because it highlights the small scales of the flow.

At initial time, the little-brother fields contain no wavelengths smaller than 500 km. After 24 hours, most of these small-scale features have been partly restored. In fact, most of them were already regenerated after 12 hours (not shown). At 48 hours, a low-pressure system has started to enter by the west side of the domain. Because it is still in the relaxation zone, the system is weaker than in the big-brother case but after 60 hours (not shown), the system has left the relaxation zone and has re-intensified. It is interesting to note that semi-stationary small-scale features are present over the Great Lakes and the Appalachian Mountains. The trough over the Great Lakes can be observed in the Little Brother as well in the Big Brother after 24 hours.

The rest of the month was also dominated by weather systems coming from the left-side boundary and intensifying over the ocean, then turning northeastward to leave the domain through the northern boundary. This general behaviour was the result of the predominance of an upper through oriented from the upper-left corner to the lower-right corner of the domain.

iii. Spectral analysis of the spin-up time at low level

We have conducted a Fourier analysis of the kinetic energy (KE) to objectively evaluate the dynamical spin-up time as a function of scales. The winds in the 850-1000 hPa layer have been used to compute the ratio of KE of the Little and Big Brother during the first 24 hours. The lateral relaxation zone is not considered in the computation. The ratio of KE is defined as:

$$R_{KE}(k) = \frac{KE_L(k)}{KE_B(k)} \quad , \tag{1}$$

where

$$KE(k) = \frac{1}{2}\int_{850\text{ hPa}}^{1000\text{ hPa}} (u_k^2 + v_k^2)\frac{dp}{g} \quad , \tag{2}$$

and k the bi-dimensional horizontal wavenumber. $KE_L(k)$ and $KE_B(k)$ are respectively the kinetic energy of the Little and Big Brother. For a more straightforward interpretation we present the results as a function of wavelength in km.

Fig. 7 shows $R_{KE}(k)$ for selected times during the first 24 hours. We can observe that the Little Brother has recovered more than 80% of the Big Brother KE and this at all scales after 24 hours. Most of the adjustment appears to occur between 6 and 12 hours. Using 80% as a threshold for defining a spin-up level, Fig. 8 shows the time it took to reach this threshold as a function of scales, i.e. the spin-up time for the different scales. We can see that the spin-up time generally increases with the length scales between 100 and 500 km, except of course for the largest scales since these were already present in the initial conditions.

Up to this point, we have only looked at the first few days of the experiment. During this period, we saw that a synoptic-scale meteorological system can be successfully brought inside the domain through the nesting zone. From there, it was taken in charge by the mesoscale model that had enough resolution to generate smaller scale features such as sharp fronts. We saw that the Little Brother had regenerated most of the KE within 24 hours. This regeneration of variance at all scales does not mean that the Little Brother is successful in predicting all scales from a deterministic point of view. The small-scale patterns must also correlate well with the big-brother ones for the small scales to be qualified well predicted. This is particularly difficult for small-scale features since for the same amount of positional error, the spatial de-correlation is higher than for large-scale features. Laprise et al. (2000) looked at the predictably as a function of scales in a nested LAM and noted that there is little deterministic predictability for scales not present in the initial and boundary conditions.

In a context of regional climate modelling, the interest is not so much in the deterministic forecast ability of the model but in the climate simulation ability. More precisely, we want to know the extent to which the little-brother small-scale activity yields to the same climate statistics of its Big Brother. That is the topic of the next subsection.

b. Climate downscaling ability

In this section we analyse the "climate" statistics based on one simulated month. For most applications, one month is surely too short to get significant statistics. This period of time appears long enough however to reach some preliminary basic conclusions. The Little Brother was run for 33 days and the first 5 days were discarded to be sure to reject any short time-scale spin-up phenomena. Therefore our month is in fact the last 28 days of the simulations. The sampling time interval is 3 hours.

The computation of the climate statistics of the simulated fields uses a temporal and spatial scale decomposition. For the temporal decomposition, a given variable φ is split into its time mean, denoted by an overbar, and its time deviation denoted by a prime:

$$\varphi(t) = \overline{\varphi} + \varphi'(t) \ , \tag{3}$$

therefore,

$$\overline{\varphi^2} = \overline{\varphi}^2 + \overline{\varphi'^2} \ . \tag{4}$$

The first term on the right-hand side is related to the stationary part of the flow and the second term is related to its temporal variability. The square root of $\overline{\varphi'^2}$ is called the transient eddy standard deviation of φ and is used to characterise the storminess activity of the simulations. Similarly to the temporal decomposition, we decompose the total field φ into two spatial components:

$$\varphi = \varphi_{ls} + \varphi_{ss} \ , \tag{5}$$

where φ_{ls} and φ_{ss} are respectively the large and small spatial scale components. The spatial dimensions of the small scales have been chosen to correspond to the dimensions of the small scales that have been filtered out from the initial and lateral boundary conditions (see the response curve on Fig. 4). Combining (4) and (5) gives

$$\overline{\varphi^2} = \overline{\varphi_{ls}}^2 + \overline{\varphi_{ss}}^2 + \overline{\varphi_{ls}'^2} + \overline{\varphi_{ss}'^2} + 2\overline{\varphi_{ls}\varphi_{ss}} + 2\overline{\varphi_{ls}'\varphi_{ss}'} \ . \tag{6}$$

The second and the fourth terms of the r.h.s of (6) are of particular interest because they represent the contributions to the stationary and transient eddies due exclusively to the small-scale features. In light of this, for both the Big and the Little Brother, we will present maps of the following quantities:

1. $\overline{\varphi}$: monthly mean of the total fields,

2. $\sqrt{\overline{\varphi'^2}}$: transient eddy standard deviation of the total fields,

3. $\overline{\varphi_{ss}}$: the small-scale stationary components of the fields,

4. $\sqrt{\overline{\varphi'^{\,2}_{ss}}}$: transient eddy standard deviation of the small-scale components of the fields.

The comparison of the Little and Big Brother with regard to these four geographically distributed climate fields will be objectively measured by the use of spatial correlation coefficients. For a given variable φ, a correlation skill score is defined as

$$R = \frac{\sum_{i,j}\left(\varphi^L_{i,j} - \langle\varphi^L\rangle\right)\left(\varphi^B_{i,j} - \langle\varphi^B\rangle\right)}{\left(\sum_{i,j}\left(\varphi^L_{i,j} - \langle\varphi^L\rangle\right)^2\right)^{1/2}\left(\sum_{i,j}\left(\varphi^B_{i,j} - \langle\varphi^B\rangle\right)^2\right)^{1/2}}, \tag{7}$$

where

$$\langle\varphi\rangle = \frac{\sum_{i,j}\varphi_{i,j}}{N} \tag{8}$$

is the spatial average taken over the N grid-points (denoted by the i and j indices) of the little-brother domain excluding the nesting zone. The superscripts L and B refer to the Little and Big Brother, respectively.

To complete the assessment of the little-brother ability in reproducing the stationary and transient climate behaviour, we define two variance ratios that are derived by first applying a spatial averaging operator to (6). Since the Fourier filter that we employ to segregate the scales makes use of orthogonal functions, the domain average of the product of large and small-scales vanishes, then

$$\left\langle \overline{\varphi^2} \right\rangle = \left\langle \overline{\varphi_{ls}}^2 \right\rangle + \left\langle \overline{\varphi_{ss}}^2 \right\rangle + \left\langle \overline{\varphi_{ls}'^2} \right\rangle + \left\langle \overline{\varphi_{ss}'^2} \right\rangle . \tag{9}$$

We define the ratio of domain-averaged stationary small-scales variances as

$$\Gamma_{ss}^{stat} = \frac{\left\langle \overline{\varphi}_{ss}^{\ 2} \right\rangle^L}{\left\langle \overline{\varphi}_{ss}^{\ 2} \right\rangle^B} , \tag{10}$$

and the ratio of domain-averaged transient small-scale variances as

$$\Gamma_{ss}^{trans} = \frac{\left\langle \overline{\varphi_{ss}'^{\ 2}} \right\rangle^L}{\left\langle \overline{\varphi_{ss}'^{\ 2}} \right\rangle^B} . \tag{11}$$

The variance ratio Γ_{ss}^{stat} and Γ_{ss}^{trans} will give us an indication of the ability of the Little Brother in regenerating the spatial variance of the stationary and transient big-brother small scales.

i. The sea level pressure fields.

The first fields to be presented are the monthly mean sea level pressure ($\overline{slp}$) fields (Fig. 9a). These are shown on the little-brother domain as will be the other fields to be shown. The similarity between the Big and Little Brothers is striking and supported by a high correlation coefficient (*R*) of 0.99. The most noticeable features that have survived the time averaging procedure is a trough over the Great Lakes. This trough is due to the dominant northwesterly flow that carried cold air over the relatively warm lakes compared to the bordering lands. Fig 9b displays the small-scale stationary component of slp. In addition of the Great Lake low-pressure effect, it can been seen that the Appalachian ridge induced stationary ridging and troughing on the upwind and downwind sides, respectively. The agreement between the Little and Big Brother is good again with $R = 0.88$. The correlation is somewhat less when only the ocean area is considered ($R = 0.75$). That is not surprising since few stationary small-scale forcings are present over the ocean.

Fig. 10a shows the transient eddy standard deviation of the slp ($\sqrt{\overline{slp'^2}}$). The fields exhibit a high level of similarity ($R = 0.99$) but the maximum activity is somewhat displaced toward the south in the Little Brother. This maximum is due to systems coming from the continent and intensifying over the ocean. Fig 10b shows the transient eddy standard deviation of the small-scale component of slp. The first most noticable characteristic of this is that a large part of it is over the ocean whereas the stationary small-scale component was mostly over land. But as for the stationary small scales the agreement seems good with R between 0.85 and 0.90.

Table 1 displays the variance ratios defined by Eqs. (10) and (11). Overall the Little Brother does a good job in reproducing the stationary and the transient variances of the big-brother slp, except perhaps over the ocean where the Little Brother has somewhat less variance ($\Gamma_{ss}^{stat} = 0.86$ and $\Gamma_{ss}^{trans} = 0.91$).

ii. The 975-hPa temperature fields.

Fig. 11a shows the monthly mean temperature fields ($\overline{T}$) at 975 hPa. The Big and Little Brother show strong similarities ($R = 0.99$), at least for the large-scale aspect of the fields. Fig 11b shows $\overline{T_{ss}}$, the stationary small-scale component of the temperature fields. The effect of the Great-Lakes heat source can easily be seen, especially south-eastward of the lakes due to the heating of the prevalent north-west cold flow during the month. Another example of regional features can be seen over the Florida peninsula where the land is colder than the ocean. The correlation coefficients are weaker than for the total stationary field but still high ($R \geq 0.89$) especially over land.

The transient eddy standard deviation of temperature ($\sqrt{\overline{T'^2}}$) at 975 hPa are shown on Fig.12a. Both fields are very similar (R = 0.99) with a maximum over the north and a relative minimum over the Great Lakes which exert a damping effect on the temperature fluctuations in both simulations. Fig. 12b shows $\sqrt{\overline{T_{ss}'^2}}$ which represents the temporal variability due to small-scale temperature perturbations. Even though the details are not always the same, both simulations show greater activities over the continent than over the ocean. It is worth noting that over the ocean, excluding the nesting zone, the activity exhibits a quasi-uniformly distributed variance in both simulations: this is probably associated with the convective activity generated by cold air advection over warm water.

Table 2 displays the variances ratios for the stationary and transient small-scale components for the 975-hPa temperature. As it can be seen, the Little Brother is successful in reproducing its Big Brother.

iii. Precipitation rate fields.

As for the low-level temperature, precipitation is a very important input climate quantity for regional climate impact studies, but it is also a very demanding quantity to simulate correctly because it is the end-product of multiple physical and dynamical processes in a model. Furthermore, precipitation is not directly driven at the lateral boundaries as winds, temperature and moisture are.

Fig. 13a shows the monthly mean precipitation rate. Most of the activity took place over the ocean. The overall patterns are in good agreement ($R \geq 0.90$), except of course within the nesting zone. Very fine details are often dissimilar due to the noisy nature of that field. This is especially true over the ocean where no localised surface forcings are present. Despite of this, the mesoscale signature formed by three branches and joining south-east of the Canadian Maritimes is fairly well reproduced by the Little Brother. It must be noted that an averaging period of one month does not seem long enough to remove fingerprints of intense precipitation events associated with travelling weather systems. An average over more events would render a more large-scale pattern. Nevertheless the reproduction of these events is a good preliminary condition to get reasonable long-term means.

Fig 13b shows the stationary small-scale component of the precipitation rate. The figure shows well the noisiness of that field but the just described feature off the Canadian Maritimes is quite visible in both simulations. Besides that feature, the Little Brother has difficulties in positioning the small-scale precipitation features especially over the ocean. The correlation for ocean area is weak ($R = 0.40$). It is better over land but not very high ($R = 0.60$). It is important to note again that this apparent deficiency would probably be reduced by a longer averaging period. Many of the small-scale features present on fig. 13b are in fact one-time events and not really stationary.

The time variability of the precipitation rate is shown on Figs. 14a-b. The patterns are similar but there are some noticeable differences. For instance, the southward tongue of precipitation variability is somewhat weaker in the Little Brother case. The correlation coefficients are reasonable with values between 0.80 and 0.90.

Table 3 shows the variance ratios for the precipitation rate. All ratios are close to one. It is worth noting that even though the stationary small-scale precipitation features were not highly correlated, the Little Brother is successful in reproducing the spatial variance of its Big Brother. The temporal variability due to the small scales is also very well reproduced by the Little Brother.

iv. The 500-hPa vorticity fields.

Up to this point we have examined fields that can be strongly influenced by surface forcings. On the other hand, the relative vorticity at 500 hPa is much less directly influenced by surface heterogeneities and is more driven by the nonlinear dynamics of the free atmosphere. Furthermore, the 500-hPa vorticity field has non-negligible small-scale features for a field at that altitude. It is therefore a good candidate to see if the Little Brother is reliable in reproducing its Big Brother away from surface forcings.

Fig. 15a shows the monthly mean average of the 500-hPa relative vorticity and Fig. 15b its small-scale components. While the Little Brother is able to reproduce the stationary large-scale features successfully ($R \geq 0.95$) away from the boundaries, it is a different story for the small-scales features. Firstly, they are absent not only from the relaxation zone along the western boundary but over a much larger region on the western side of the domain. Secondly, as for the stationary small-scale component of the precipitation rate, the spatial distributions show randomness which is expressed by the low correlation coefficients ($R \leq 0.45$). In fact, the lowest correlation found in this study is for that field over the ocean (R =0.35). Many of the small-scale features over the ocean have small amplitudes and are not really stationary; a longer averaging period should result in smoother fields and improved correlations.

Figs. 16a-b shows respectively the transient eddy standard deviation of the total and small-scales relative vorticity. The first noticeable characteristic on both Figures is again the lower amplitudes in the little-brother case. On the other hand, the patterns are fairly similar except over the land where R = 0.73 and R = 0.52 for the total and the small-scale transients, respectively.

Table 4 displays the variance ratios Γ_{ss}^{stat} and Γ_{ss}^{trans} for the 500-hPa relative vorticity. As perceived from figs 15b and 16b, the Little Brother has weaker stationary and transient small-scale features especially over the continent. This is probably because it takes a longer distance than the width of the relaxation zone to regenerate small-scale vorticity from large-scale systems entering from the western boundary.

4. Discussion

In a review of the evolution of the regional climate modelling research, Giorgi and Mearns (1999) argued that despite all the potential pit-falls, past and current experiences with RCM has shown that the one-way nesting strategy is a workable solution. They suggest that validation tests should be made before doing more elaborate and costly simulations. One of them consists in verifying that the RCM satisfactorily simulates the current climate when driven by objective analyses of observations. It is this framework of validation that the project to intercompare regional climate simulations (PIRCS) provides. The major problem with this framework is the validation of mesoscale features. In effect, climate observation networks are usually at a too low resolution to permit a real validation of the mesoscales especially away from the surface. Furthermore, as with any model, RCMs make approximations in solving the field equations and these make their simulated climate imperfect. These imperfections are distinct from those related to the nesting, and consequently call for validation approaches that can isolate them.

This motivated us to adopt a perfect-prognosis approach that we called the Big-Brother Experiment. In this experiment the RCM output, in particular the small-scales, are verified against a virtual, model-generated reality. The BBE is a basic experiment that permits to verify whether the small scales generated by the nested RCM are reasonable compared to the small scales present in the virtual reality reference. We view this validation experiment as a necessary, but not necessarily sufficient condition, for claiming that the one-way nesting strategy is an acceptable method for regional climate modelling. Moreover, we have addressed only a subset of the issues listed in the introduction namely: the numerical nesting formulation, the effect of the resolution jump, the atmospheric spin-up and their possible effect on a climate drift or systematic errors. The results have been exposed in two parts: The first part of the results gave us a subjective assessment of how the Little Brother assimilated the driving large-scale information and how it regenerated the small scales. The second part looked at the model "climate" downscaling ability. The rational of this two-part approach is this: During the first few days, gross errors, noise or a lack of regenerating small scales can be easily diagnosed and attributed. On the other hand, some errors need time to accumulate or to be diagnosed as long-term tendency errors. We review and discuss next what has been found from these two parts.

a. Small-scale generation and spin-up

We have estimated that the spin-up time for the low-level atmospheric dynamics was around 24 hours. During this time the Little Brother regenerated small scales from initial conditions which were only constituted of large and synoptic scales (see Figs 5-6). This regeneration of small-scale activity in the lower troposphere was observed not only over the continent where surface forcings at these small scales are present, but also over the ocean. This means that the downscaling ability of the nesting strategy does not depend necessarily only on the small-scale surface forcings. The nonlinear internal atmospheric dynamics and hydrodynamic instabilities also play a role.

During that first five days no spurious noises or gross errors emanated from the boundary. Of course, the activity was weak in the relaxation zone due to the imposed forcing of the large-scale flow. It is worth noting that different conclusions would be obtained if the Big and Little Brothers did not shared the same model formulation. In effect, problems might have had more chance to appear at the outflow boundary since the weather systems in the nesting and nested models would more likely travel at different speeds. Our prefect-prognosis approach avoids such problems.

b. Climate downscaling ability

We looked at four different climate fields to analyse the climate downscaling ability produced by a one-month simulation. First, we looked at the sea level pressure (slp). This variable is a basic variable to look at since it displays the atmospheric mass behaviour during the month. The monthly mean and the transient standard deviation of the small-scale component of slp (Figs 9b-10b and tables 1) showed that the Little Brother successfully reproduced the small-scales especially over land where surface forcing such as water masses and mountains play an important role.

Low-level temperature and precipitation variables are of great interest for characterising regional climate. The 975-hPa temperature small-scales fields (Figs 11b, 12b) showed, that the Little Brother had abilities in reproducing regional features. The precipitation fields (Figs 13a-b, 14a-b) show good results also except for the stationary part of its small-scale components over the ocean where atmospheric convection is active. However with longer simulations, we expect smoother precipitation fields with weaker stationary small-scale variances over the ocean.

To assess the Little Brother downscaling ability away from surface forcings we looked at a 500-hPa relative vorticity. This field highlights better the small-scale structure of the flow than the velocity field. Its analysis is therefore more revealing of the small-scale dynamics of the free atmosphere. We found that, while the Little Brother was able to reproduce monthly mean large-scale features of the vorticity, it shows some weaknesses in regenerating its small-scale spatial and temporal variability (Figs 14b, 15b and table 4). It could be that the domain size (issue 7) was not large enough for the Little Brother to fully regenerate all the small-scale variability of systems entering into the domain. The correlation coefficients for the stationary small-scale components are especially low over the ocean. But again, this may not be surprising since no stationary forcings are present there. We expect that with longer simulations this stationary component will decrease in amplitude. On the other hand, the correlation of the time variability, i.e. the small-scale disturbance activity of the flow, is well simulated, although somewhat weaker. Even though the Little Brother had more difficulty with the relative vorticity field, these weaknesses did not have a noticeable impact on the surface climate.

To diagnose possible drifts in the little-brother simulation, we present on Fig.17 time series of the precipitation rates averaged over the domain excluding the relaxation zone. We can see that the Little Brother does not drift or deviate significantly from the Big Brother. Over the whole month, excluding the spinup period, the Little Brother produced similar total precipitation compared to the Big Brother: 116 mm versus 120 mm. The same conclusion can be draw from the time series of low-level temperatures (not shown). Concerning the ability of the Little Brother to reproduce the big-brother small scales, we found that the Little Brother was generally very good. The only exception we found is the relative vorticity away from strong surface forcing (see Figs 15b and 16b). Fig 18 shows time series of the spatial variance of the small-scale relative vorticity at 500 hPa. We see that the Little Brother has negative bias most of the time. Nevertheless, this weakness did not seem to have a negative impact on other variables such as precipitation and temperature.

Our findings about the robustness of the surface mesoscale reproducibility are in line with those of Noguer et al. (1998). They showed that, even though their RCM simulations had large-scale biases originating from the driving GCM, the mesoscale component of the surface air temperature and precipitation were relatively insensitive to the errors of the driving GCM. This owes to the fact that the verification was done only over land where stationary topographic and coastal forcings are important. Furthermore the biases in the driving circulation, although significant, were apparently not strong enough to induce significant storm track modification as anticipated in issue 8.

c. Future work

In this paper, we proposed a clean experimental framework, called the big-brother experiment, to assess the one-way nesting strategy. As an example of application we investigated issues one, two, three and nine, but we studied just one configuration of the operating nesting. In effect, we studied only one resolution jump, one domain size, one update frequency, one region and one season. The robustness of the present conclusion needs to be tested for different locations on the globe (mid-latitude versus tropical or polar regions, land versus ocean, mountainous versus modest orography regions) and different seasons. The impact of the domain size and the update frequency are also issues that can be investigated within the context of the big-brother experiment. Experiments involving comparison with double nesting would also be of interest.

5. Conclusions

The main objective of this study was to test the hypothesis under which RCMs are employed, namely:

"Can one-way nested RCMs accurately simulate fine-scale climate features when driven by large-scale information only."

To circumvent the lack of mesoscale observations for validating the above hypothesis and to separate nesting errors from model errors, we designed an experiment called "the Big-Brother Experiment" in which one-way nested RCM outputs have been compared to a high-resolution virtual reality. This experiment has been carried out with a resolution jump of about 6. Our findings of the first few days and the climate statistic of a single month with emphasis on the small scales lead us to these conclusions:

- Small-scale low-level features absent from the initial and lateral boundary conditions are almost fully re-generated by the one-way nested RCM within the first day.

- Mesoscale features of sea level pressure and low-level temperature are simulated with a high level of accuracy by the one-way nested RCM. This conclusion applies as well to the mesoscale stationary features as to their time variability.

- The downscaling ability for the stationary precipitation patterns shows some skill except over areas dominated by stochastic convective activity. The time variability of precipitation is well reproduced.

- Some weaknesses has been noted in the middle troposphere for the relative vorticity field where its time variability cannot be fully recovered by the RCM. This suggests that the nested domain we employed might not have been large enough. The simulated climate as seen by the sea level pressure, low-level temperature and precipitation variables however did not appear to suffer from that.

- Finally and maybe not surprisingly, surface heterogeneities play a great role in determining stationary mesoscale climate features. Small-scale activities generated by nonlinear dynamics of the atmosphere, i.e. the cascade of information from the large-scale flow, is also generally well simulated by the one-way nesting RCM. But its spatial pattern has a more random behaviour than for the small scales directly forced by stationary surface forcings.

These conclusions have been drawn from only one specific big-brother experimental configuration. Further experiments need to be performed for studying the impact various parameters such as the geographical domain (size and location), the season, the nesting resolution jump, the update frequency, etc.

Acknowledgements

This work has been financially supported by funding from the USDOE Climate Change Prediction Program (CCPP) and the UQAM regional climate modelling group. We gratefully acknowledge the Meteorological Service of Canada for granting an education leave to the first author during this study and for providing access to its facilities. We are thankful to the UQAM regional climate modelling staff for their precious technical help with the Canadian RCM. We also thank Drs. Bernard Dugas and Ramón de Elía for stimulating discussions.

References

Baumhefner, D. P., and D. J. Perkey, 1982: Evaluation of lateral boundary errors in a limited domain model. *Tellus*, **34**, 409-428.

Bergeron, G., R. Laprise, and D. Caya, 1994: *Formulation of the Mesoscale Compressible Community (MC2) model.* Cooperative Centre for Research in Mesometeorology, 165 pp., [Available from Dr. D. Caya, Groupe des Sciences de l'Atmosphère, Département des Sciences de la Terre et de l'Atmosphère, Université du Québec à Montréal, C.P. 8888, Succursale "Centre-Ville," Montréal, PQ, H3C 3P8, Canada]

Biner, S., D. Caya, R. Laprise, and L. Spacek, 2000: Nesting of RCMs by imposing large scales., 7.3-7.4. In: Research activities in Atmospheric and Oceanic Modelling, WMO/TD - No. 987, Report No. 30.

CAS/JSC WGNE, 1999: *Report of Fourteenth Session of the CAS/JSC Working Group on Numerical Experimentation (Recherche en Prévision Numérique, Environnement Canada, Doval, Québec, Canada, 2-6 November 1998)*, No. 14, WMO/TD-NO. 964, World Meteor. Org., 28 pp.

CAS/JSC WGNE, 2000: *Report of Fifteenth Session of the CAS/JSC Working Group on Numerical Experimentation (Naval Research Laboratory, Monterey, CA, USA, 25-29 October 1999)*, No. 15, WMO/TD-NO. 1024, World Meteor. Org., 29 pp.

Caya, D., and R. Laprise, 1999: A semi-implicit semi-Lagrangian regional climate model: The Canadian RCM. *Mon. Wea. Rev.*, **127**, 341-362.

Christensen, O. B., J. H. Christensen, B. Machenhauer, and M. Botzet, 1998: Very high-resolution regional climate simulations over Scandinavia-present climate. *J. Climate*, **11**, 3204-3227.

Davies, H. C., 1976: A lateral boundary formulation for multi-level prediction models. *Quart. J. Roy. Meteor. Soc.*, **102**, 405-418.

Davies, H. C., and R. E. Turner, 1977: Updating prediction models by dynamical relaxation: an examination of the technique. *Quart. J. Roy. Meteor. Soc.*, **103**, 225-245.

Denis, B., J. Côté, and R. Laprise, 2001: Spectral decomposition of two-dimensional atmospheric fields on limited-area domains using the discrete cosine transform (DCT). *Mon. Wea. Rev. (submitted).*

Déqué, M., P. Marquet , and R. G. Jones, 1998: Simulation of climate change over Europe using a global variable resolution general circulation model. *Climate Dyn.*, **14**, 173-189.

Fox-Rabinovitz, M. S., G. L. Stenchikov, M. J. Suarez, L. L. Takacs, and R. C. Govindaraju, 2000: A uniform- and variable-resolution stretched-grid GCM dynamical core with realistic orography. *Mon. Wea. Rev.*, **128**, 1883–1898.

Giorgi, F., and L. O. Mearns, 1999: Introduction to special section: regional climate modeling revisited. *J. Geophys. Res.*, **104**, 6335-6352.

Hong, S.-Y., and A. Leetmaa, 1999: An evaluation of the NCEP RSM for regional climate modeling. *J. Climate*, **12**, 592-609.

Houghton, J. T., Y. Ding, D. J. Griggs, M. Noguer, P. J. van der Linden, and D. Xiaosu, 2001: *Climate Change 2001: The Scientific Basis.* Cambridge University Press, 944 pp.

Houghton, J. T., G. J. Jenkins, and J. J. Ephraums, 1990: *Climate Change—The IPCC Scientific Assessment.* World Meteor. Org. / UN Environment Programme, Cambridge University Press, 365 pp.

Jacob, D., and R. Podzun, 1997: Sensitivity studies with the regional climate model REMO. *Meteorol. Atmos. Phys*, **63**, 119-129.

Ji, Y., and A. D. Vernekar, 1997: Simulation of the Asian summer monsoons of 1987 and 1988 with a regional model nested in a global GCM. *J. Climate*, **10**, 1965-1979.

Jones, R. G., J. M. Murphy, and M. Noguer, 1995: Simulation of climate change over Europe using a nested regional-climate model. I: Assessment of control climate, including sensitivity to location of lateral boundaries. *Quart. J. Roy. Meteor. Soc.*, **121**, 1413-1449.

Jones, R. G., J. M. Murphy, M. Noguer, and A. B. Keen, 1997: Simulation of climate change over Europe using a nested regional-climate model. I: Comparison of driving and regional model responses to a doubling of carbon dioxide. *Quart. J. Roy. Meteor. Soc.*, **123**, 265-292.

Kain, J. S., and J. M. Fritsch, 1990: A one-dimensional entraining/detraining plume model and its application in convective parameterization. *J. Atmos. Sci.*, **47**, 2784-2802.

Laprise, R., D. Caya, G. Bergeron, and M. Giguère, 1997: The formulation of André Robert MC2 (Mesoscale Compressible Community) model. The André J. Robert Memorial Volume (C. Lin, R. Laprise and H. Ritchie, Eds.), companion volume to *Atmos.-Ocean*, **35**, 195-220.

Laprise, R., D. Caya, M. Giguère, G. Bergeron, H. Côté, J.-P. Blanchet, G. Boer, and A. N. McFarlane, 1998: Climate and climate change in western Canada as simulated by the Canadian regional climate model. *Atmos.-Ocean*, **36**, 119-167.

Laprise, R., M. K. Ravi Varma, B. Denis, D. Caya, and I. Zawadzki, 2000: Predictability in a nested limited-area model. *Mon. Wea. Rev.*, **128**, 4149-4154.

Leung, L. R., and S. J. Ghan, 1999: Pacific Northwest climate sensitivity simulated by a regional climate model driven by a GCM. Part I: Control simulations. *J. Climate*, **12**, 2010-2030.

McGregor, J. L., 1997: Regional climate modelling. *Meteorol. Atmos. Phys.*, **63**, 105-117.

Noguer, M., R. Jones, and J. Murphy, 1998: Sources of systematic errors in the climatology of a regional climate model over Europe. *Climate Dyn.*, **14**, 691-712.

Risbey, J. S., and P. H. Stone, 1996: A case study of the adequacy of GCM simulations for input to regional climate change assessments. *J. Climate*, **9**, 1441-1467.

Robert, A., and E. Yakimiw, 1986: Identification and elimination of an inflow boundary computational solution in limited area model integrations. *Atmos.-Ocean*, **24**, 369-385.

Seth, A., and F. Giorgi, 1998: The effects of domain choice on summer precipitation simulation and sensitivity in a regional climate model. *J. Climate*, **11**, 2698–2712.

Staniforth, A., 1997: Regional modeling: A theoretical discussion. *Meteorol. Atmos. Phys.*, **63**, 15-29.

Takle, E. S., W. J. Gutowski, Jr., R. W. Arritt, Z. Pan, C. J. Anderson, R. R. da Silva, D. Caya, S.-C. Chen, F. Giorgi, J. H. Christensen, S.-Y. Hong, H.-M. H. Juang, J. Katzfey, W. M. Lapenta, R. Laprise, G. E. Liston, P. Lopez, J. McGregor, R. A. Pielke, Sr., and J. O. Roads, 1999: Project to Intercompare Regional Climate Simulations (PIRCS): Description and initial results. *J. Geophys. Res.*, **104**, 19443-19461.

von Storch, H., H. Langenberg, and F. Feser, 2000: A spectral nudging technique for dynamical downscaling purposes. *Mon. Wea. Rev.*, **128**, 3664–3673.

Waldron, K. M., J. Paegle, and J. D. Horel, 1996: Sensitivity of a spectrally filtered and nudged limited-area model to outer model options. *Mon. Wea. Rev.*, **124**, 529-547.

Walsh, K., and J. L. McGregor, 1995: January and July climate simulations over the Australian region using a limited-area model. *J. Climate*, **10**, 2387-2403.

Warner, T. T., R. A. Peterson, and R. E. Treadon, 1997: A tutorial on lateral boundary conditions as a basic and potentially serious limitation to regional numerical weather prediction. *Bull. Amer. Meteor. Soc.*, **78**, 2599-2617.

Yakimiw, E., and A. Robert, 1990: Validation experiments for a nested grid-point regional forecast model. *Atmos.-Ocean*, **28**, 466-472.

Figures

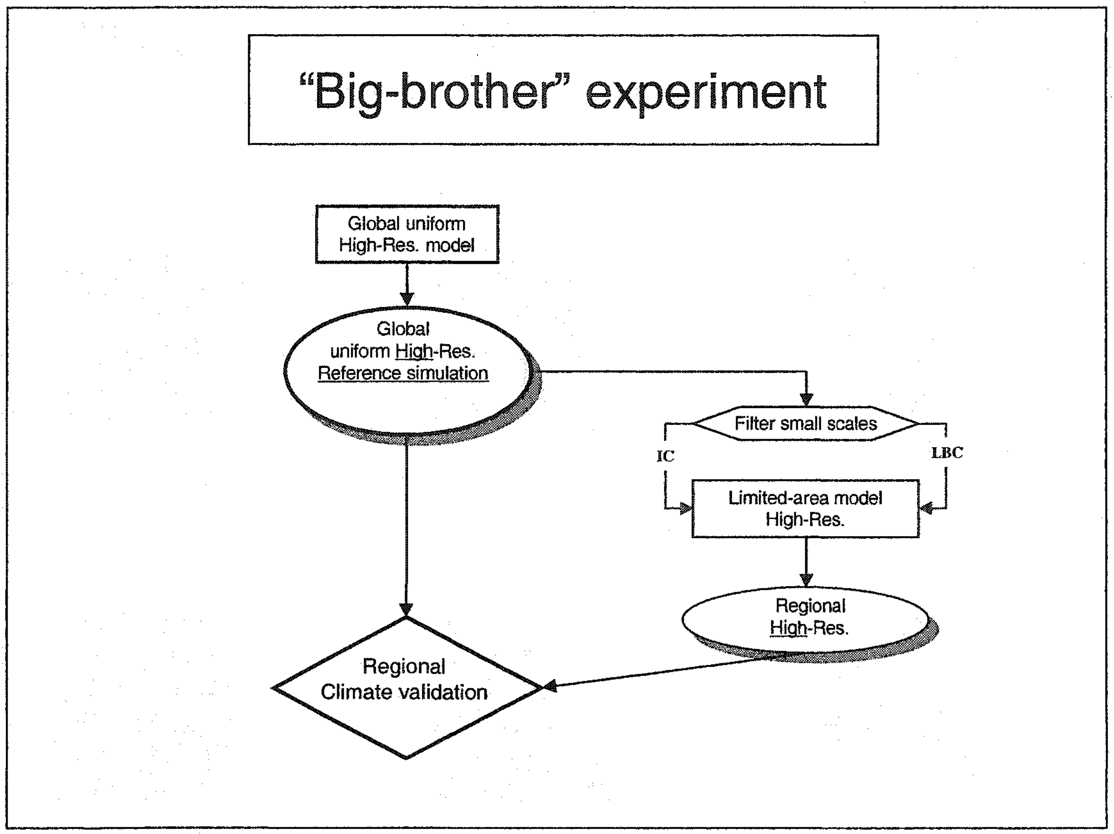

Fig. 1. The big-brother experiment flowchart. Rectangles are the models and ovals are their corresponding datasets. The diamond represents validation of the little-brother regional-scale features against those existing in the reference big-brother dataset. The initial conditions (IC) and lateral boundary conditions (LBC) for LAM (right branch) are spatially filtered such that the small scales are removed.

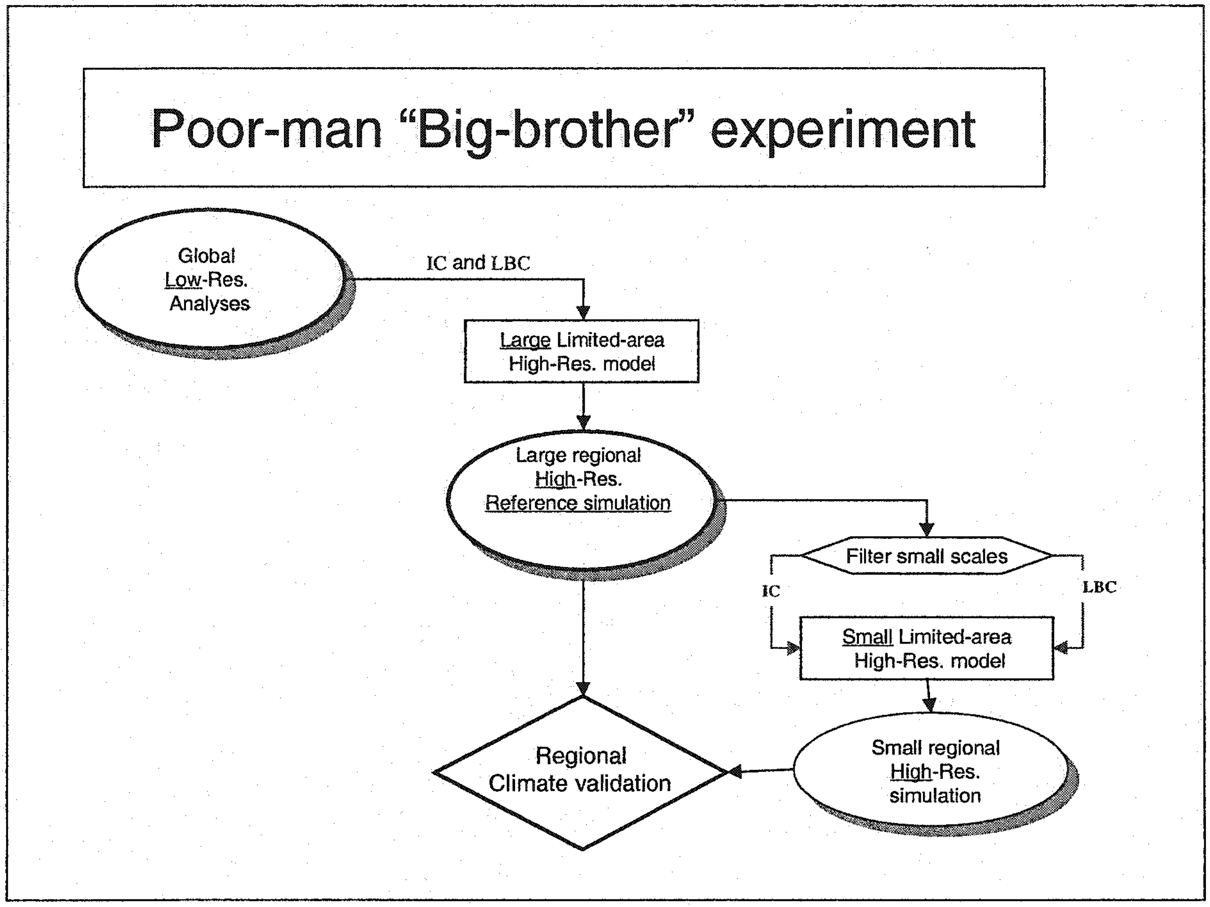

Fig. 2. The poor-man big-brother experiment flowchart. This flowchart is similar to Fig. 1 except that the global uniform high-res. model is replaced by a LAM run over a large domain. The initial conditions (IC) and lateral boundary conditions (LBC) for that large-domain run were taken from global low-resolution analyses.

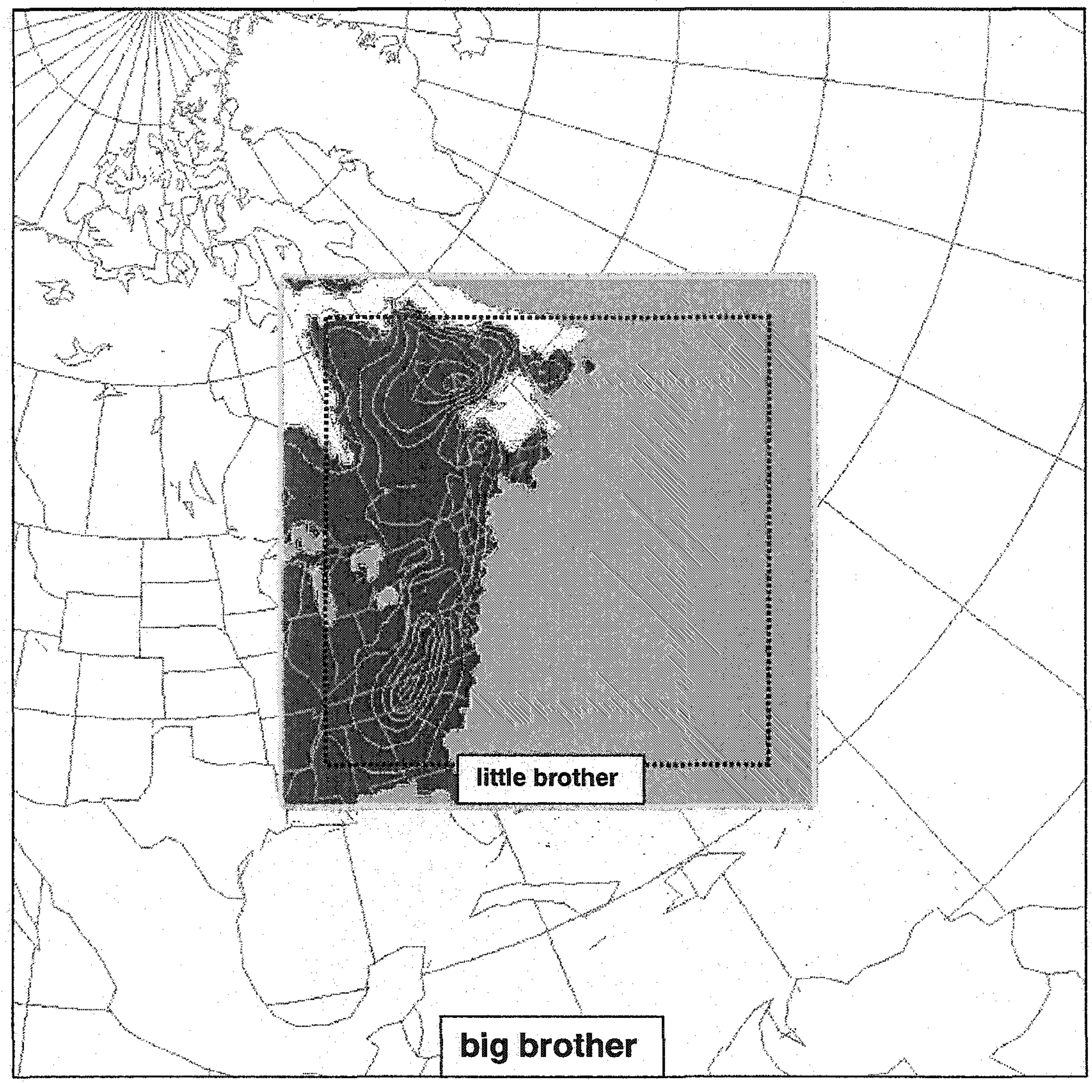

Fig. 3. Geographical layout of the domains. The dashed line around the little-brother domain represents the width of the nesting zone. The topographic field and the land/open-water/sea-ice mask are also shown but only for the Little Brother for clarity. The topography is contoured every 100 m. Open-water areas are shown as grey and sea-ice areas as white.

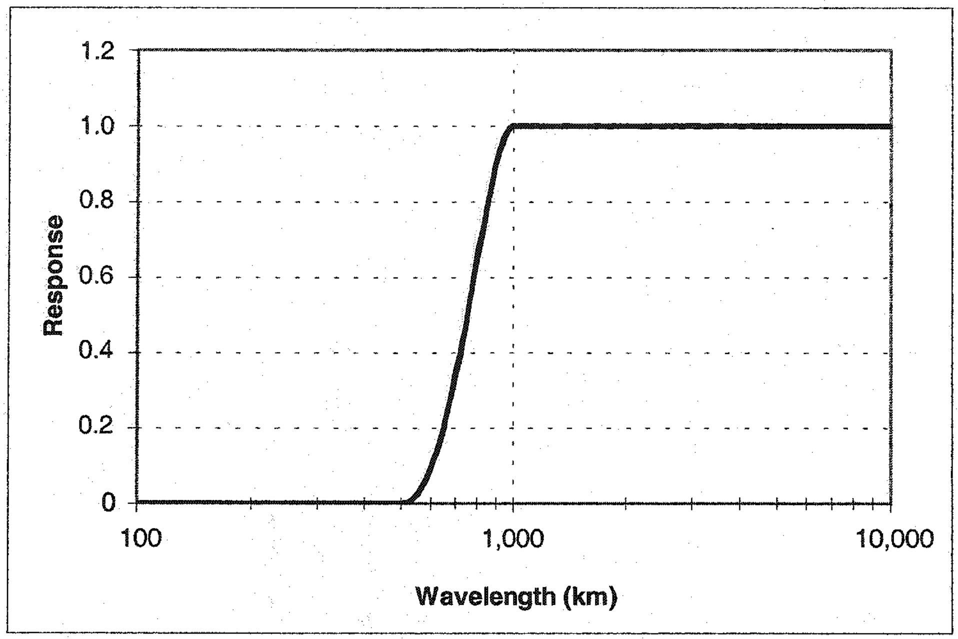

Fig. 4. The response of the low-pass Fourier filter used to remove small scales from the initial and the lateral boundary conditions for the little-brother simulation. The abscissa is logarithmic in wavelength and the ordinate is linear in response.

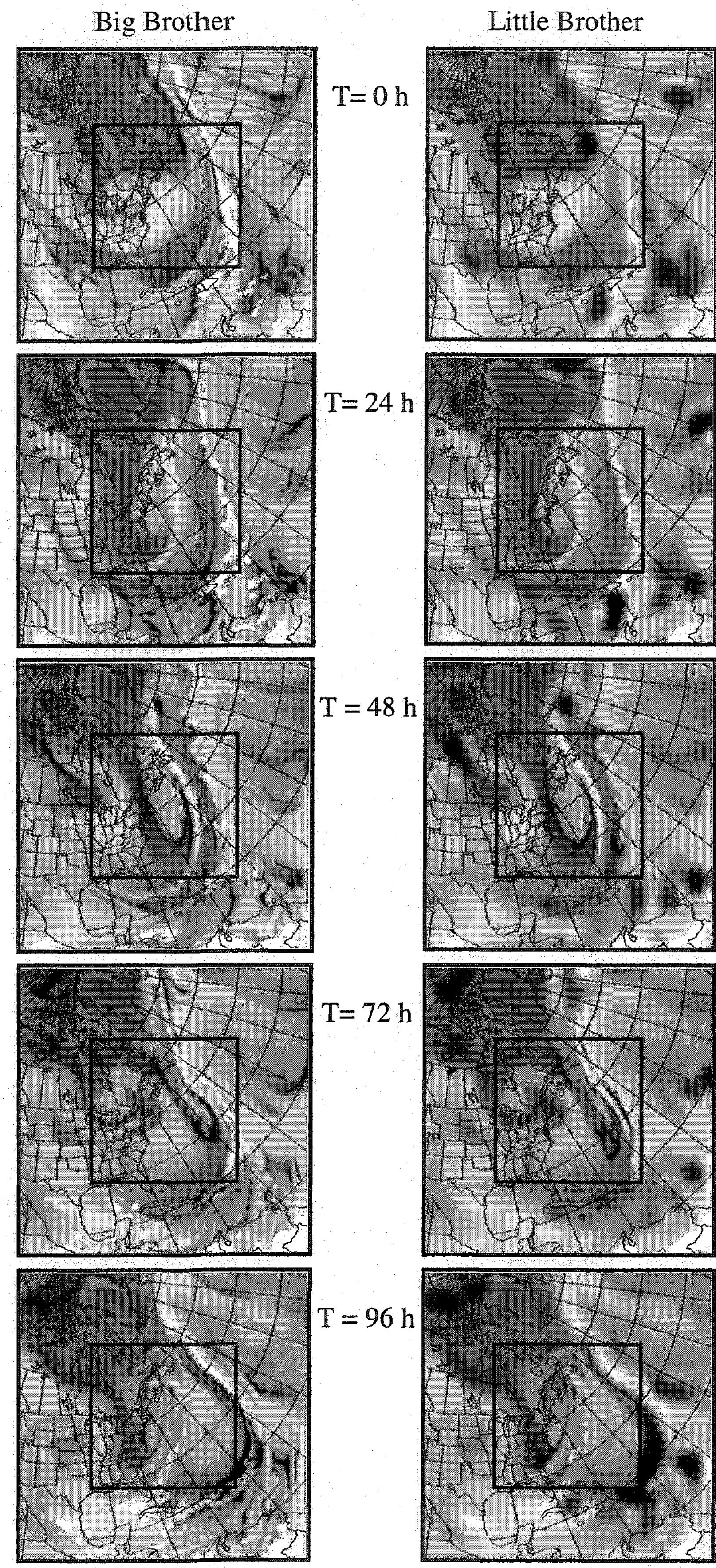

Fig. 5 Evolution of the specific humidity at 700 hPa during the first 96 hours, sampled every 24 hours. The left column is the control Big Brother. The inner squares of the right column correspond to the little-brother domain while the area outside these squares are the filtered big-brother humidity used to nest the Little Brother. The squares are also drawn on the big-brother column to ease the comparison. The large domain (Big Brother) contains 196 by 196 grid points and the inner domain (Little Brother) has 100 by 100 grid points. The grey tones go from black for dry air (0 g kg^{-1}) to bright white for moist air (maximum of 17 g kg^{-1}).

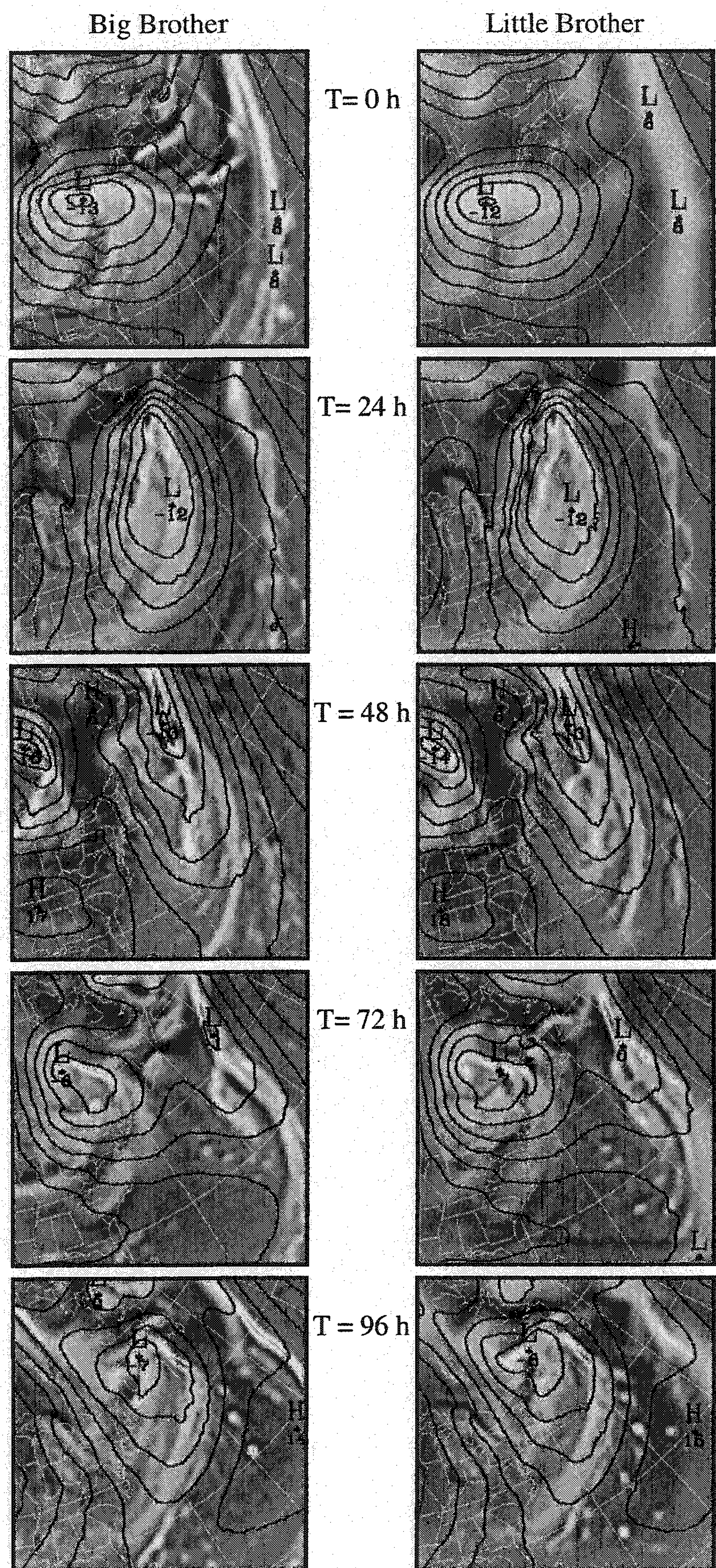

Fig. 6. Evolution of the relative vorticity (grey tones) and the 1000-hPa geopotentiel height field during the first 96 hours, sampled every 24 hours. The left column is the control Big Brother (showed only over the area corresponding to the Little Brother domain). The right column displays the Little Brother. The grey tones go from dark grey for negative vorticity to bright white for positive vorticity. The geopotentiel height fields are contoured every 4 dam.

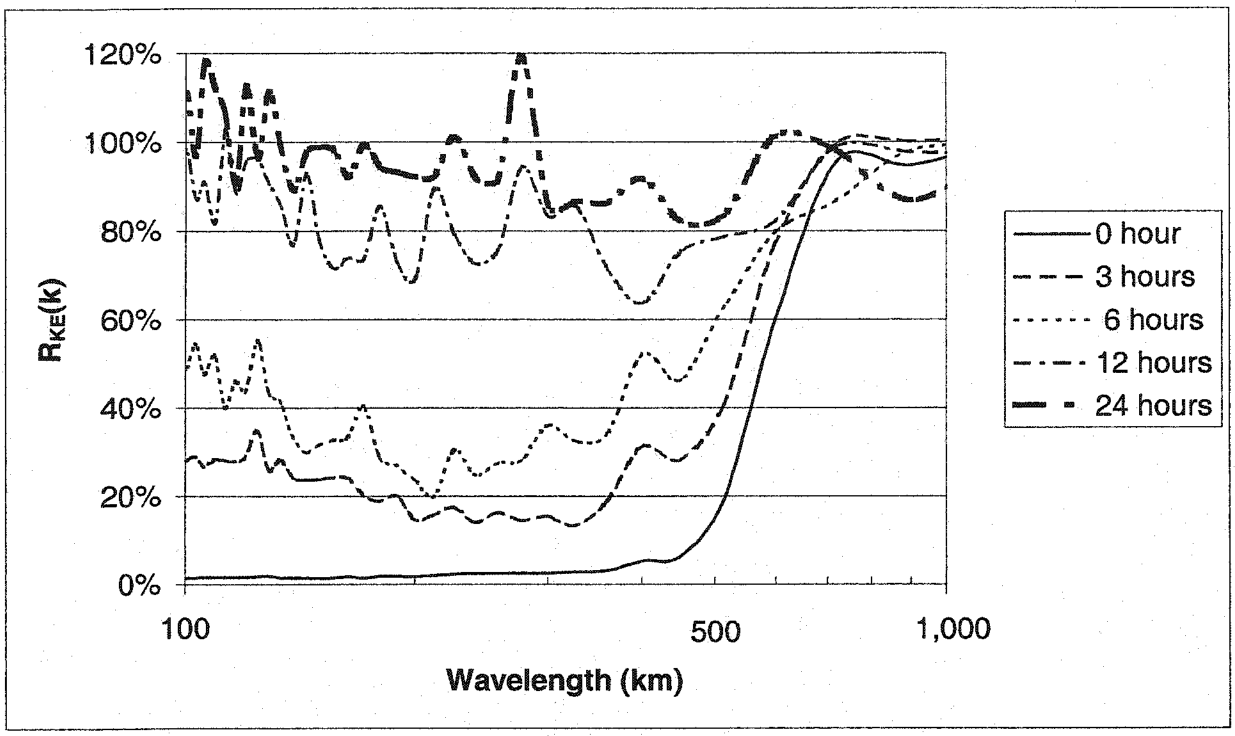

Fig. 7. Ratio (Little Brother/Big Brother) of low-level kinetic energy as a function of scales for different times. The abscissa is logarithmic in wavelength and the ordinate is linear in KE ratio.

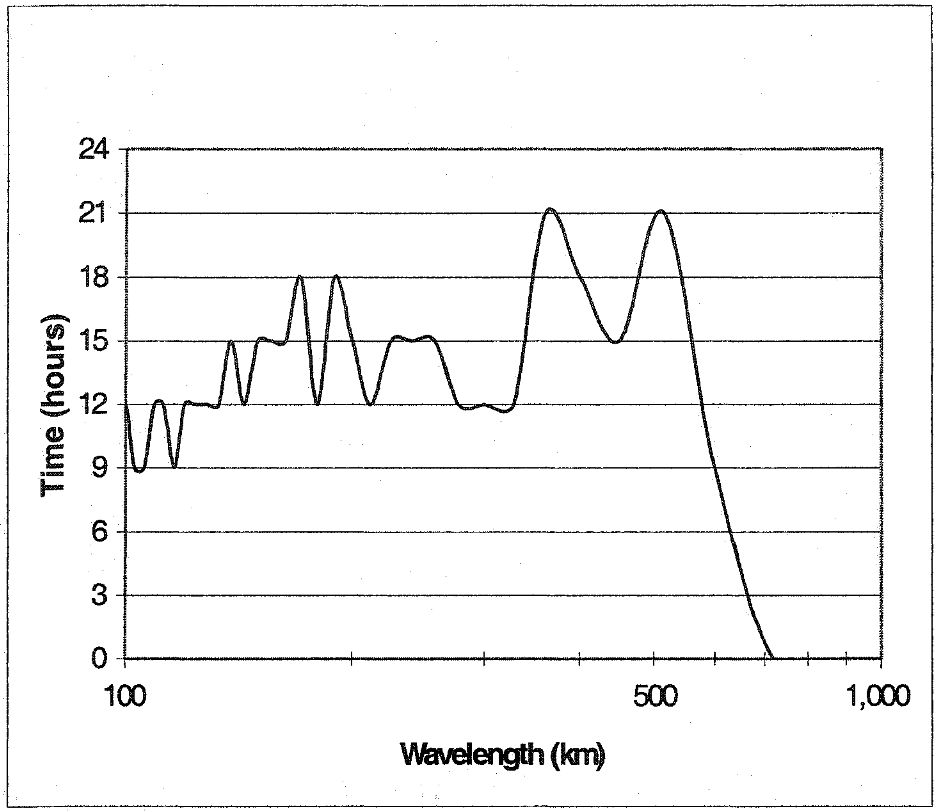

Fig. 8. Spin-up time of low-level kinetic energy as a function of scales. The spin-up time is defined as the time it takes for the kinetic energy in the Little Brother simulation to reach 80% of the big-brother kinetic energy.

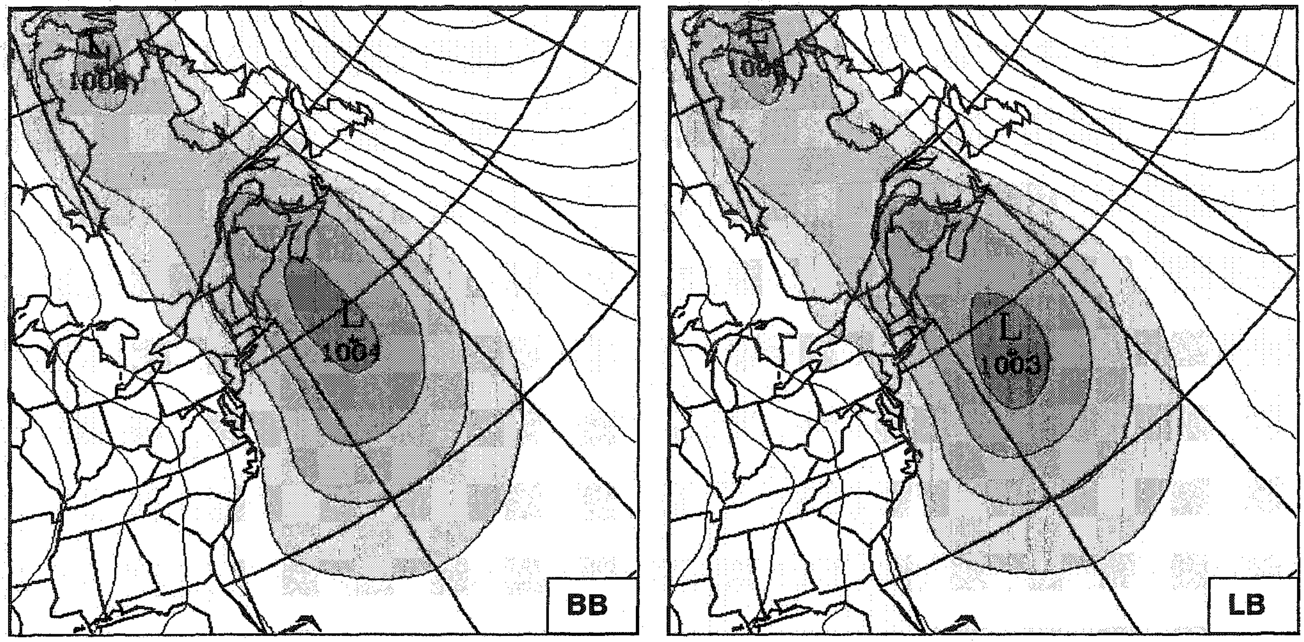

Fig. 9a. Monthly mean slp. The Big and Little Brothers are respectively on the left and the right panel. Contours are every 2 hPa. Areas with values smaller than 1010 hPa are shaded. Correlation coefficient $R = 0.99$. For land only: $R = 0.99$, for ocean only: $R = 0.99$.

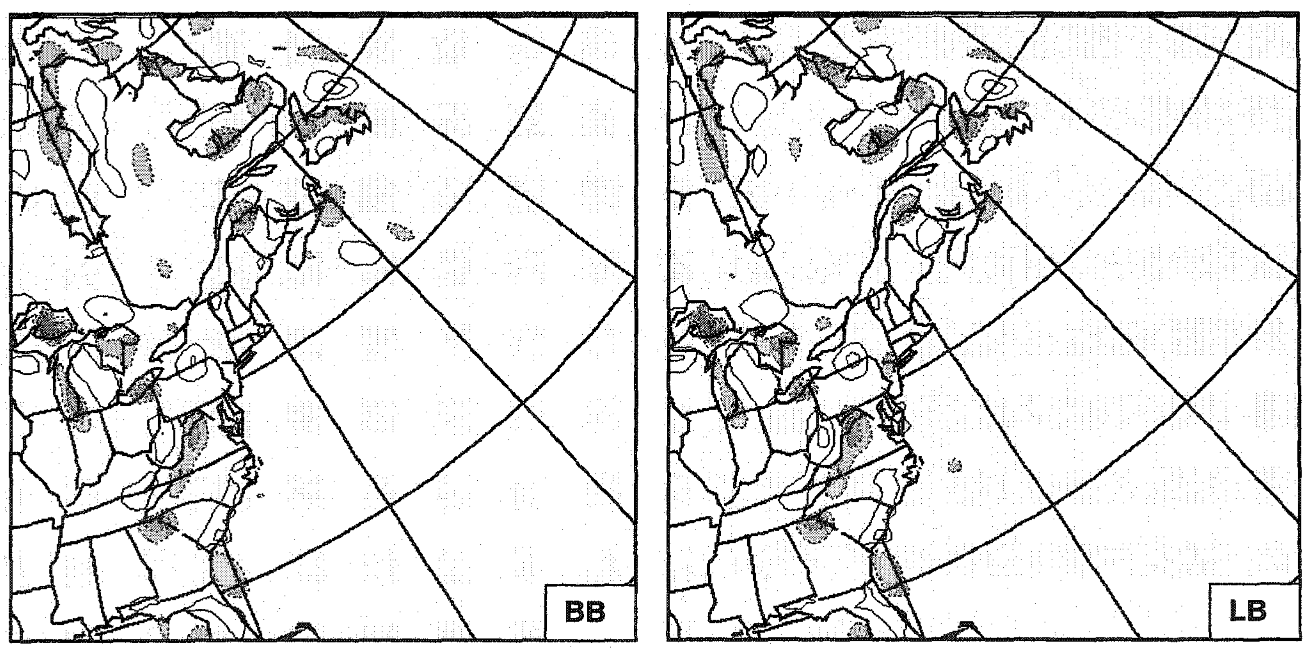

Fig. 9b. Stationary small-scale component of slp. Contour intervals are every 0.1 hPa. The zero contour is omitted. Regions with values smaller than –0.1 hPa are shaded. Correlation coefficient $R = 0.88$. For land only: $R = 0.92$, for ocean only: $R = 0.75$.

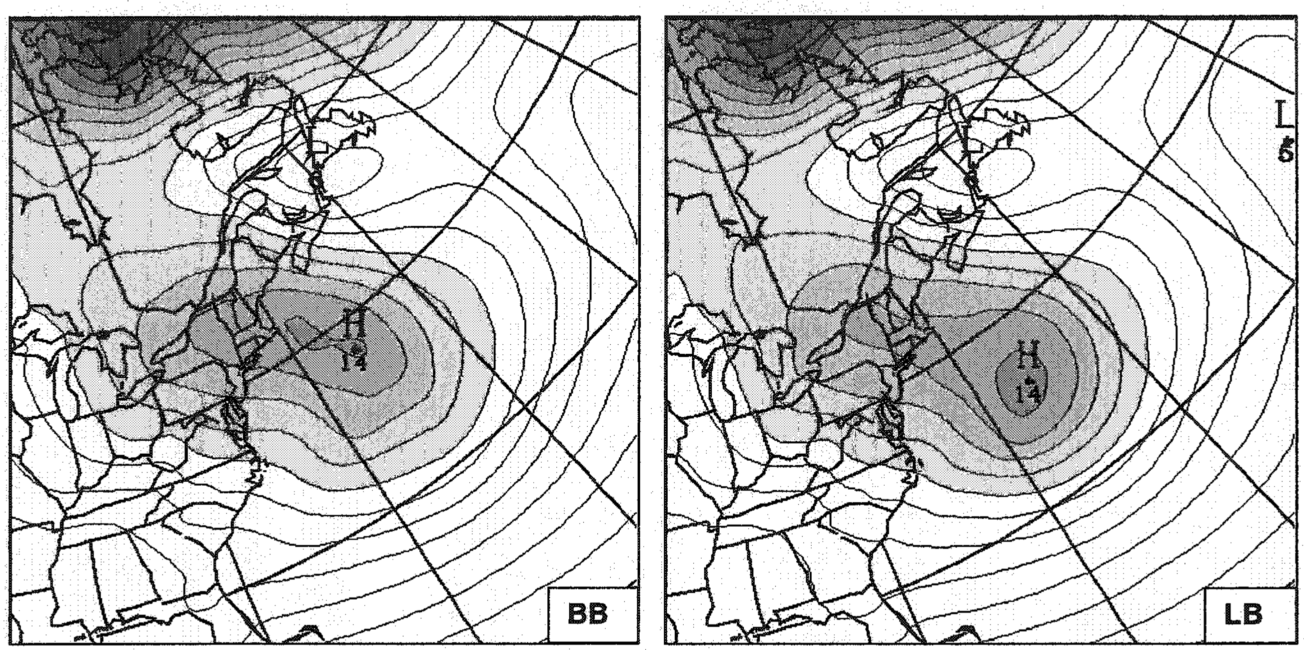

Fig. 10a. Transient eddy standard deviation of slp. Contours are every 1.0 hPa. Regions with values larger than 10 hPa are shaded. Correlation coefficient $R = 0.99$. For land only: $R = 0.99$, for ocean only: $R = 0.99$.

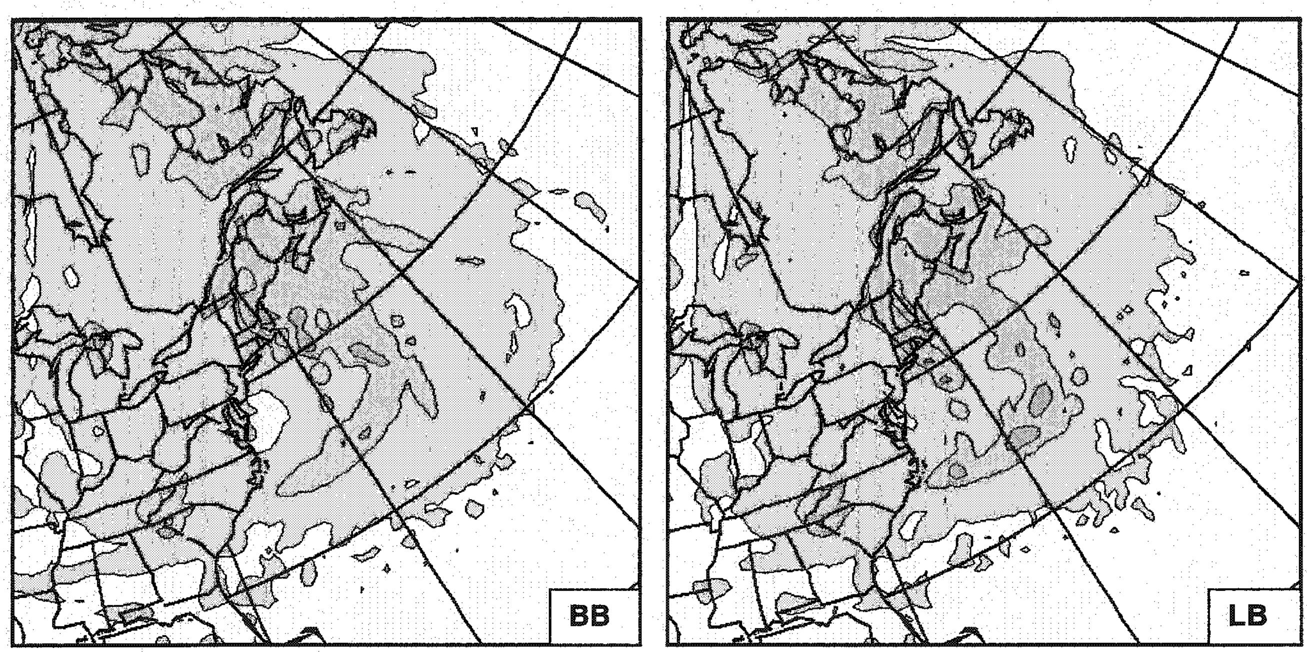

Fig. 10b. Transient eddy standard deviation of the small-scale component of slp. Contours are every 0.2 hPa. Regions with values larger than 0.2 hPa are shaded. Correlation coefficient $R = 0.88$. For land only: $R = 0.90$, for ocean only: $R = 0.85$.

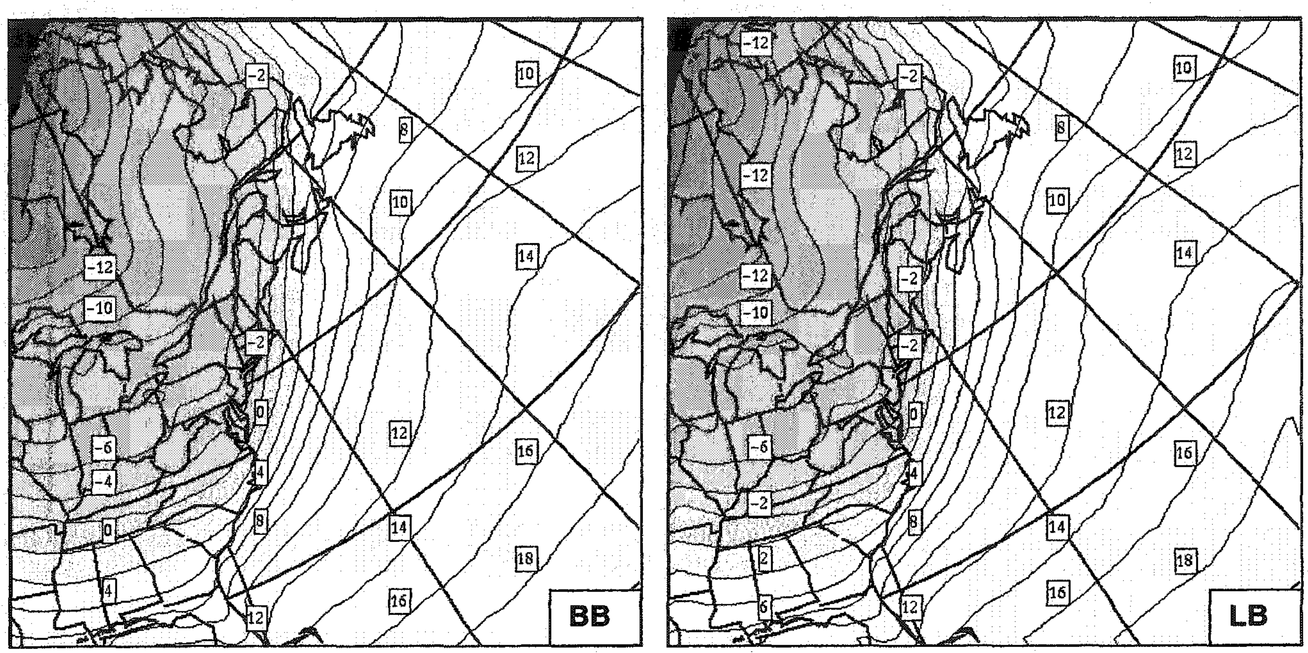

Fig. 11a. Monthly mean temperature at 975 hPa. Contours are every 2 °C. Regions with temperature below zero Celsius are shaded. Correlation coefficient $R = 0.99$. For land only: $R = 0.99$, for ocean only: $R = 0.99$.

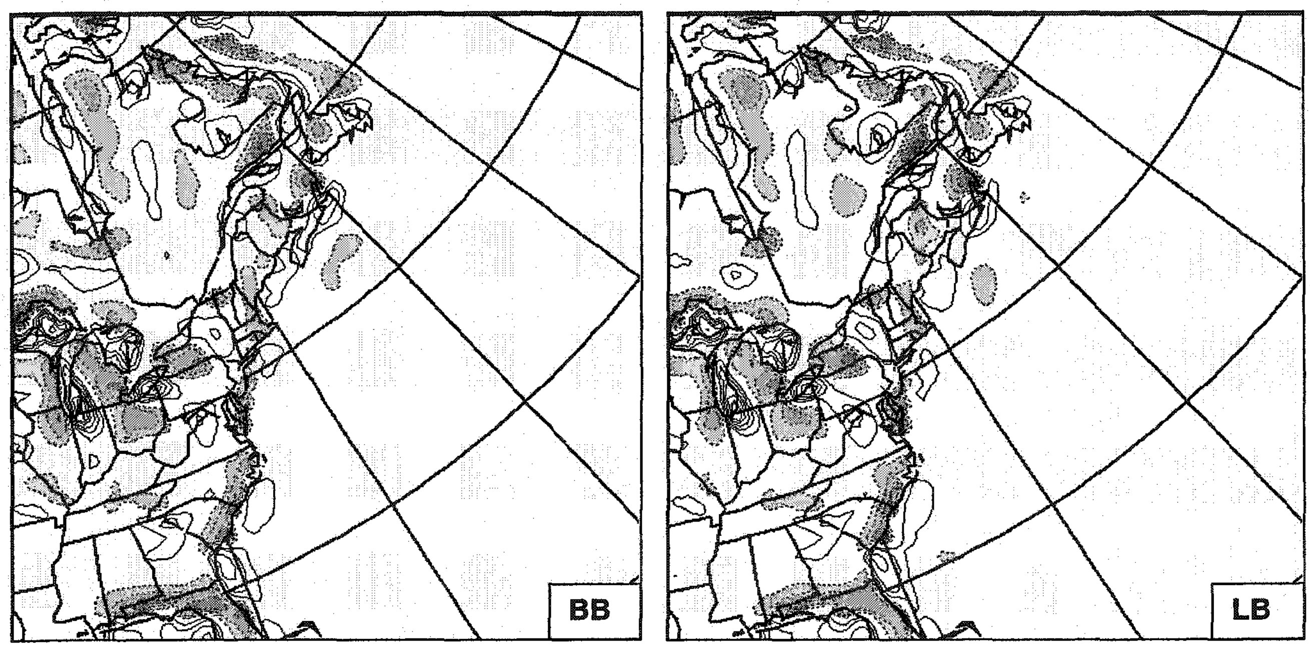

Fig. 11b. Stationary small-scale component of temperature at 975 hPa. Contours are every 0.2 °C. The zero contour is omitted. Regions with values smaller than –0.2 °C are shaded. Correlation coefficient $R = 0.93$. For land only: $R = 0.94$, for ocean only: $R = 0.89$.

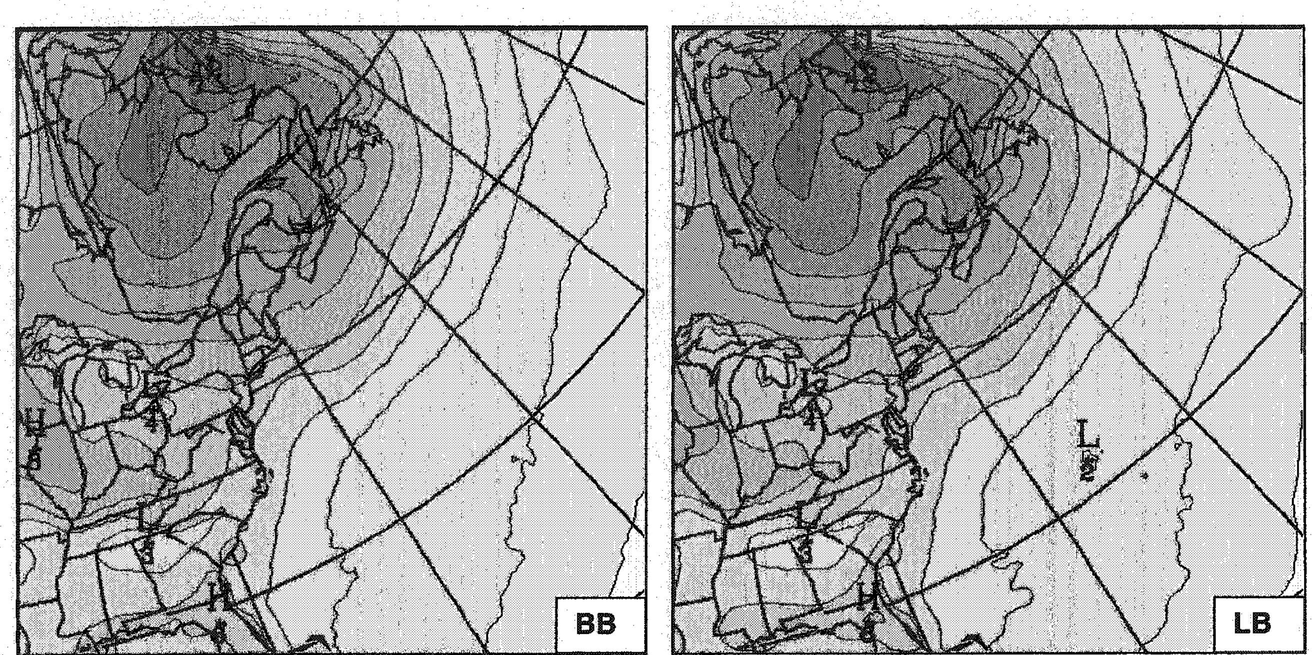

Fig. 12a. Transient eddy standard deviation of temperature at 975 hPa. Contours are every 1 °C. Correlation coefficient $R = 0.99$. For land only: $R = 0.99$, for ocean only: $R = 0.99$.

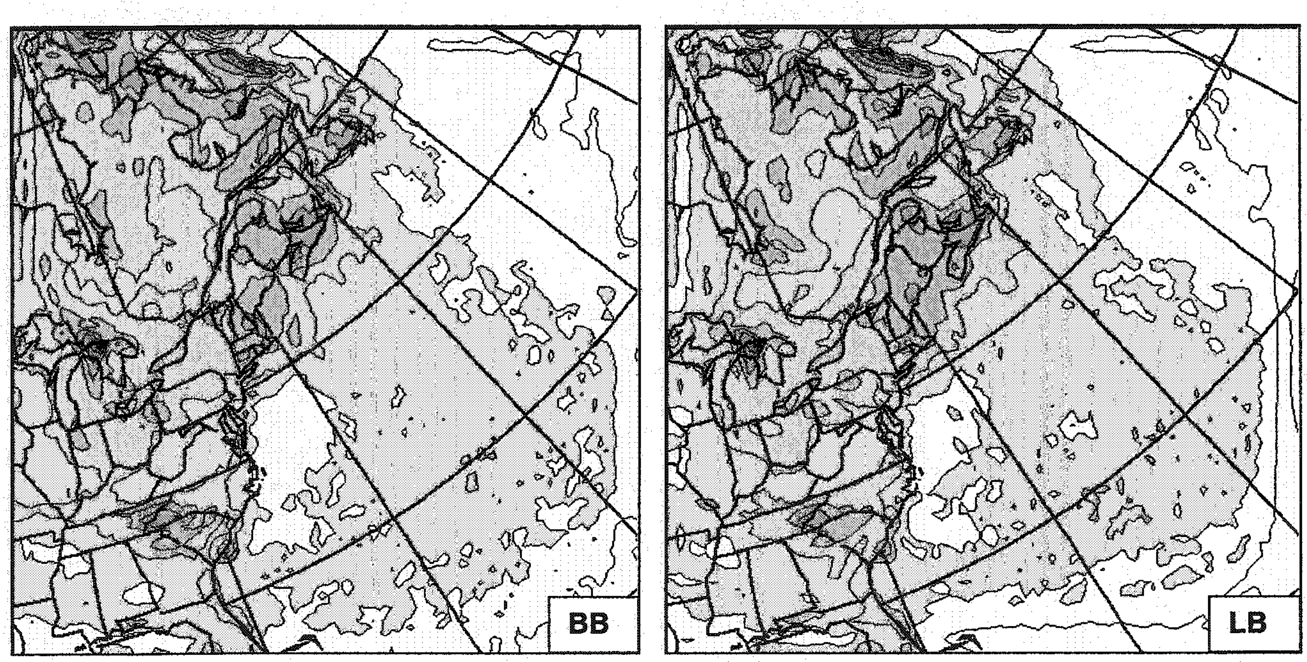

Fig. 12b. Transient eddy standard deviation of the small-scale component of temperature at 975 hPa. Contours are every 0.25 °C. Regions with values larger than 0.5 °C are shaded. Correlation coefficient $R = 0.95$. For land only: $R = 0.91$, for ocean only: $R = 0.89$.

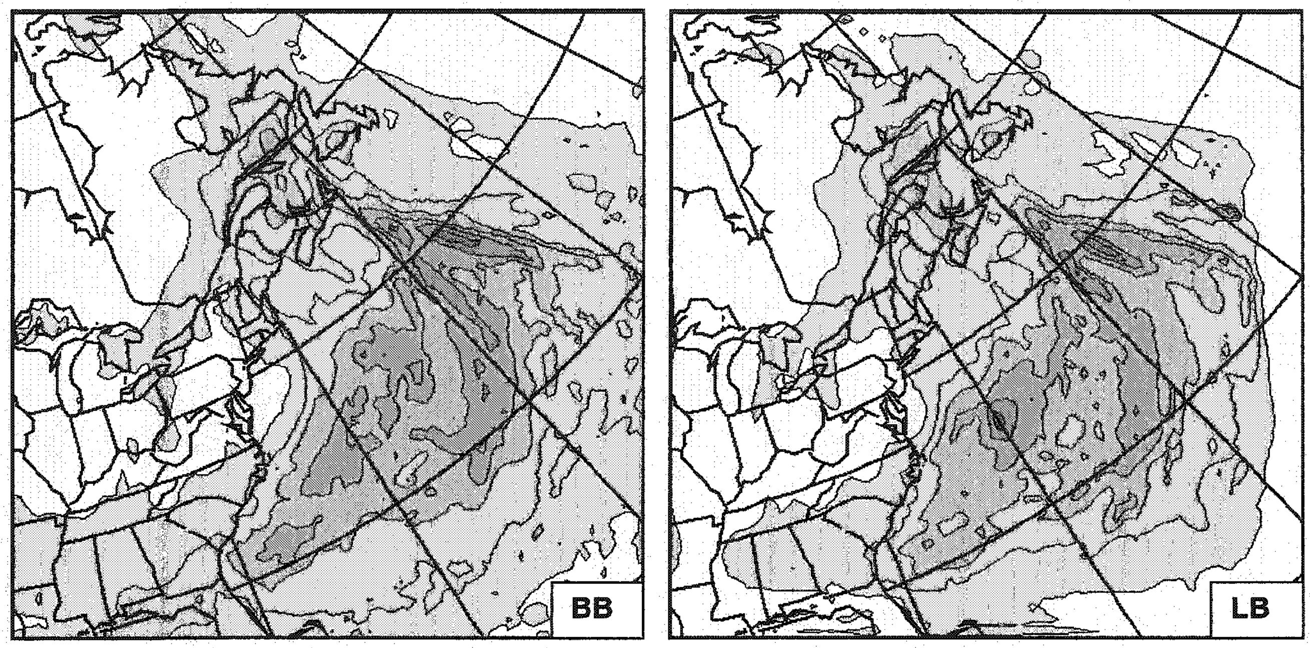

Fig. 13a. Monthly mean precipitation rate. Contours are every 2 mm per day. Regions with values larger than 2 mm per day are shaded. Correlation coefficient $R = 0.93$. For land only: $R = 0.94$, for ocean only: $R = 0.90$.

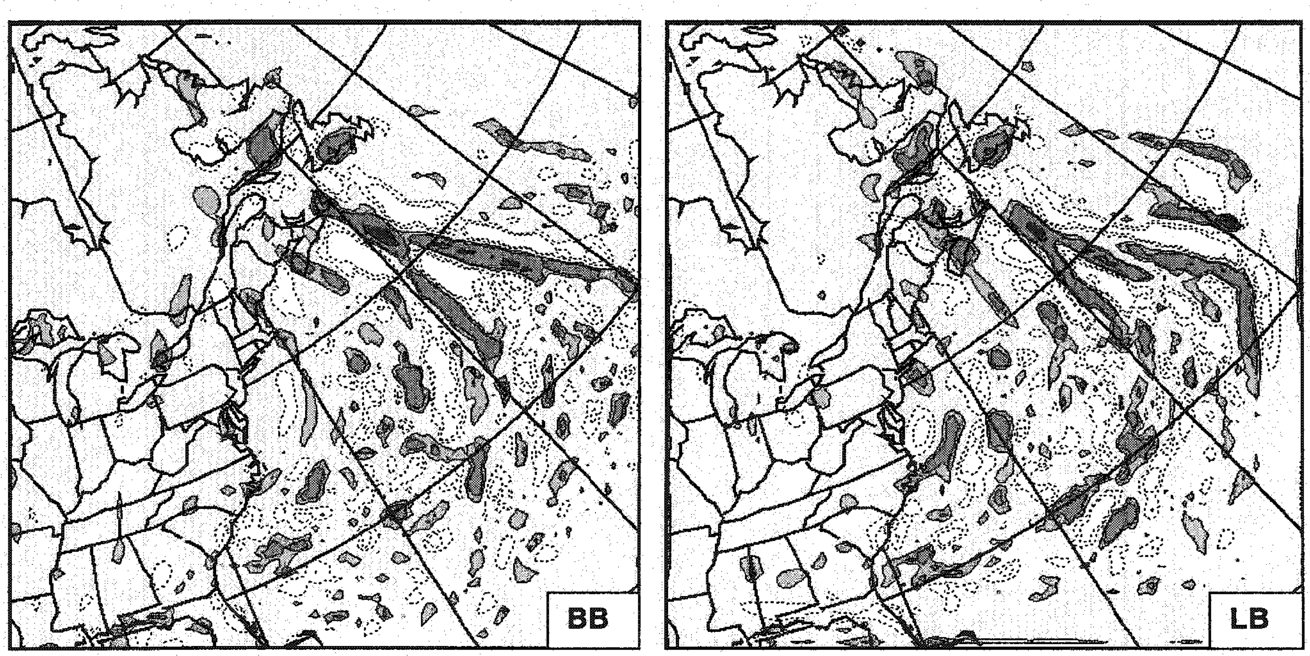

Fig. 13b. Stationary small-scale component of the precipitation rate. Contours are [-5,-3,-1,-0.5,0.5,+1,+3,+5] mm day^{-1}. Regions with values larger than 0.5 mm day^{-1} are shaded. Correlation coefficient $R = 0.44$. For land only: $R = 0.60$, for ocean only: $R = 0.40$.

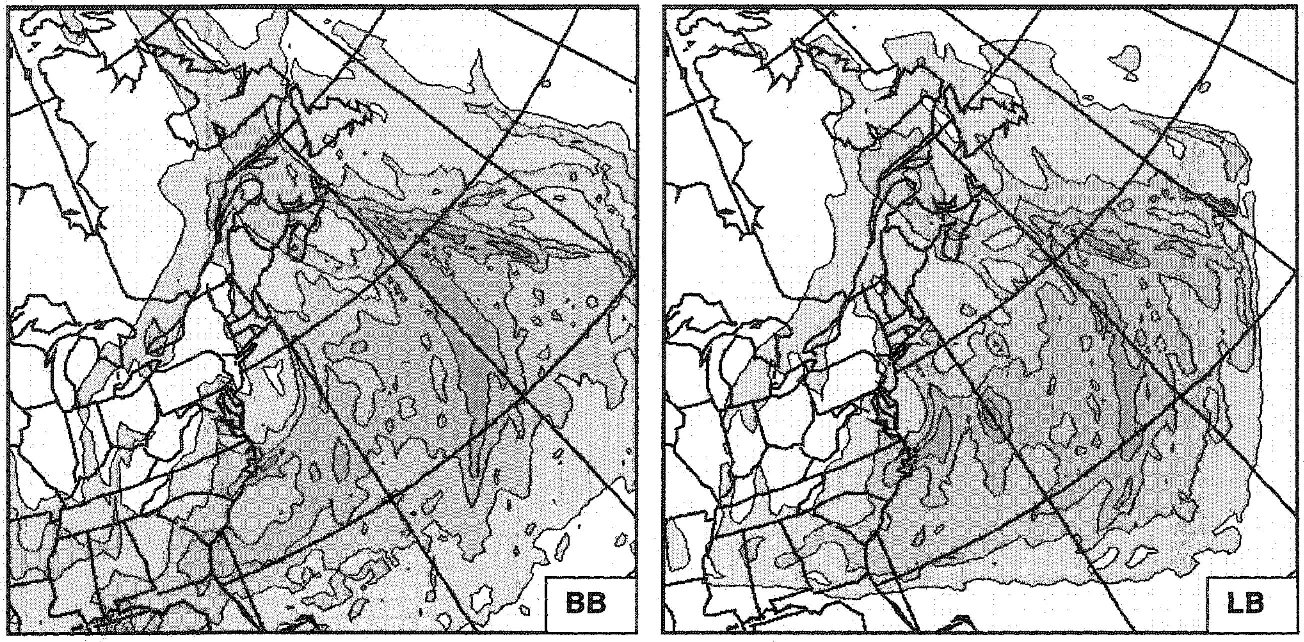

Fig. 14a. Standard deviation of precipitation rate. Contours are every 5 mm day^{-1}. Regions with values larger than 5 mm day^{-1} are shaded. Correlation coefficient $R = 0.88$. For land only: $R = 0.84$, for ocean only: $R = 0.81$.

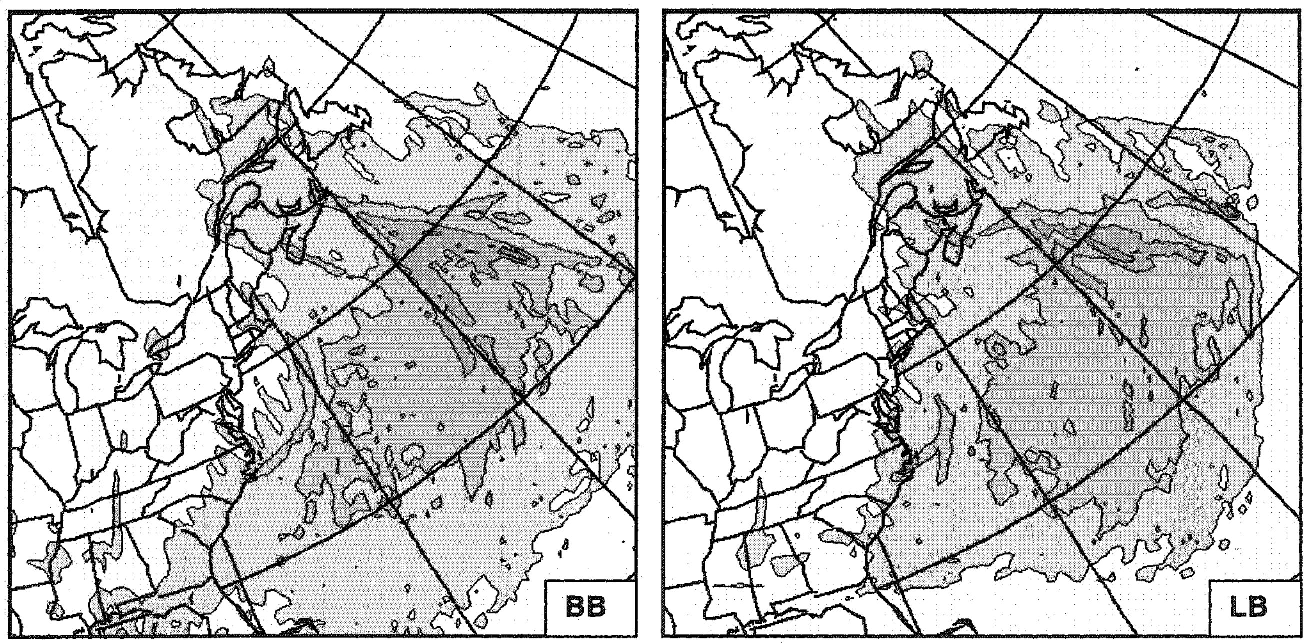

Fig. 14b. Standard deviation of the small-scale component of the precipitation rate. Contours are every 5mm per day. Regions with values larger than 5 mm day^{-1} are shaded. Correlation coefficient $R = 0.90$. For land only: $R = 0.80$, for ocean only: $R = 0.83$.

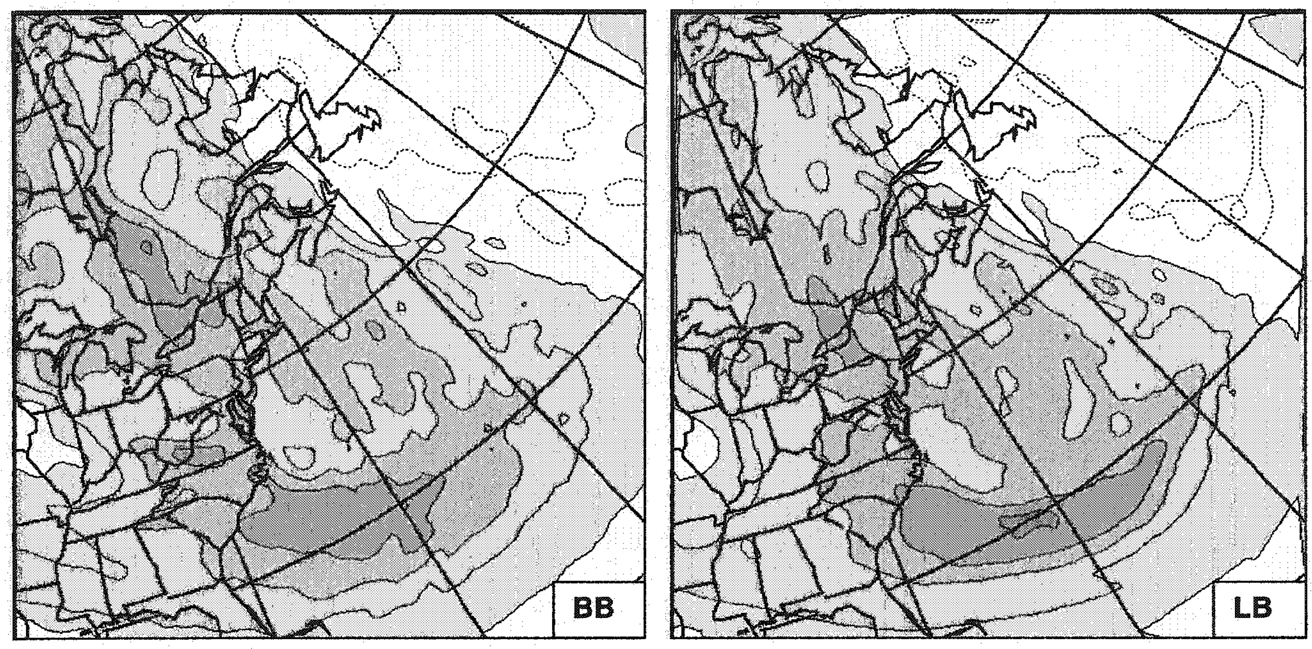

Fig. 15a. Monthly mean relative vorticity at 500 hPa. Contours are every 1 x10-5 s-1. Regions with positive values are shaded. Correlation coefficient R = 0.97. For land only: R = 0.95, for ocean only: R = 0.97.

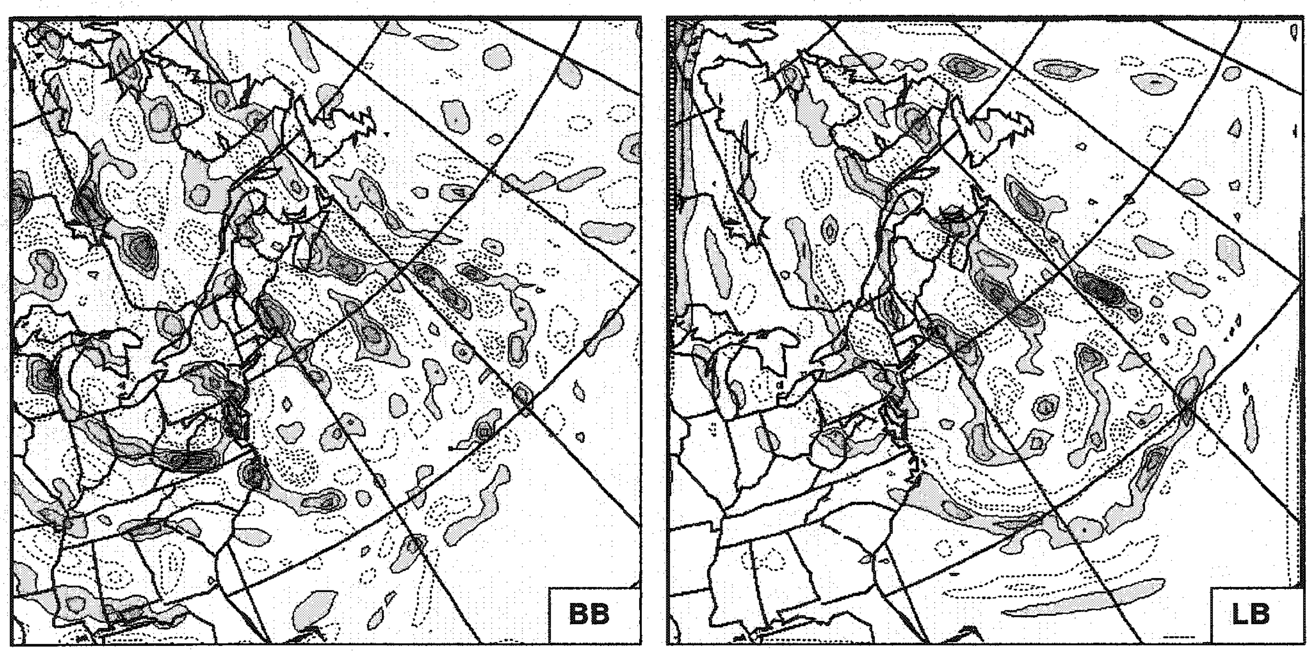

Fig. 15b. Stationary small-scale component of relative vorticity at 500 hPa. Contour intervals are every 0.2×10^{-5} s^{-1}. The zero contour is missing. Regions with values larger than 0.2×10^{-5} s^{-1} are shaded. Correlation coefficient $R = 0.38$. For land only: $R = 0.45$, for ocean only: $R = 0.35$.

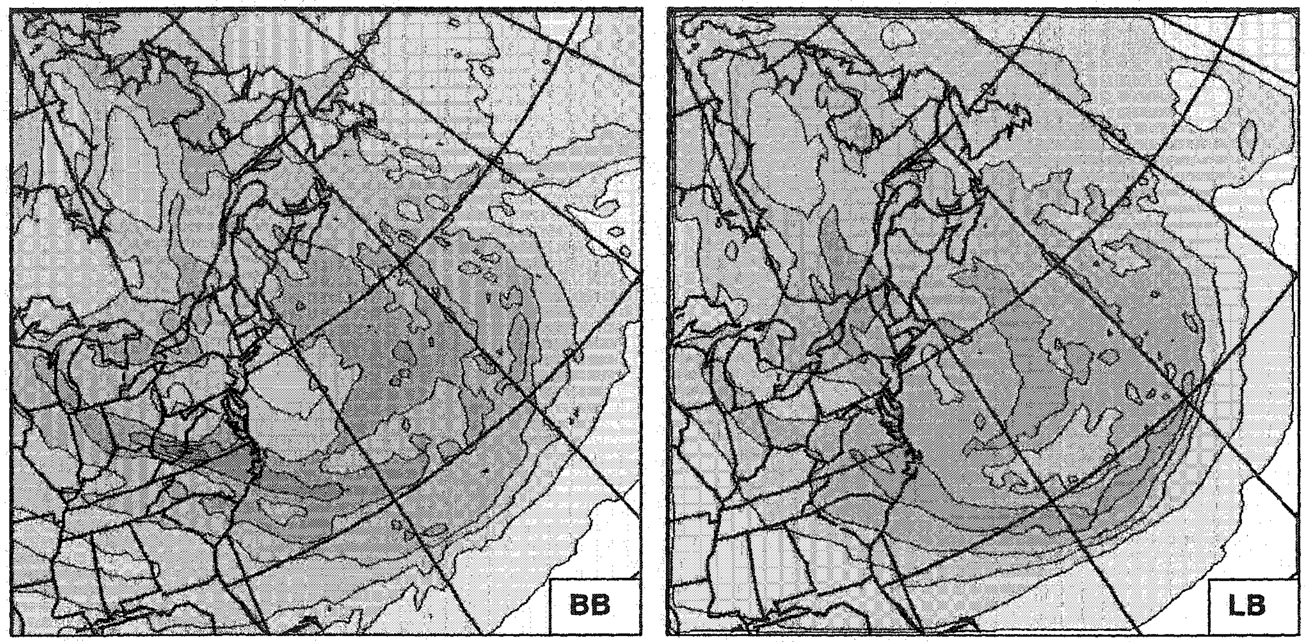

Fig. 16a. Transient eddy standard deviation of the relative vorticity at 500 hPa. Contours are every $1 \times 10^{-5}\ s^{-1}$. Regions with values larger than $2 \times 10^{-5}\ s^{-1}$ are shaded. Correlation coefficient $R = 0.87$. For land only: $R = 0.73$, for ocean only: $R = 0.90$.

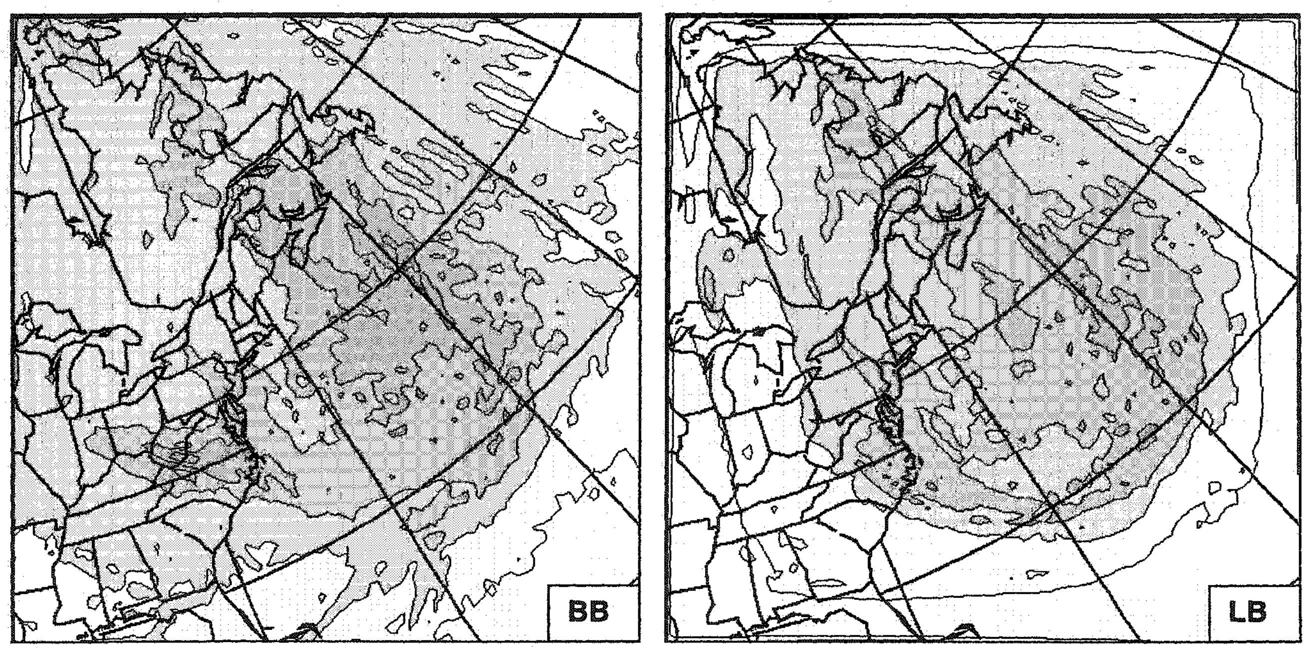

Fig. 16b. Transient eddy standard deviation of the small-scale component relative vorticity at 500 hPa. Contours are every $1 \times 10^{-5}\ s^{-1}$. Regions with values larger than $2 \times 10^{-5}\ s^{-1}$ are shaded. Correlation coefficient $R = 0.82$. For land only: $R = 0.52$, for ocean only: $R = 0.90$.

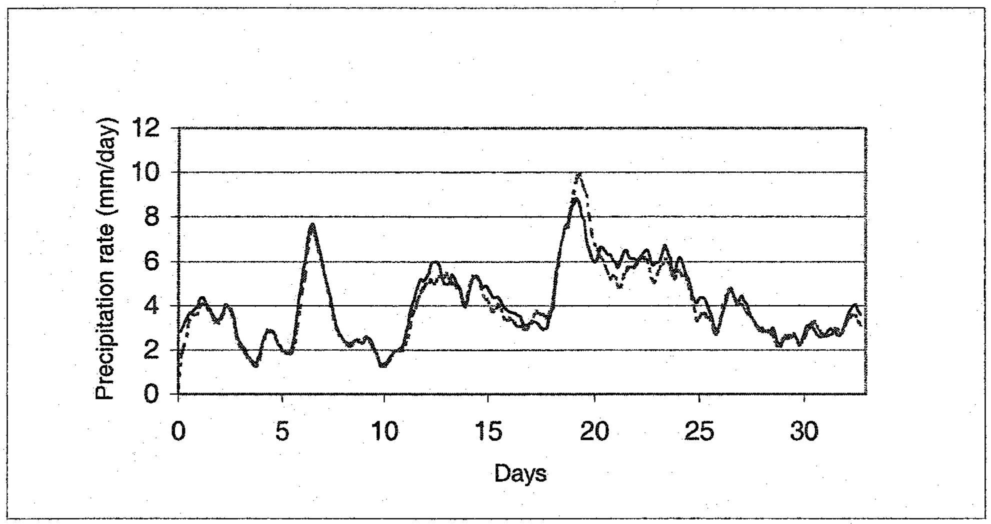

Fig. 17. Time series of spatial-averaged precipitation rates. Solid curve: Big Brother; dash curve: Little Brother.

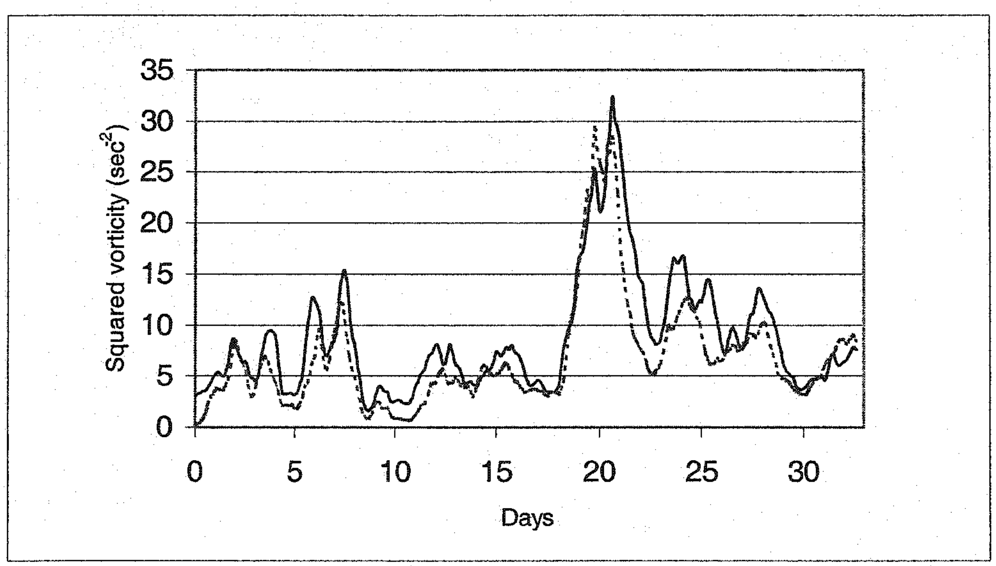

Fig. 18. Time series of spatial-averaged squared relative vorticity at 500 hPa due to small scales. Solid curve: Big Brother; dash curve: Little Brother.

Tables

TABLE 1. Variance ratios Γ_{ss}^{stat} and Γ_{ss}^{trans} for slp.

	Land & Ocean	Land	Ocean
Stationary - small scales	1.01	1.06	0.86
Transient - small scales	0.95	0.99	0.91

TABLE 2. Variance ratios Γ_{ss}^{stat} and Γ_{ss}^{trans} for temperature at 975 hPa.

	Land & Ocean	Land	Ocean
Stationary - small scales	0.99	0.99	0.96
Transient - small scales	1.00	0.99	1.02

TABLE 3. Variance ratios Γ_{ss}^{stat} and Γ_{ss}^{trans} for precipitation rate.

	Land & Ocean	Land	Ocean
Stationary - small scales	1.02	0.96	1.04
Transient - small scales	0.98	0.96	0.99

TABLE 4. Variance ratios Γ_{ss}^{stat} and Γ_{ss}^{trans} for relative vorticity at 500 hPa.

	Land & Ocean	Land	Ocean
Stationary - small scales	0.82	0.55	1.07
Transient - small scales	0.79	0.73	0.83

Comments of the Reviewers

1. Reviewer: Philip B. Duffy, LLNL

Summary:

This paper describes a well-conceived study which assesses the ability of nested regional climate models (RCMs) to simulate fine-scale climate features when driven using coarse-resolution data at the lateral boundaries. This issue is important, and will become even more important as the climate-research community puts more energy into assessing regional impacts of anthropogenic climate change.

The study is designed to isolate problems in the RCM solution due to the nesting procedure from problems due to other causes. The design of the experiments is simple, clever, and, to my knowledge, unique. It seems to have succeeded in isolating problems associated with the nesting procedure.

In contrast to much of the scientific "literature", this paper is very clearly written, and was a pleasure to read. The Introduction gives a fairly thorough review of possible problems associated with nesting RCMs. Although this adds significantly to the length of the paper, I think it is important to include this material, as it makes the paper much more accessible to non-specialists (by which I mean climate researchers who do not work with RCMs). This broad accessibility is one of the paper's strengths.

My bottom-line assessment is that this is an excellent paper, one of the best I have recently read. I am recommending that the paper be accepted after very minor revisions are made.

General comments:

1. I do have one question about the experimental design. In order to produce coarse-resolution information to force the RCM at the lateral boundaries, the results of the Big Brother were filtered using essentially a low-pass filter. An alternative approach would have been to perform spatial averaging of the Big Brother solution. Why was filtering used instead of averaging?

2. In the Conclusions section, more caveats should be added. As the authors themselves point out earlier, their findings apply to only one resolution jump, one domain size, etc. This should be reiterated in the Conclusions section.

Specific Comments:

1. Introduction, first sentence: The reference cited here is old (IPCC, 1990). It would be more persuasive to cite a more recent reference.

2. Introduction, second paragraph: At the end of the 3rd sentence, the word "respectively" should be added, I believe.

3. Introduction, p. 8, last sentence of 1st paragraph: the word "fictitious" is misspelled.

4. Introduction, pp. 8 – 9: In the discussion of sensitivity of RCM results to domain size, there seems to be an implicit assumption that it is bad for RCM results to deviate from those obtained with a coarse-resolution GCM. But it seems to me that it may be expected, and good, for the RCM results (when aggregated to an appropriately coarse resolution) to differ from those of a coarse-resolution GCM.

5. Inroduction, p. 11, 1st full paragraph: "scepticism" should be "skepticis."

6. Experimental Design, p. 12, 1st paragraph:: In the last sentence, "does not resolve" should be "would not resolve."

7. Experimental design, p. 14: In the discussion of vertical resolution, it should be made clear what sort of vertical coordinate the model uses. As it stands, the discussion of interpolating the results to pressure levels and then to "model levels" was opaque to me.

8. Results, p. 16: In the second line, "scrutinise" should be "scrutinize" (assuming CD uses American English spellings).

9. Results, p. 16: In the thrid line from the bottom, "five days prior the..." should be "five days prior to the...".

10. Results, p. 23, end of middle paragraph: "...little stationary small-scale forcings..." should be "...few stationary small-scale forcings."

11. p. 30, end of first paragraph: "different speed" should be "different speeds."

2. **Reviewer: Daniela Jacob, MPI**

I

B

Climate Dynamics - Reviewer's Comments for Author(s)

JUN 04 2001

Author(s): Denis, Laprise, Caya, Côté

Title: Downscaling ability of one-way nested regional climate models: The big-brother experiment

Dr. Daniela Jacob

Signature (only if you wish your identity to be revealed to the author(s))

Comments for the author(s):

Dear authors,

I recommended to accept the paper with minor revision (typos..)
It is a very important and excellent paper, which will have major impact on the climate modelling community. It shows the downscaling ability and quality of RCM using a clear and well defined Big Brother Experiment.
The introduction gives a good motivation for this experiment, listing several important issues for RCMs. Please add a few comments concerning the following points.

p6 b.) Please indicate what might happen, if the ratio is as high as 10 or even higher. What are the drawbacks? Which budgets might be affected?

c.) Is it really possible to separate between spin-up of the soil and of atmospheric features? Does the spin-up of the surface hydrology influence the faster spin-up in the atmospheric features due to incorrect latent heat fluxes or.?

II B

JUN 04 2001

page 7 d)

An update frequency of 12 h will also have an effect on the turbulent kinetic energy of travelling systems. For example the curvature of a front will be distroyed when travelling through the boundary into the domain.

page 10 i.)

Climate drift must be studied in longer runs taking annual and inter-annual variability into account. Please notice that only the first multi-decadal RCM runs are available and that the issue of drift will be studied using coupled and uncoupled RCMs.

page 14.)

It is not always the ~~same~~ case that pressure level data from GCMs are used. More direct input from model level to model level is used. What is the effect of the interpolation procedure?

Chapter IV

Sensitivity of a Regional Climate Model to the Spatial Resolution and Temporal Updating Frequency of the Lateral Boundary Conditions

Using the Big-Brother Experiment framework developed in the previous Chapter, the sensitivity of an RCM to the *spatial* resolution and t*emporal* update frequency of the LBC is investigated. These are two of the most important issues concerning use of the one-way nesting strategy for dynamical climate downscaling purposes. Because the text of the second and third paper is meant to be self-contained, this leads to some unavoidable overlap between them.

Sensitivity of a Regional Climate Model to the *Spatial* Resolution and *Temporal* Updating Frequency of the Lateral Boundary Conditions

Bertrand Denis[*+#],
René Laprise[*] and
Daniel Caya[*]

[*] *Département des sciences de la Terre et de l'Atmosphère, Université du Québec à Montréal, Montréal, Québec, Canada*

[+] *Department of Atmospheric and Oceanic Sciences, McGill University, Montréal, Québec, Canada*

 # Recherche en Prévision Numérique, Meteorological Service of Canada, Dorval, Québec, Canada

Submitted to *Climate Dynamics*

31 August 2001

Corresponding author address:

Bertrand Denis
Recherche en Prévision Numérique
2121 Route Transcanadienne
Dorval, Québec
Canada
H9P 1J3

Email Bertrand.Denis@ec.gc.ca

Abstract

The sensitivity of a one-way nested regional climate model (RCM) to the spatial and temporal levels of information provided at its lateral boundaries is studied. To unambiguously address these two issues, a perfect-prognosis approach called the Big-Brother Experiment (BBE) is employed. It consists in first establishing a reference climate simulation (called the Big Brother) over a large domain and then using the simulated data for nesting another RCM (called Little Brother) integrated over a smaller domain. The effect of degrading the resolution of lateral boundary conditions (LBC), spatially and temporally, is investigated by comparing the big- and little-brother climate statistics for the total and fine-scale components of the fields, as well as for their stationary and transient components.

Within the BBE framework using a 45-km grid-point RCM, it is found that the one-way nesting approach gives satisfactory results for most fields studied when spatial resolution jumps up to 12 are imposed between the nesting data and the Little Brother. For the LBC update interval, 12 hours appears to be the upper limit, while little difference is found between update intervals of 3 and 6 hours.

1. Introduction

The one-way nesting strategy has been so far the most popular approach employed by dynamical regional climate models (RCMs) for downscaling large-scale atmospheric information to regional scales. The fine-scale features that develop in RCMs are the results of atmospheric internal dynamical interactions and surface forcings supported by the RCM's high-resolution gridmesh, while the RCM's large-scale destiny remains controlled by the large-scale atmospheric circulation imposed at its lateral boundaries. The RCM's fine-scale features are the added-values over conventional low-resolution Global Climate Models (GCMs), which are computationally prohibitive to run for long climate simulations with the same high resolution since they have to be integrated with a domain covering the entire Earth.

Even though the one-way nesting technique has become widely used for regional climate modelling and proved to be a workable approach for climate downscaling (Giorgi and Mearns, 1999), skepticism has been expressed concerning the ability of such a technique to adequately simulate regional climates (CAS/JSC WGNE, (1999, 2000)). There are a number of issues that are related to the one-way nesting, which, as the name implies, does not allow feedback between the RCM and its driving data (simulated or objective analyses). Most of these has been reviewed by Denis et al. (2001b) who designed an experimental framework, called the Big-Brother Experiment (BBE), to test the downscaling ability of a one-way nested RCM. From the list of issues raised, the impact of the resolution jump between the driving data and the RCM, and the temporal updating frequency of the lateral boundary conditions (LBC), are two important topics that have not yet been rigorously studied. In this paper, we propose to use the BBE to shed some light on these two issues.

The first objective of this paper is to answer the question: What is the maximum spatial resolution jump between the driving data and the driven model that can be used? Figure 1 shows an example of a resolution jump and the implied increased level of details generated by a one-way nested RCM. The case displayed is a winter snapshot of the low-level moisture field produced by the Canadian RCM (CRCM) (Caya and Laprise, 1999) nested in the Canadian GCM (McFarlane et al., 1992). In this case, the driving model (GCM) was a spectral T32 (~ 600 km grid spacing) and the nested RCM had a resolution of 45 km. Regional climate simulations using this resolution jump with the CRCM are reported in Laprise et al. (1998). It can be seen in Fig. 1 that the RCM is able to generate fine-scale features on the large-scale flow imposed at its lateral boundaries. Are these features meaningful and reliable? Or are they just noise and do not make sense from a climate point of view? In other words, are the climate statistics of these features, such as time-averages, transients, extremes and all climate related budgets, realistic? This is the question that Denis et al. (2001b) attempted to answer but with only one resolution jump. In this paper, the first objective is to asses the *maximum* resolution jump that still produces meaningful results. The second objective is to get an idea about the upper limit of the LBC temporal updating interval that can be employed without deteriorating unacceptably the simulated RCM climate.

2. Experimental design

a. The Big-Brother Experiment

Because the validation of RCMs is severely limited by the lack of high-resolution detailed climatologies, a "perfect-prognosis" approach nicked-named the Big-Brother Experiment (BBE) is adopted in this paper, following the methodology described in detail by Denis et al. (2001b). To summarize, the BBE consists in first establishing a reference climate by performing a large-domain high-resolution RCM simulation: this simulation is called the Big Brother. This reference simulation is then degraded by filtering short scales that are unresolved in today's global objective analyses (OA) and/or GCMs when integrated for climate projections. This filtered reference is then used to drive the same nested RCM (called the Little Brother), integrated at the same high-resolution as the Big Brother, but over a smaller domain that is embedded in the big-brother domain. The climate statistics of the Little Brother are then compared with those of the Big Brother over the little-brother domain. Differences can thus be attributed unambiguously to errors associated with the nesting and downscaling technique, and not to model errors nor to observation limitations. The flowchart in Fig. 2 illustrates the essence of the BBE framework. Although not explicitly shown in Fig. 2, the Big Brother has to be supplied with lateral boundary conditions (LBC). This was done with the use of 12-hour archived global analyses. Fig. 3 shows the computational domains of the big and the Little Brother that has been used in this paper. The domains are centered on the North-American East Coast. The grid-point spacing is 45 km. The big- and the little-brother domain include 196 by 196 and 100 by100 gridpoints, respectively. The little-brother nesting zone is shown as a dashed line along its lateral boundary. In this paper, the simulations that we shall study are for winter months (four February months).

b. Brief description of the CRCM

The RCM employed to do the big-brother experiments is the Canadian Regional Climate Model (CRCM) (Caya and Laprise, 1999). It is a limited-area grid-point non-hydrostatic model that uses a three-time-level semi-Lagrangian semi-implicit numerical scheme. The timestep used in our experiments was 15 minutes and the grid-point spacing 45 km. The one-way nesting technique was developed by Robert and Yakimiw (1986) and Yakimiw and Robert (1990) and is inspired from Davies (1976). A complete description of the dynamical formulation of the CRCM, including the nesting implementation, can be found in Bergeron et al. (1994) and in Laprise et al. (1997). The physical parameterizations are similar to what can be found in Caya and Laprise (1999) except for the moist convection scheme, which now follows the Kain and Fritsch (1990) formulation. The time evolution of the sea-surface temperature (SST) was imposed by linearly interpolating monthly mean climatological data; because of this, there were no fine-scale structures in the SST field.

c. Definition of the spatial resolution jump

In Denis et al. (2001b), the downscaling ability of the one-way nesting was tested for only one resolution jump. The big-brother reference run was degraded such that all disturbances having *wavelengths* smaller than 500 km were removed while wavelengths greater than 1000 km were left unaffected by the filtering. The grid-point spacing of the

RCM being 45 km, the resolution jump defined by the ratio $J = \frac{\text{RCM spatial res.}}{\text{LBC spatial res.}}$ was about 6, i.e. ~ (wavelength of 500 km)/ (wavelength of 2x45 km). The results for that particular ratio were generally very good.

In the present paper, the climate sensitivity to the resolution jump is examined by varying the resolution level of information provided by the LBC. The spatial filtering employed to degrade the resolution has been performed in the spectral space using a 2D discrete cosine transform (DCT) (Denis et al., 2001a). This spectral filtering technique is suitable for non-periodic data and gives full control over the choice of the wavelengths to be removed. Four different resolution jumps have been generated by the filtering of the big-brother dataset. Figure 4 shows the response curves defining the 4 resolutions. The corresponding resolution jumps (J6, J12, J24 and J48) for the 45-km RCM and the equivalent spectral triangular spherical harmonic truncations (T60, T30, T15 and T7) are also shown. As an illustration of the filtering effect, Fig. 5 shows the results of the four filtering levels on an instantaneous mean-sea-level pressure field and a relative vorticity field (1000 hPa). The panel labelled J1 displays the unfiltered fields. For all spatial resolution experiments, the temporal updating interval was 3 hours. Linear time-interpolation was performed between these times to accommodate the nesting which is applied every timestep.

d. Definition of the temporal updating frequency

In the second part of this study, four updating frequencies will be compared: U8, U4, U2 and U1, corresponding to 8, 4, 2 and 1 update per day, i.e. update intervals of 3, 6, 12 and 24 hours, respectively. It is important to stress again that linear interpolation is used to fill in between these update instants. The ensemble of experiments that have been performed by varying either the spatial or temporal LBC resolutions, or both, is shown in Table 1.

3. Results

Before looking at the little-brother's ability to reproduce the big-brother climate when the resolution jump and updating frequency are varied, we would like first to give an idea of the inter-annual variability of the four simulated months. To this end, and to improve the significance of the climate statistics as well as the robustness of the results obtained by Denis et al. (2001b), simulations were carried out for four different February months: February 1990, 1991, 1993 and 1994. Figures 6 and 7 show the big-brother monthly means of sea-level pressure and precipitation rate, respectively. These fields, as well as all the rest of the displayed fields, are shown on the little-brother domain. It can be seen from Figs. 6 and 7 that the inter-annual variability is fairly high, but some characteristics proper to the North-American East Coast winter climate are noticeable. For example, the pressure trough offshore accompanied by a more intense precipitation area over the ocean is very visible. This is due to the mean circulation producing dry cold air advection over the Gulf Stream which fuels storm developments. Furthermore, the stationary Great Lakes effect can be clearly seen in the sea-level pressure field of years 1990 and 1993 and also in the precipitation rate field for years 1990, 1991 and 1993.

a. Sensitivity to the spatial resolution of the LBC

We now turn our attention to the ability of the Little Brother to reproduce its Big Brother, as a function of the resolution jumps as defined in Section 2c. Results are presented first for the time-average (stationary) and time-standard-deviation (transient) parts of sea-level pressure (*slp*) and precipitation rate (*pcp*) fields. In order to facilitate the examination of the little-brother downscaling ability to reproduce the fine-scale features, these features were extracted by the use of a spatial spectral filter (as in Denis et al. (2001b)) and examined separately. It must be noted that the fine scales considered here for diagnostic purposes, are those that can survive a J6 filtering. These fine scales had to be regenerated inside the domain by the little-brother simulations (J6, J12, J24, J48); none of these simulations did get information of scales smaller than the J6 level from the lateral boundaries or the initial conditions. For each displayed field, the correlation coefficients ***(R)*** between each Little Brother and the reference Big Brother are given, as well as the ratios of the spatial variance (Γ). It must be noted that the nesting zone is excluded from all diagnostic calculations or skill scores such as the correlation coefficients and ratios of variance, but it *is* part of all field displayed (see Fig. 3 for the nesting zone delimitation). Finally, diagrams summarising the results for the *slp*, *pcp*, and also for 975-hPa temperature and 500-hPa relative vorticity are presented at the end of the Section.

i. Sea level pressure fields

Figures 8 and 9 show the total and the small-scale components of the sea-level-pressure (slp) fields averaged over four February months. These fields can be seen as the stationary parts of the mass field (Fig. 9) even though there exists a large inter-annual variability for the total components as seen from Fig. 6. The first striking evidence from Fig. 8 is that, as far as the large scale is concerned, the Little Brother is capable of reproducing its Big Brother at least up to a resolution jump of 24 (T15). This may not be surprising since that field is largely dominated by large-scale features which in turn are highly controlled by the large-scale driving LBC provided by the Big Brother. Figure 9 shows that, even though the correlation coefficient for the small-scale components drops faster than for the total component, the fine-scale features, such as those induced by the Great Lakes and the mountains, exhibit a strong robustness up to J24.

The ability to reproduce the transient variability is certainly as important as the ability to reproduce the stationary time-averaged climate. Figure 10 shows the effect of the resolution jump on the transient-eddy standard deviation of the slp. We can see that the Little Brother is capable of maintaining the same level of transient activity as its Big Brother, and that up to J12. After this jump of resolution the activity is significantly smaller, as shown by a variance ratio Γ of 70% and 12% for J24 and J48, respectively. Interestingly, when only the fine scales are considered in the calculation of the transient activity (Fig. 11), the Little Brother yields reasonable results up to J24.

ii. Precipitation rate fields.

Precipitation is probably one of the most important climate quantities. It is also an end-of-the-line product of the climate system since it results from many processes and interactions between the climate components. In an RCM, precipitation is generated by parameterized physical processes as well as numerically resolved atmospheric transports. It is also worth noting that precipitation is not one of the variables that are supplied at the lateral boundaries as are, for example, the pressure, temperature, moisture and wind fields. It is critical field to our study, therefore, to look at this field.

Time averages of precipitation rates over the four February months are presented in Fig. 12. It can be seen that the Little Brother holds well up to J12. After that, the amount of precipitation decreases substantially, as can be seen on the J24 panel where the area receiving at least 2 mm per day has shrunk significantly. It can be noted that for all little-brother cases, precipitation is lower along the boundaries; the main reason for this is that the vertical velocity is set to zero at the boundaries. The stationary small-scale components are presented in Fig. 13. It can be seen that the time-averaging process has left negligible fine-scale features common to all simulations, especially over the ocean. But there are some signs of regional persistent precipitation patterns over the Great Lakes and over the sea-ice edge of the Labrador coast that are visible up to J24. In fact, when computed from land gridpoints alone for J24, the correlation coefficients increase from $\boldsymbol{R}$=25% to $\boldsymbol{R}$=57% , and the variance ratio increases from $\boldsymbol{\Gamma}$=81% to $\boldsymbol{\Gamma}$=92% .

The ability of the Little Brother to reproduce time variability of precipitation is shown in Figs. 14 and 15 for the total and small-scale components, respectively. It can be noted, firstly, that both quantities have similar patterns and similar values (though somewhat smaller for the small-scale components). This is due to the fact that the temporal variance of the precipitation fields is dominated by the effect of transient fine-scale features such as fronts. Secondly, the maximum acceptable resolution jump appears to be again J12.

iii. Summary diagrams

A convenient graphical method to summarize comparisons of model results has been proposed by Taylor (2001). The now so-called Taylor diagram is a way of plotting on a 2-D graph, using the law of cosines (see Appendix), three statistics that indicate how closely two datasets match each other. These statistics make it easy to determine how much of the overall mean square difference (or RMS difference) is attributable to a difference in variance and how much is due to a poor pattern correlation. A diagram of this type is shown in Figs. 16-17. For a given point position on the diagram, the mean square difference is proportional to the radial distance from the origin of the abscissa, the ratio of variance (Little Brother / Big Brother) is proportional to the radial distance from the lower-right corner, and the correlation is the azimuthal position which gives the correlation coefficient between the Little and Big Brother. For normalization purposes, the mean square difference is relative to the Big Brother`s variance and thus expressed as a percentage. The goal for the Little Brother is to fall as close as possible to the abscissa origin with a ratio of variance near 100%. The space and time decomposition that was employed (see the Appendix) permits an evaluation of the little-brother performance in terms of the stationary (Fig. 16) and transient components (Fig. 17), respectively.

The expression for the stationary part is given by

$$\frac{d^{*2}_{\overline{LB}\,\overline{BB}}}{\sigma^{*2}_{\overline{BB}}} = 1 + \frac{\sigma^{*2}_{\overline{LB}}}{\sigma^{*2}_{\overline{BB}}} - 2\frac{\sigma^{*}_{\overline{LB}}}{\sigma^{*}_{\overline{BB}}} R^{*}_{\overline{LB}\,\overline{BB}} \tag{1}$$

where $\frac{d^{*2}_{\overline{LB}\,\overline{BB}}}{\sigma^{*2}_{\overline{BB}}}$ is the relative mean square difference, $\frac{\sigma^{*2}_{\overline{LB}}}{\sigma^{*2}_{\overline{BB}}}$ is the ratio of spatial variances, and $R^{*}_{\overline{LB}\,\overline{BB}}$ is the correlation coefficient between the little-brother and the big-brother stationary part. The ratio of variance and the correlation coefficient for the stationary part in Eq. (1) are the same as those of Figs. 8-9 and Figs. 12-13.

The Taylor diagrams for the stationary component of the sea-level pressure, precipitation rate, 975-hPa temperature and 500-hPa relative vorticity are shown in Fig. 16. In each diagram, the results for the total fields and the fine-scale fields are displayed for the 4 resolution jumps as well as the J1 case (same resolution, i.e. no jump). It can be seen in all diagram that the total fields are very robust to the increase of the resolution jump, at least up to J12 as shown by mean square differences smaller than 10% in all cases. This holds (although less strongly) also for the small-scale components of slp and temperature, but not for the precipitation and vorticity fields, which show a clear tendency to decorrelate and diminish variances with increasing resolution jumps.

The expression for the transient component is given by

$$\frac{\left\langle \overline{d'^2_{LB\,BB}} \right\rangle}{\left\langle \sigma'^2_{BB} \right\rangle} = 1 + \frac{\left\langle \sigma'^2_{LB} \right\rangle}{\left\langle \sigma'^2_{BB} \right\rangle} - 2\frac{\left\langle \sigma'^2_{LB} \right\rangle^{1/2}}{\left\langle \sigma'^2_{BB} \right\rangle^{1/2}} R'^{e}_{LB\,BB} \tag{2}$$

where $\frac{\left\langle \overline{d'^2_{LB\,BB}} \right\rangle}{\left\langle \sigma'^2_{BB} \right\rangle}$ is the relative mean square difference of the transient part, $\frac{\left\langle \sigma'^2_{LB} \right\rangle}{\left\langle \sigma'^2_{BB} \right\rangle}$ is the ratio of the spatially averaged temporal variances, and $R'^{e}_{LB\,BB}$ is an effective temporal correlation coefficient. It must be noted that the ratio of variance and the correlation coefficient for the transient part as expressed in Eq. (2) are different than those shown in Figs. 10-11 and 14-15 because $R'^{e}_{LB\,BB}$ represents a correlation of time series averaged over the domain and not a correlation between 2-D images of transient standard deviations.

The Taylor diagrams for the transient components are displayed in Fig. 17. The slp and temperature fields are again the most reproducible fields by the Little Brother. The transient fine scales cause much more difficulty as is apparent from by the poor correlation on each diagram. This is because our definition of the correlation coefficient for the transient component is deterministic, i.e. it takes into account the temporal correlation of events; that is very demanding for a climate model that is integrated for a longer period than the deterministic forecast period (a few days). Boer and Lambert (2001) have proposed a modified version of the Taylor diagram which is more adapted for global climate simulations since the temporal correlation is left out (assumed to be one). Since a nested RCM is forced at the lateral boundaries, some temporal correlation is expected to occur at least for nested fields showing large-scale variances. On the other hand, the fine scales are not nested (for J6 to J48) and do not have to be time-correlated to yield a good climate. But their transient-eddy fields (e.g. Figs 10-11 and Figs 14-15) should correlate and have the same level of temporal variances. In other words, the poor correlation of the transient fine scales is not critical, but the decrease of variances as seen in Fig. 17 is. In this regard, the Little Brother does well up to J12 for all fields, except for the vorticity field.

b. Sensitivity to the temporal updating frequency

For this part of the study, the time interval of the nesting LBC data is varied, while no spatial filtering of the LBC is applied (J1 case). Four updating frequencies will be compared: U8, U4, U2 and U1, corresponding to 8, 4, 2 and 1 update per day, i.e. every 3, 6, 12 and 24 hours, respectively. It should be noted that experiment U8 corresponds exactly to the experiment J1 presented earlier in Section 3a.

As in the previous Section, Taylor diagrams are used to synthezise the results. Figures 18-19 summarize the effect of varying the updating frequency for the stationary and transient components, respectively. As can be seen in Fig. 18, the stationary component of the total fields that are strongly dominated by their large-scale variance (e.g. sea-level pressure and temperature) are not very sensitive. This may not be surprising since their large-scale components are slowly varying, therefore they do not require a very high temporal resolution of the LBC in order to be nested adequately. On the other hand, fields more dominated by fine-scale features, such as the precipitation and the vorticity fields, are more sensitive. This is especially true for fine-scale components as shown by the weak correlation, but is is not be of much concern because the stationary components of these fields are weak (see for instance Fig. 13), and are not expected to correlate over regions lacking fine-scale surface forcings. Figure 18 also reveals that the mean square difference of the precipitation and vorticity have converged near 1% when the updating frequency is increased to 8 times per day. Therefore, an errorless little-brother simulation does not seem reachable even with higher update frequencies.

The impact of the update frequency on the transients is shown in Fig. 19. The precipitation and vorticity fields are more difficult to reproduce after U4 (6 hours) and certainly after U2 (12 hours), as apparent from the weaker temporal variance. This weakness is less pronounced for the sea-level pressure and is completely absent for temperature. It is interesting to note that for all fields in Figs. 18-19, the update intervals of 3 and 6 hours yield similar results, as illustrated by the closeness of the circle and triangle symbols.

A last set of experiments has been performed in order to reflect more closely the spatial and temporal resolution of the LBC used in the current CRCM mode of operation which consists in driving an RCM at every 6 hours with data provided by a spectral T32 GCM. For that purpose, a single resolution jump J12 (T30) has been employed while the update frequency was varied. Figures 20-21 show the results. It can be seen that the combination of resolution J12-U4, which is similar to what is currently used by the CRCM, gives satisfying results except for relative vorticity, for which the variance ratios of the transient components are significantly low. But it is clear, from the systematic closeness of the circles and triangles, that no gain can be obtained by diminishing the update interval from 6 to 3 hours. This simply reflects, in our BBE context, that driving data having a resolution equivalent to T30 contains only features that are large enough and travel slowly enough to be resolved by a 6 hour interval. On the other hand, reducing the resolution jump by using T60 driving data may likely requires shorter nesting intervals.

4. Discussion

The main hypothesis behind the use of a one-way nested RCM is that it can produce high-resolution climate information from low-resolution LBC, and can achieve this in a reliable and computationally efficient manner. The bigger the spatial resolution jump is, the more efficient this approach is; but this efficiency is at a cost of reliability. The same can be said for the updating frequency, but in this case a lower updating frequency means a reduced usage of storage space and data motion; this is usually a less stringent constraint than computation efficiency. In view of these considerations, let us review the results of the simulations performed in this research in order to define the upper limits of the spatial resolution jumps and update intervals for reliably running a one-way nested RCM.

The results concerning the impact of the spatial resolution jump at the lateral boundaries lead us to believe that jumps as high as 12 can be handled correctly by the nesting mechanism for a 45-km grid-point RCM, at least in a context of climate simulation where statistics such as the time mean and time variability are of primary importance. It must be noted that such a large resolution jump might be too much for deterministic weather forecasts, in particular when the fine-scale features are the centres of interest (Laprise et al., 2000; de Elía et al., 2001).

Concerning the maximum acceptable update time interval that can yield a reasonable climate, experiments showed that a 12-hour interval is workable for a 45-km grid-point model but significant improvements are obtained by using a 6-hour interval. Little improvement was gained by going from 6 to 3 hours at this 45-km resolution. It is interesting to note that, during the infancy of the RCM science, time intervals of 12 hours were the rule. This was probably because the computer storage necessary for archiving global climate simulations serving as driving data was too expensive, or because objective analyses were only available at 12-hour interval. Nowadays, intervals of 6 hours are currently used. It can be argued that update intervals longer than 6 or 12 hours are too large to correctly capture synoptic systems that enter the domain and can underestimate fluxes across the lateral boundary (Majewski, 1997). On the other hand, although such systems might not be quite resolved temporally at the lateral boundaries, they can be regenerated to a certain extent farther inside the domain (if it is large enough) by the large-scale dynamics which interact with the synoptic scales. A similar argument can be used to explain the good results (up to J12) obtained in the first part when the LBC spatial resolution was degraded. But it seems that the larger the resolution jumps or the update intervals are, the longer the fetch inside the nested domain should be to give enough room for the generation of transient fine-scale features. Unfortunately, this reduces the area of usefulness of the RCM domain, and so also its computational efficiency.

Using Taylor diagrams to visualize the results, it has been found that the transient components are more sensitive to the lack of resolution of the LBC (both temporal and spatial) than the stationary components since, as mentioned previously, fine-scales features not supplied at the inflow lateral boundaries must be regenerated inside the domain. Any deficiency with respect to this point should reflected in the transient activity, especially for the smallest scales. On the other hand, stationary fine-scale features are largely caused by stationary forcings such as lakes and mountains, and for this reason show high robustness to the LBC resolution, as long as the large circulation that interacts with these forcings is well simulated overall. This can be seen, for instance, in Figs. 22-23 which show the total and fine-scale components of the stationary 850-hPa wind fields, respectively. As long as the mean flow impedes the mountains with the correct speed and angle, or brings cold air masses over the warm open water areas, the Little Brothers are capable of reproducing their big-brother stationary fine scales.

The results indicate that the spatial and the temporal resolutions of the LBC impact jointly on the simulated climate. To further investigate this point, the most sensitive variable displayed on the Taylor diagrams, the variance ratio of the transient component of the total relative vorticity field, is used. Figure 24 displays the variance ratio as a function of resolution jump and update interval. It can be seen that the isolines of variance ratio are concentric circles or ellipses, with quasi-horizontal lines at small update intervals and quasi-vertical lines at small resolution jumps. This means that the sensitivity to temporal resolution of the LBC is higher at small resolution jumps and decreases with larger resolution jumps because, in the latter case, high-frequency information is implicitly already absent from the low-resolution LBC. Similarly, the sensitivity to the resolution is high at high-frequency updates and decreases at lower frequencies. From Fig. 24, a characteristic "phase speed" can be computed by taking the ratio of the spatial wavelength to the temporal wavelength implied by the jumps and update intervals, respectively. The phase speed turns out to be 30-45 km/h, which is characteristic of the travelling weather systems in mid-latitudes during winter (Laprise and Zwack, 1992). This means that the decrease of the transient variance found in the Taylor diagrams is probably due to the deficiency of adequately resolving weather systems that enter the domain and/or failling to fully regenerating them once inside.

Our finding, which shows that a spatial resolution jump of 12 (corresponding to T30 in our experiments) and an update frequency of 4 times per day (every 6 hours) is acceptable for a 45-km grid-point RCM, must be seen as an upper limit since our BBE is a perfect prognosis approach, i.e. the reference truth is a model-generated virtual reality. The low-resolution data generated for the nesting of the Little Brother were, in a sense, perfect since the full model resolution participated in its generation. This would not be the case for a GCM run at very low resolution such as T7. In effect, a T7 GCM does not produce an acceptable climate even for the large-scale atmospheric circulation since important smaller scale interactions are absent; they are required for the GCM to yield a good large-scale climate. This has been demonstrated by Boer and Denis (1997) who showed that the large-scale solution of a GCM does not converge below T32 resolution. Therefore nesting an RCM with a low-resolution GCM might yield worse results than those seen in this study. Furthermore, in real applications, nested RCMs often do not share the same dynamical numerics and/or physical parameterization with the driving model (or analyses). Even when this is, or nearly is the case, the fact that the driving model and the RCM are not run at the same physical spatial resolution (grid-point spacing or spectral truncation) may lead to different behaviour in the two model versions. In effect, the dynamical part of each model may lead to dissimilar phase speeds of travelling weather systems resulting in a mismatch at the lateral boundaries. This may call for higher updating frequency or for a domain-wide control of the largest scales that guide the evolution of the synoptic systems (see Biner et al. (2000) and von Storch et al. (2000) on this topic). The physical parameterizations may also cause problems even if they are the same because they may have different responses to the spatial resolution. Our BBE does not address these issues because the grid-point spacings were the same between the Big and the Little Brothers. In fact, the BBE was designed precisely to eliminate these effects in order to concentrate solely on the nesting, without having to sort out the effects just mentioned. Nevertheless, these issues and others, such as the effect of the domain size, the domain location, the season and whether or not an RCM should improve the large-scale circulation of its driving model, will ultimately have to be addressed. Finally, a successful BBE test must be viewed as a necessary but not sufficient condition to prove without any doubts that the one-way nesting RCM approach is a reliable approach.

5. Conclusion

The goal of this paper was to shed some light on two of the most important issues concerning the use of one-way nested RCMs as a downscaling climate technique: the impacts of the *spatial* resolution and *temporal* updating frequency of the lateral boundary conditions. To address these issues, a perfect-prognosis framework called the Big-Brother Experiment, developed by Denis et al. (2001), was employed. This framework consists in using the same model to produce both the control and nested simulations. This approach allowed us to address the above issues separately without mixing nesting errors with those due to possible different formulations between the driving and the nested model. Using this framework with a 45-km grid-point RCM over the North-American East Coast and during winter months, it has been found that:

- Spatial resolution jumps up to 12 between the resolution of the nesting LBC data and the RCM can yield reliable regional climate for most fields studied with an RCM at 45 km resolution.

- Update frequency of twice a day (every 12 hours) are almost sufficient although 6 hours is significantly better and should be used since there is little increase of computational cost related to doing so. No improvement was found by going from 6 to 3 hours in our tests with a 45-km grid-point RCM.

- Although the 500-hPa relative vorticity was the most affected variable when the resolution of the LBC was degraded, the most important climate fields, such as those of the precipitation, temperature, and sea-level pressure fields were far less affected. These last two fields showed the most resistance to the LBC resolution degradation; their largest scales did not need a high-resolution LBC to be well nested, and their stationary fine-scale components are, in turn, strongly forced by the surface heterogeneities and therefore rather independent of the LBC.

- The combination of T32-6 hours currently employed in the Canadian RCM mode of operation seems acceptable, although significant improvements can be anticipated by reducing the spatial resolution jump to 6 from 12 , i.e. by the use of T60 resolution driving data.

Acknowledgements

This work has been financially supported by funding from the Climate Change Prediction Program (CCPP) of the US Dept. of Energy, and from the UQAM regional climate modelling group. We gratefully acknowledge the Meteorological Service of Canada for granting an education leave to the first author during this study and for providing access to its facilities. We are thankful to the UQAM regional climate modelling staff for their invualable technical help with the Canadian RCM. We also thank Dr. Bernard Dugas, Dr. Ramón de Elía and M. Richard Harvey for stimulating discussions.

Appendix

Development of the space-time decomposition for the Taylor diagrams

We describe in this appendix the space-time decomposition performed for comparing the stationary and transient components of two model runs in Taylor diagrams. Given two time series of two-dimensional spatial fields $A=A(x,y,t)$ and $B=B(x,y,t)$, the space-time mean square difference is defined by

$$\left\langle \overline{d_{AB}^2} \right\rangle = \left\langle \overline{(A-B)^2} \right\rangle, \tag{A1}$$

where the space, the time and the time-space averages are given (for $A(x,y,t)$ for instance) by

$$\left\langle A \right\rangle (t) = \frac{1}{N_i} \frac{1}{N_j} \sum_{i=1}^{N_i} \sum_{j=1}^{N_j} A(x_i, y_j, t), \tag{A2}$$

$$\overline{A(x,y)} = \frac{1}{N_p} \sum_{p=1}^{N_p} A(x, y, t_p), \tag{A3}$$

and

$$\left\langle \overline{A} \right\rangle = \frac{1}{N_i} \frac{1}{N_j} \frac{1}{N_p} \sum_{i=1}^{N_i} \sum_{j=1}^{N_j} \sum_{p=1}^{N_p} A(x_i, y_j, t_p) \tag{A4}$$

respectively. N_i, N_j and N_t are the number of data points in x, y, t, respectively.

After expending (A1) and re-arranging the appropriate terms, we can get this space-time form:

$$\left\langle \overline{d_{AB}^{2}} \right\rangle = d_{\langle\overline{A}\rangle\langle\overline{B}\rangle}^{2} + \sigma_{A}^{\circ 2} + \sigma_{B}^{\circ 2} - 2\sigma_{A}^{\circ}\sigma_{B}^{\circ}R_{\mathrm{AB}}^{\circ} \tag{A5}$$

where

$$d_{\langle\overline{A}\rangle\langle\overline{B}\rangle}^{2} = \left(\langle\overline{A}\rangle - \langle\overline{B}\rangle\right)^{2} \tag{A6}$$

is the space-time squared bias,

$$\sigma_{A}^{\circ} = \sqrt{\left\langle \overline{\left(A - \langle\overline{A}\rangle\right)^{2}} \right\rangle} \tag{A7}$$

is the space-time standard deviation of A,

$$\sigma_{B}^{\circ} = \sqrt{\left\langle \overline{\left(B - \langle\overline{B}\rangle\right)^{2}} \right\rangle} \tag{A8}$$

is the space-time standard deviation of B, and

$$R_{\mathrm{AB}}^{\circ} = \frac{\left\langle \overline{\left(A - \langle\overline{A}\rangle\right)\left(B - \langle\overline{B}\rangle\right)} \right\rangle}{\sigma_{A}^{\circ}\sigma_{B}^{\circ}} \tag{A9}$$

is the space-time correlation between A and B.

This form (A5) of the mean square difference can be conveniently represented in the so-called Taylor diagram, which exploits the similarity between the law of cosine

$$c^{2} = a^{2} + b^{2} - 2ab\cos(\phi) \tag{A10}$$

and Eq. (A5) (once the bias term is removed).

One important feature of the (A5) form is that it combines the space and time information, i.e. the comparison between two runs is summarized by one point on a Taylor diagram. But to get a clearer view of the source of the differences, we adopted a form of (A5) in which the differences due to the of stationary and transient components are examined separately.

Equation (A5) can be rewritten as

$$\left\langle \overline{d_{AB}^2} \right\rangle = d_{\langle\overline{A}\rangle\langle\overline{B}\rangle}^2 + d_{\overline{A}\overline{B}}^{*2} + \left\langle \overline{d_{AB}'^2} \right\rangle, \tag{A11}$$

where

$$d_{\overline{A}\overline{B}}^{*2} = \sigma_{\overline{A}}^{*2} + \sigma_{\overline{B}}^{*2} - 2\sigma_{\overline{A}}^{*}\sigma_{\overline{B}}^{*}R_{\overline{A}\overline{B}}^{*} \tag{A12}$$

is the mean square difference expression related to the stationary components and

$$\left\langle \overline{d_{AB}'^2} \right\rangle = \left\langle \overline{\sigma_A'^2} \right\rangle + \left\langle \overline{\sigma_B'^2} \right\rangle - 2\left\langle \overline{\sigma_A'\sigma_B'R_{AB}'} \right\rangle \tag{A13}$$

is the expression related to the transient components. The spatial standard deviations and the spatial correlation of the stationary components in Eq. (A12) are given by

$$\sigma_{\overline{A}}^{*} = \sqrt{\left\langle \left(\overline{A} - \left\langle \overline{A} \right\rangle\right)^2 \right\rangle}, \tag{A14}$$

$$\sigma_{\overline{B}}^{*} = \sqrt{\left\langle \left(\overline{B} - \left\langle \overline{B} \right\rangle\right)^2 \right\rangle} \tag{A15}$$

and

$$R_{\overline{A}\overline{B}}^{*} = \frac{\left\langle \left(\overline{A} - \left\langle \overline{A} \right\rangle\right)\left(\overline{B} - \left\langle \overline{B} \right\rangle\right) \right\rangle}{\sigma_{\overline{A}}^{*}\sigma_{\overline{B}}^{*}} \tag{A16}$$

respectively.

For the expression of the transient component difference (A13), the temporal standard deviations and the temporal correlation are given by

$$\sigma'_A = \sqrt{\overline{\left(A - \overline{A}\right)^2}}, \tag{A17}$$

$$\sigma'_B = \sqrt{\overline{\left(B - \overline{B}\right)^2}}, \tag{A18}$$

and

$$R'_{AB} = \frac{\overline{\left(A - \overline{A}\right)\left(B - \overline{B}\right)}}{\sigma'_A \sigma'_B} \tag{A19}$$

respectively.

Eq. (A13) is not directly admissible for a Taylor diagram since it does not follow the law of cosine in a strict sense due to the last term on the right-hand side. Eq. (A13) is therefore modified as

$$\left\langle \overline{d'^2_{AB}} \right\rangle = \left\langle \sigma'^2_A \right\rangle + \left\langle \sigma'^2_B \right\rangle - 2\left\langle \sigma'^2_A \right\rangle^{1/2} \left\langle \sigma'^2_B \right\rangle^{1/2} R'^e_{AB} \tag{A20}$$

with an "effective" correlation R'^e_{AB} defined as a weighted average

$$R'^e_{AB} = \frac{\left\langle \sigma'_A \sigma'_B R'_{AB} \right\rangle}{\left\langle \sigma'^2_A \right\rangle^{1/2} \left\langle \sigma'^2_B \right\rangle^{1/2}}. \tag{A21}$$

Finally, the stationary and transient expressions are normalised by their respective variances of *B(x,y,t)* such that identical simulations will show up on the diagram as a point located on the abscissa at unit distance from the origin (i.e. same variances and a correlation coefficient of 100%). These final expressions for the stationary and transient components are given by

$$\frac{d^{*2}_{\overline{A}\,\overline{B}}}{\sigma^{*2}_{\overline{B}}} = 1 + \frac{\sigma^{*2}_{\overline{A}}}{\sigma^{*2}_{\overline{B}}} - 2\frac{\sigma^{*}_{\overline{A}}}{\sigma^{*}_{\overline{B}}} R^{*}_{\overline{A}\,\overline{B}} \tag{A22}$$

and

$$\frac{\left\langle \overline{d'^2_{AB}} \right\rangle}{\left\langle \sigma'^2_B \right\rangle} = 1 + \frac{\left\langle \sigma'^2_A \right\rangle}{\left\langle \sigma'^2_B \right\rangle} - 2\frac{\left\langle \sigma'^2_A \right\rangle^{1/2}}{\left\langle \sigma'^2_B \right\rangle^{1/2}} R'^{e}_{AB} \tag{A23}$$

respectively.

References

Bergeron, G., R. Laprise, and D. Caya, 1994: *Formulation of the Mesoscale Compressible Community (MC2) model.* Cooperative Centre for Research in Mesometeorology, 165 pp., [Available from Dr. D. Caya, Groupe des Sciences de l'Atmosphère, Département des Sciences de la Terre et de l'Atmosphère, Université du Québec à Montréal, C.P. 8888, Succursale "Centre-Ville," Montréal, PQ, H3C 3P8, Canada]

Biner, S., D. Caya, R. Laprise, and L. Spacek, 2000: Nesting of RCMs by imposing large scales., 7.3-7.4. In: Research activities in Atmospheric and Oceanic Modelling, WMO/TD - No. 987, Report No. 30.

Boer, G. J., and S. J. Lambert, 2001: Second-order space-time climate difference statistics. *Climate Dyn.*, **17**, 213-218.

CAS/JSC WGNE, 1999: *Report of Fourteenth Session of the CAS/JSC Working Group on Numerical Experimentation (Recherche en Prévision Numérique, Environnement Canada, Doval, Québec, Canada, 2-6 November 1998).* No. 14, WMO/TD-NO. 964, World Meteor. Org., 28 pp.

CAS/JSC WGNE, 2000: *Report of Fifteenth Session of the CAS/JSC Working Group on Numerical Experimentation (Naval Research Laboratory, Monterey, CA, USA, 25-29 October 1999).* No. 15, WMO/TD-NO. 1024, World Meteor. Org., 29 pp.

Caya, D., and R. Laprise, 1999: A semi-implicit semi-Lagrangian regional climate model: The Canadian RCM. *Mon. Wea. Rev.*, **127**, 341-362.

Davies, H. C., 1976: A lateral boundary formulation for multi-level prediction models. *Quart. J. Roy. Meteor. Soc.*, **102**, 405-418.

de Elía, R., R. Laprise, and B. Denis, 2001: Scale-dependent predictability of a limited-area model. *Submited to Mon. Wea. Rev.*

Denis, B., J. Côté, and R. Laprise, 2001a: Spectral decomposition of two-dimensional atmospheric fields on limited-area domains using the discrete cosine transform (DCT). *Mon. Wea. Rev. (submitted).*

Denis, B., R. Laprise, D. Caya, and J. Côté, 2001b: Downscaling ability of one-way nested regional climate models: the big-brother experiment. *Accepted for publication in Climate Dyn.*

Giorgi, F., and L. O. Mearns, 1999: Introduction to special section: regional climate modeling revisited. *J. Geophys. Res.*, **104**, 6335-6352.

Kain, J. S., and J. M. Fritsch, 1990: A one-dimensional entraining/detraining plume model and its application in convective parameterization. *J. Atmos. Sci.*, **47**, 2784-2802.

Laprise, R., D. Caya, G. Bergeron, and M. Giguère, 1997: The formulation of André Robert MC2 (Mesoscale Compressible Community) model. The André J. Robert Memorial Volume (C. Lin, R. Laprise and H. Ritchie, Eds.), companion volume to *Atmos.-Ocean*, **35**, 195-220.

Laprise, R., D. Caya, M. Giguère, G. Bergeron, H. Côté, J.-P. Blanchet, G. Boer, and A. N. McFarlane, 1998: Climate and climate change in western Canada as simulated by the Canadian regional climate model. *Atmos.-Ocean*, **36**, 119-167.

Laprise, R., M. K. Ravi Varma, B. Denis, D. Caya, and I. Zawadzki, 2000: Predictability in a nested limited-area model. *Mon. Wea. Rev.*, **128**, 4149-4154.

Laprise, R., and P. Zwack, 1992: Variation de l'activité cyclonique dans un scénario double CO2. *Le Climat*, **10**, 39-62.

Majewski, D., 1997: Operational Regional Prediction. *Meteorol. Atmos. Phys.*, **63**, 89-104.

McFarlane, N. A., G. J. Boer, J.-P. Blanchet, and M. Lazare, 1992: The Canadian Climate Centre second-generation general circulation model and its equilibrium climate. *J. Climate*, **5**, 1013-1044.

Robert, A., and E. Yakimiw, 1986: Identification and elimination of an inflow boundary computational solution in limited area model integrations. *Atmos.-Ocean*, **24**, 369-385.

Taylor, K. E., 2001: Summarizing multiple aspects of model performance in a single diagram. *J. Geophys. Res.*, **106**, 7183-7192.

von Storch, H., H. Langenberg, and F. Feser, 2000: A spectral nudging technique for dynamical downscaling purposes. *Mon. Wea. Rev.*, **128**, 3664–3673.

Yakimiw, E., and A. Robert, 1990: Validation experiments for a nested grid-point regional forecast model. *Atmos.-Ocean*, **28**, 466-472.

Figures

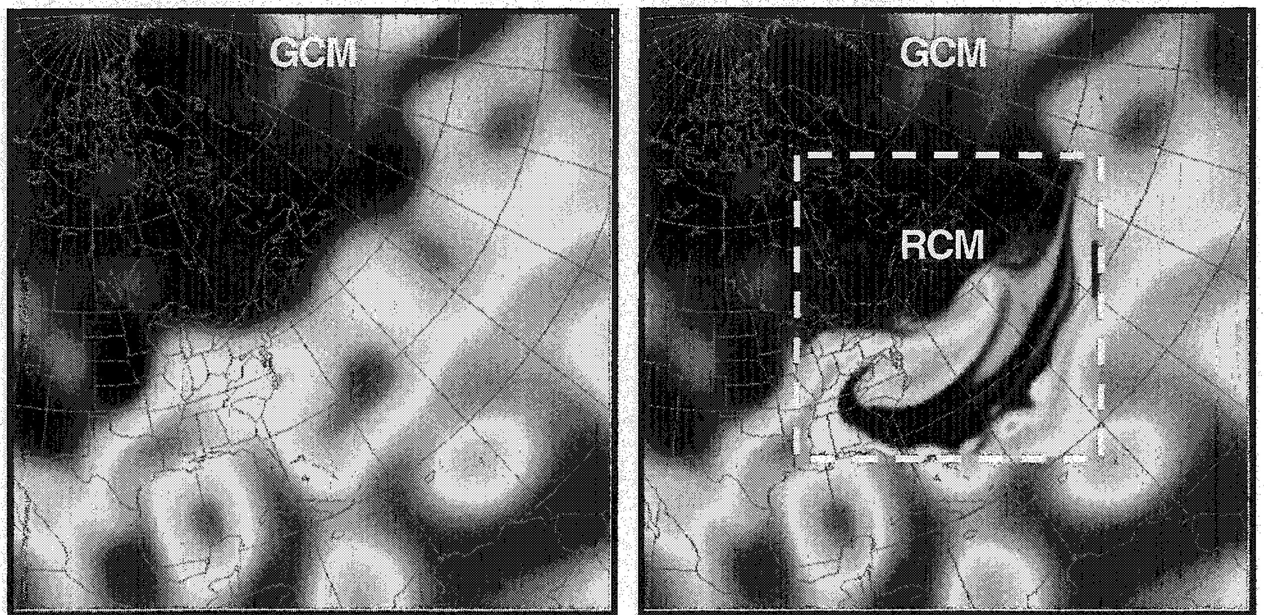

Fig. 1. Fine-scale feature generation from a one-way nested RCM. Left: GCM at T32 (600 km) resolution. Right: a 45 km-resolution RCM nested in the T32 GCM. The field shown is a winter snapshot of low-level specific humidity.

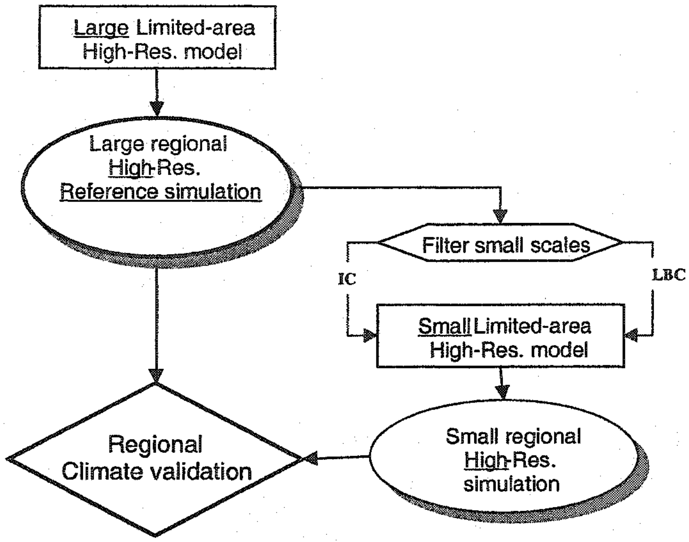

Fig. 2. Simplified flowchart illustrating the BBE framework. Rectangles are the models and ovals are the datasets. The diamond represents validation of the little-brother regional-scale features against those existing in the reference big-brother dataset. The initial conditions (IC) and lateral boundary conditions (LBC) for the small-domain model (right branch) are spatially filtered such that the smallest scales are removed.

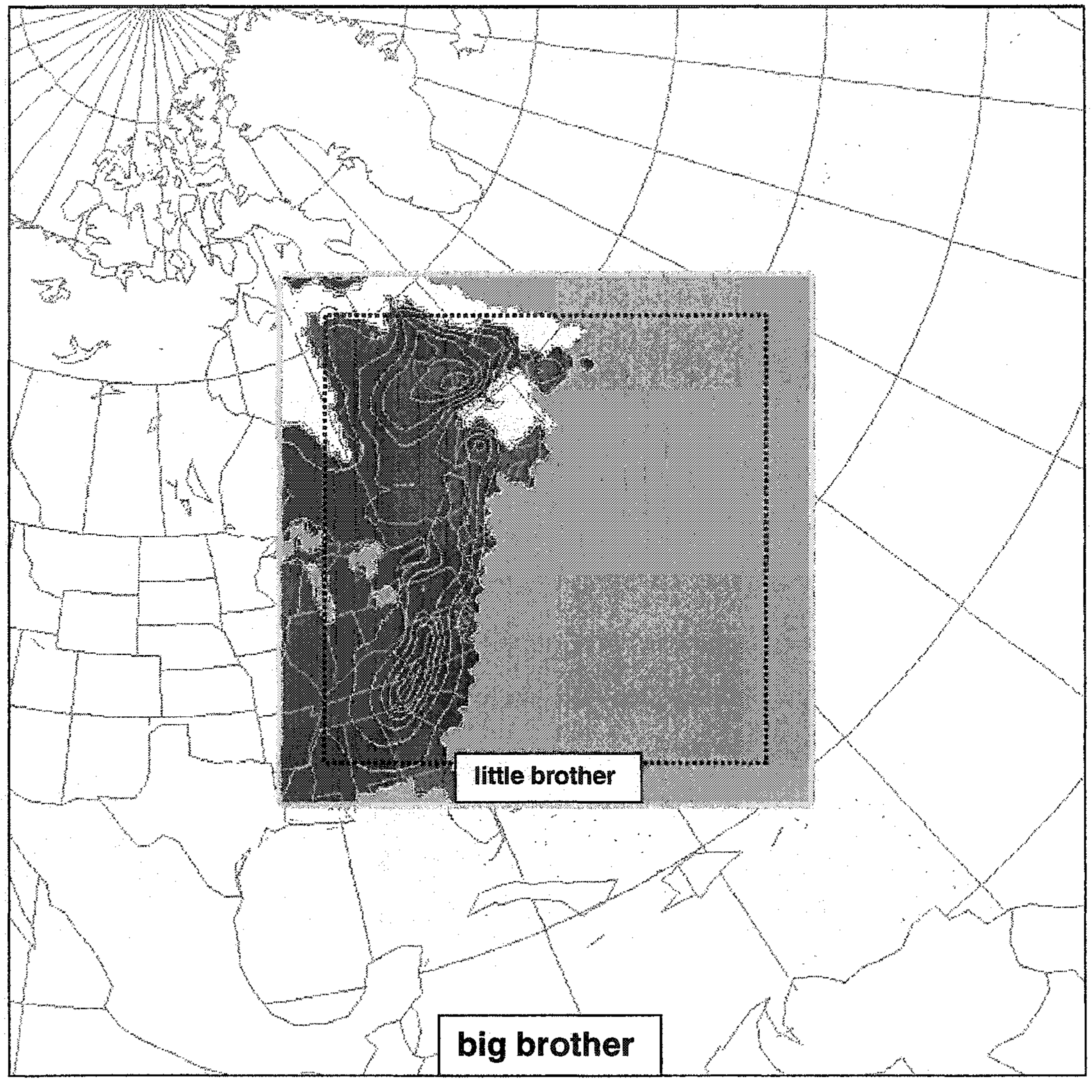

Fig. 3. Large big-brother domain and nested smaller little-brother domain, over North-Eastern America. The dashed line around the little-brother domain represents the width of the nesting zone. The topographic field and the land/open-water/sea-ice masks are also shown but only for the Little Brother for clarity. The topography is contoured at every 100 m. Open-water areas are grey and sea-ice areas are white.

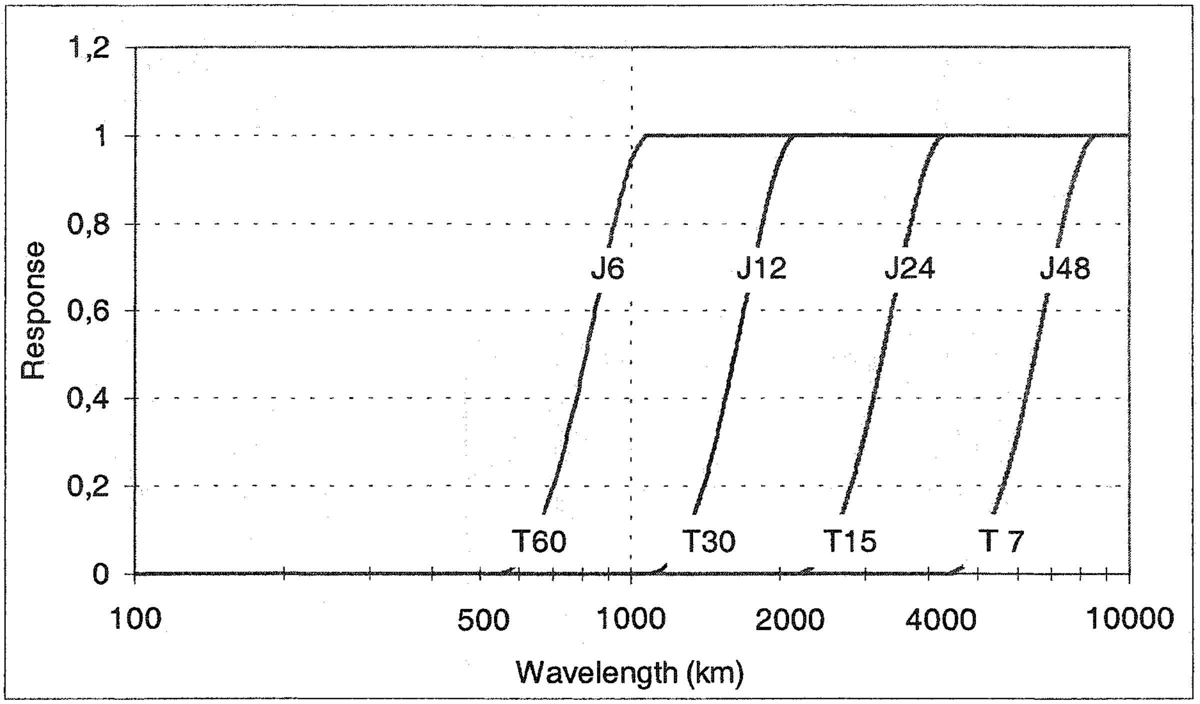

Fig. 4. Response curves of the spectral filter used to degrade the resolution of the driving data. The four resolution jumps are labelled J6, J12, J24 and J48 (jump of 6, 12, 24 and 48 times the original 45-km grid resolution). The corresponding spectral triangular spherical truncations T60, T30, T15 and T7, are also given for reference; they have been loosely deduced by dividing the Earth circumference by the truncation number.

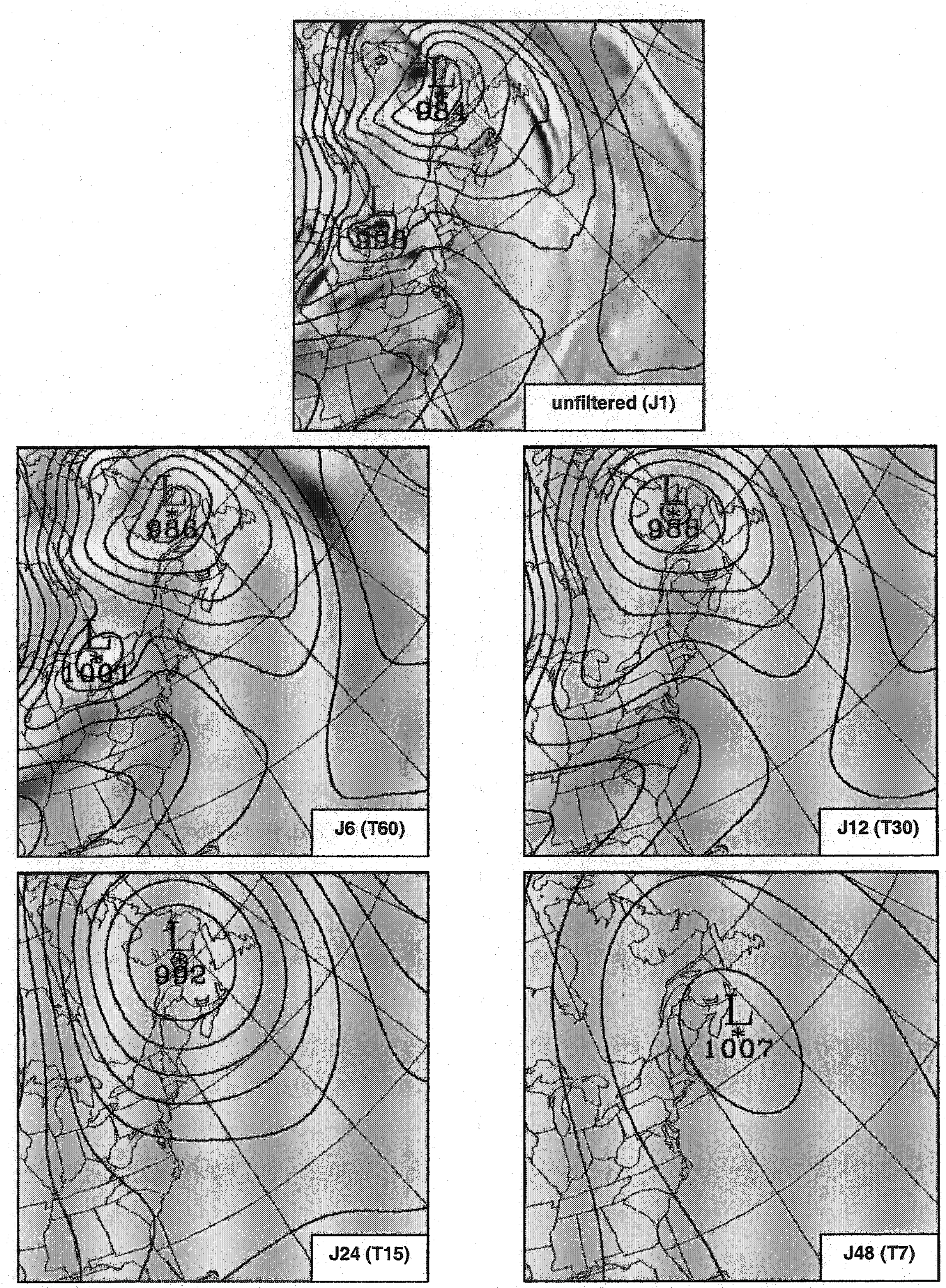

Fig. 5. Examples of filtering corresponding to the response curves of Fig. 4. On each panel the sea-level pressure field is shown with contours and the relative vorticity field is in grey tones. The atmospheric situation is a snapshot of a simulated February 1993. The domain corresponds to the little-brother domain.

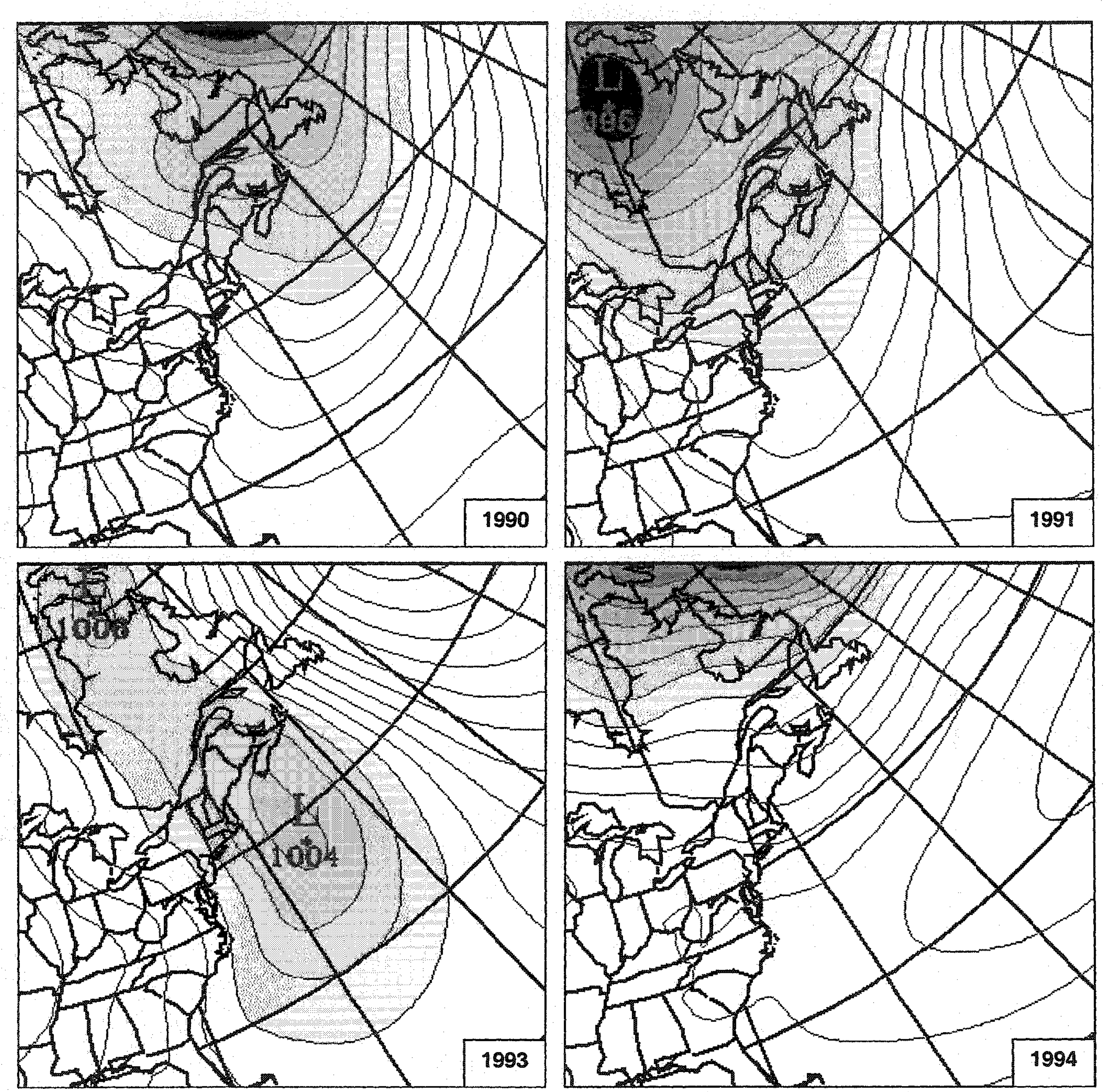

Fig. 6. Big-brother monthly-mean sea-level pressure for February of 1990, 1991, 1993 and 1994. Contours are at every 2 hPa. Areas with values lower than 1010 hPa are shaded. The fields are shown on the little-brother domain.

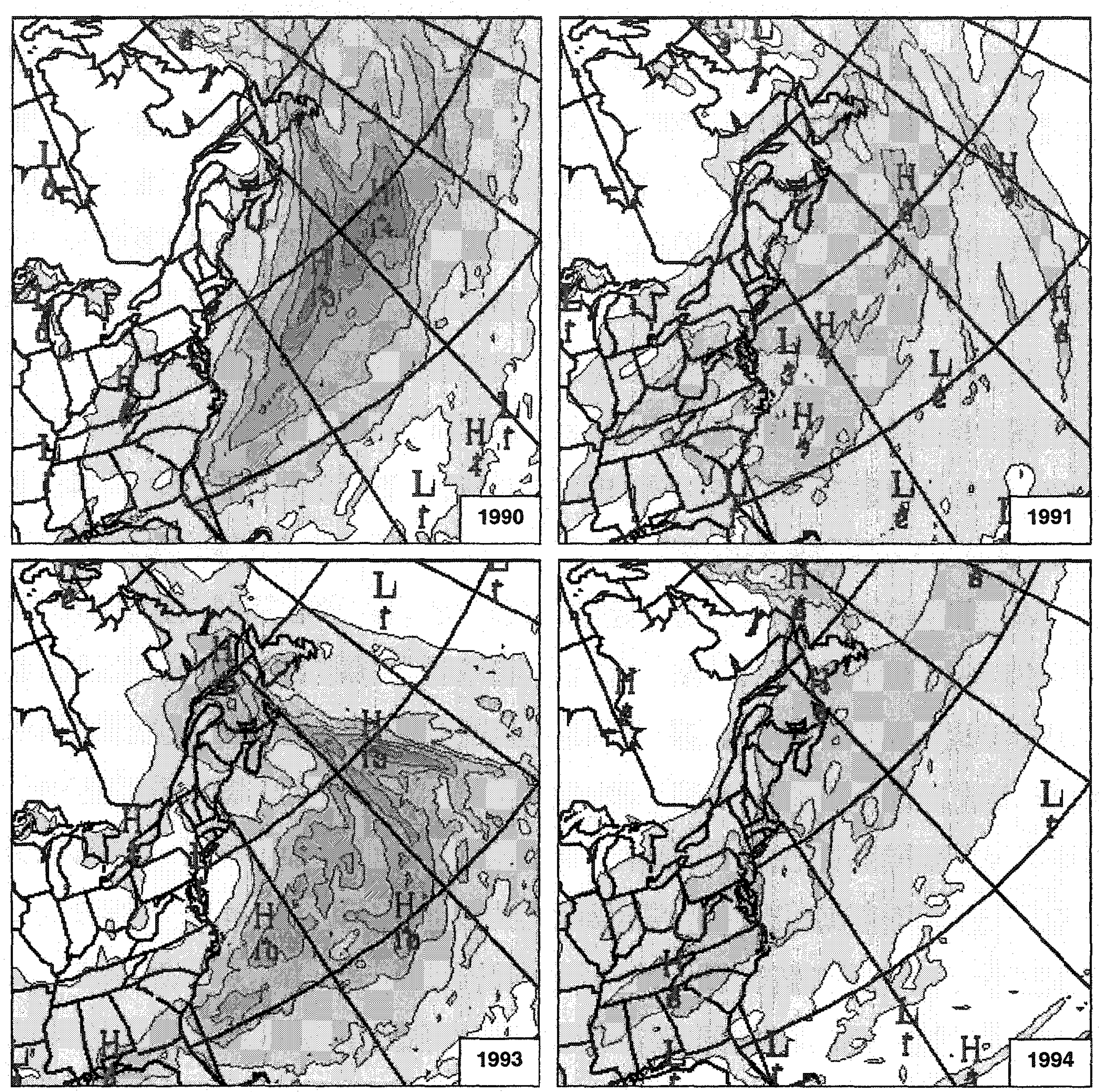

Fig. 7. Big-brother monthly-mean precipitation rates for February of 1990, 1991, 1993 and 1994. Contours are at every 2 mm per day. Areas with values higher than 2 mm per day are shaded.

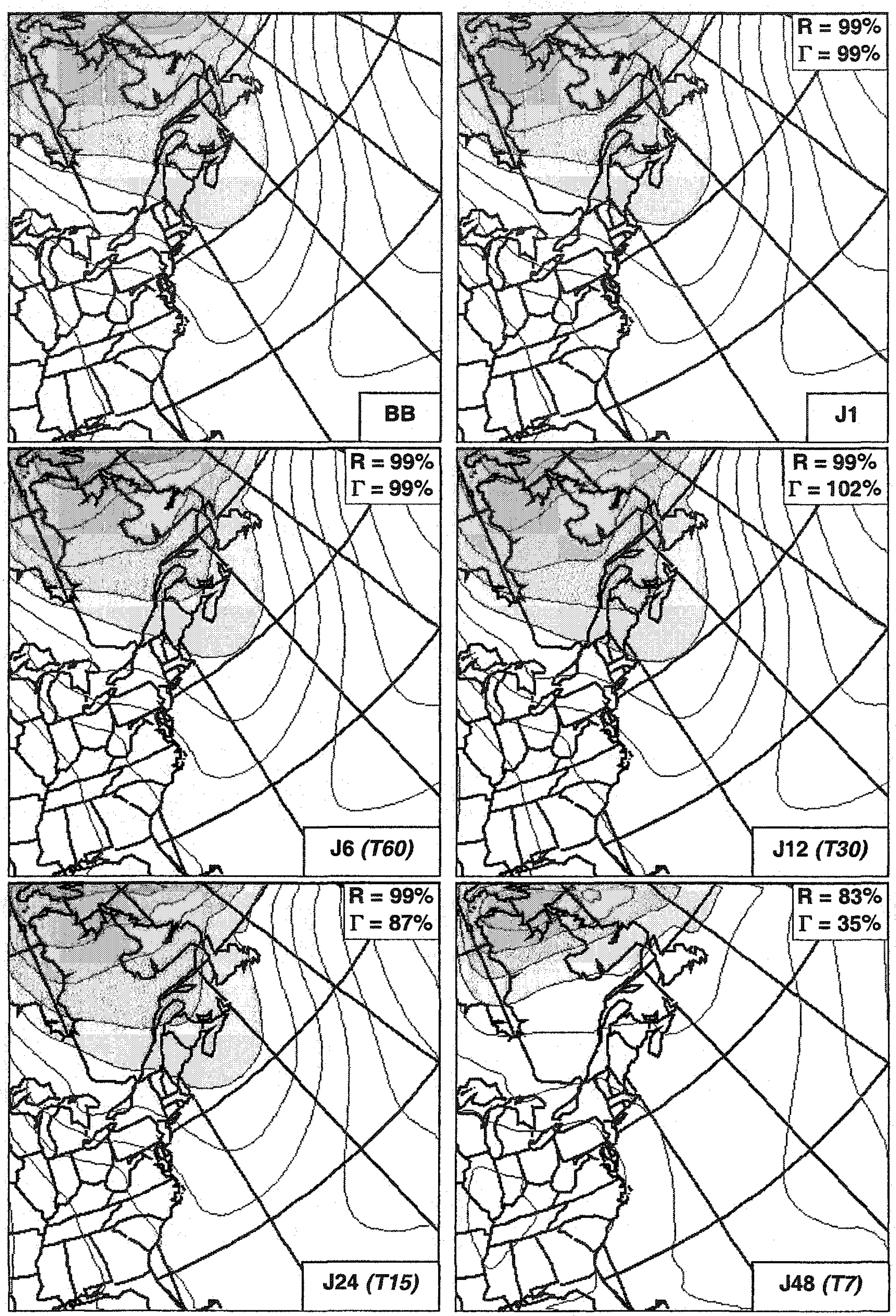

Fig. 8. Sea-level pressure (slp) fields averaged over four February months. Contours are at every 2 hPa. Areas with values lower than 1010 hPa are shaded. The resolution jumps (**J**), as well as the corresponding spherical triangular truncations (**T**), are indicated on the lower-right corners. Correlation coefficients (**R**) and variance ratios (Γ) between the little-brother and big-brother panels are indicated in the upper-right corners.

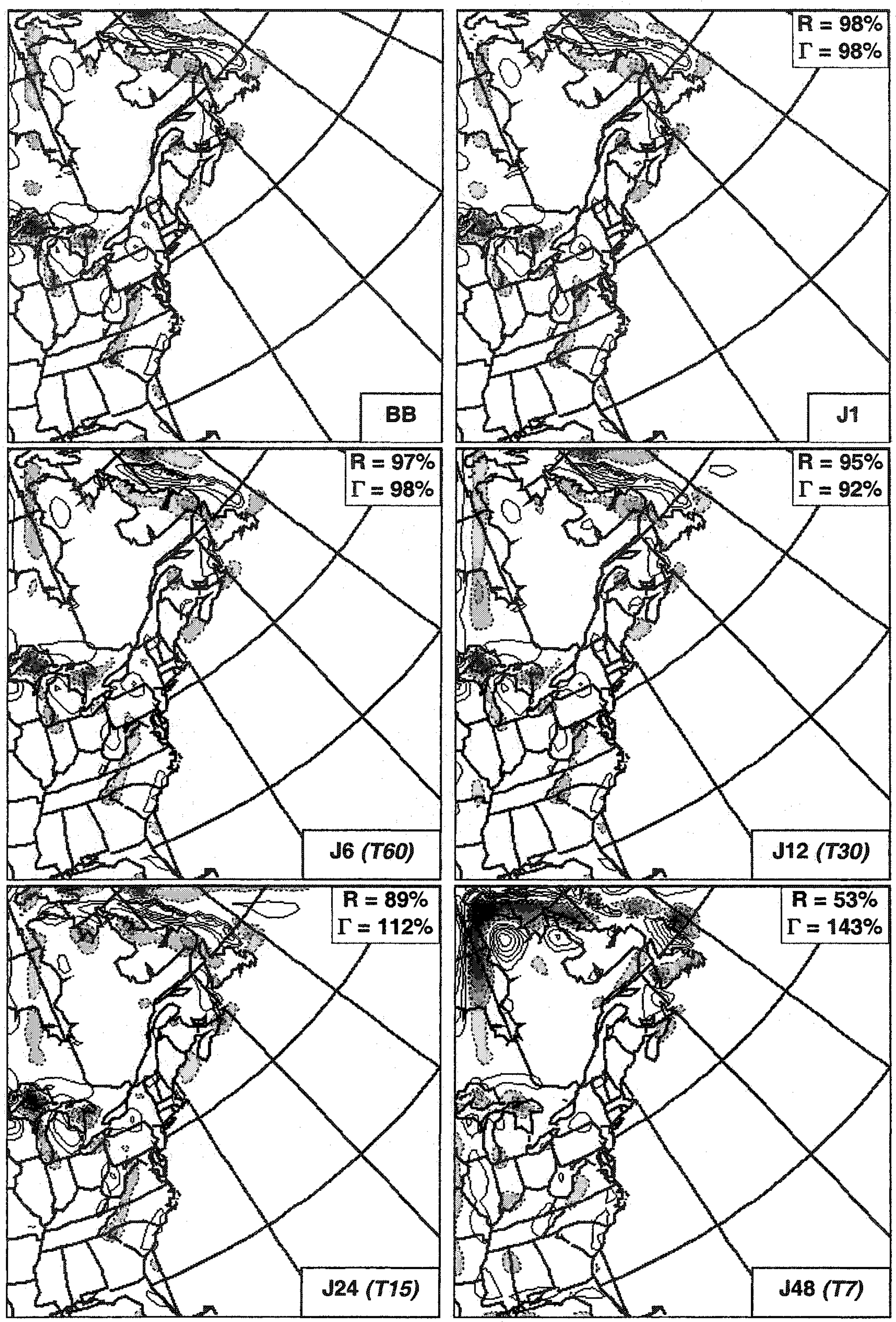

Fig. 9. Stationary small-scale component of slp (over four February months). Contour intervals are at every 0.1 hPa. The zero contour is omitted for clarity. Correlation coefficients (**R**) and variance ratios (Γ) between the little-brother and big-brother panels are in the upper-right corners.

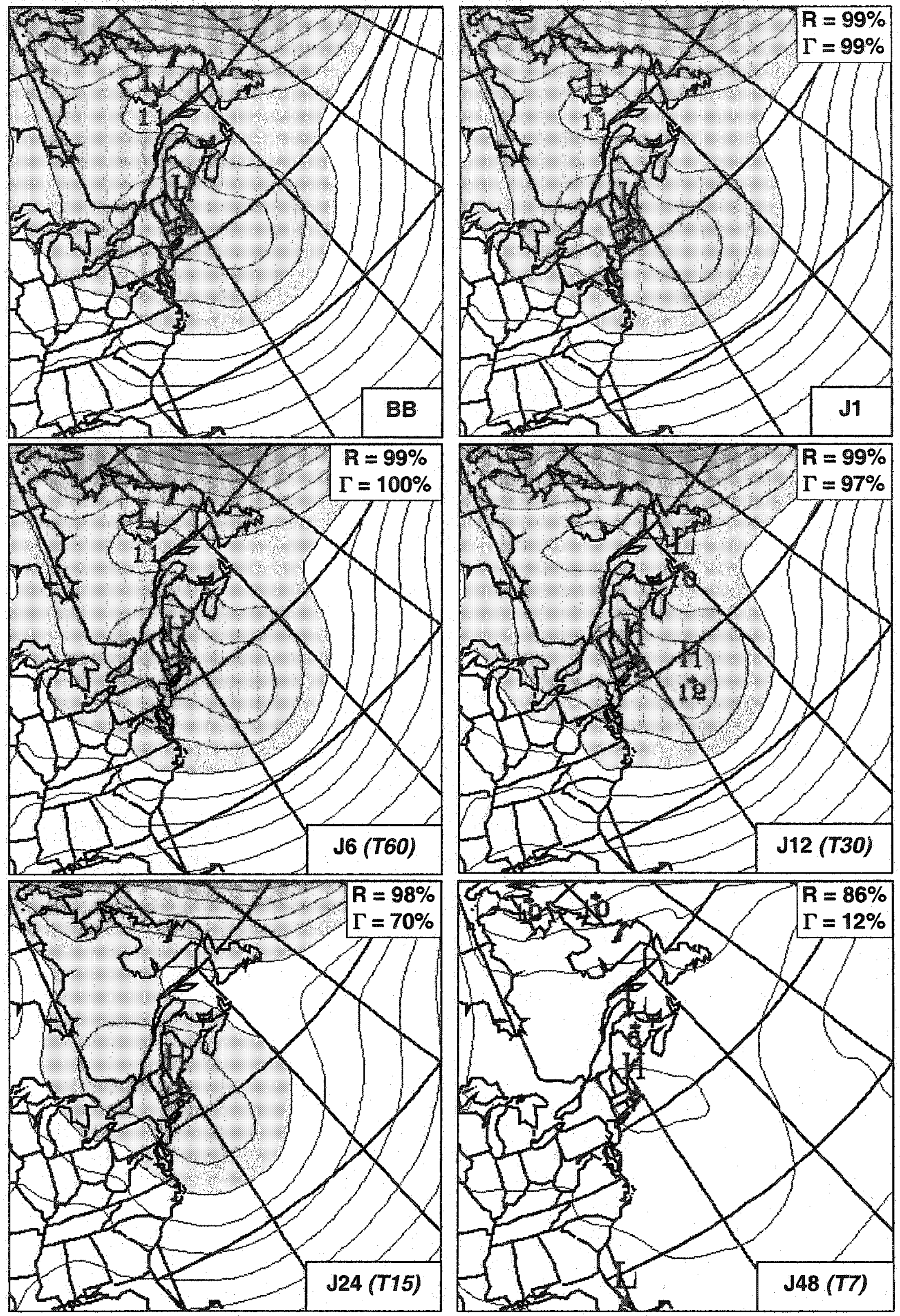

Fig. 10. Transient-eddy standard deviations of slp. Contours are at every 1.0 hPa. Areas with values larger than 10 hPa are shaded.

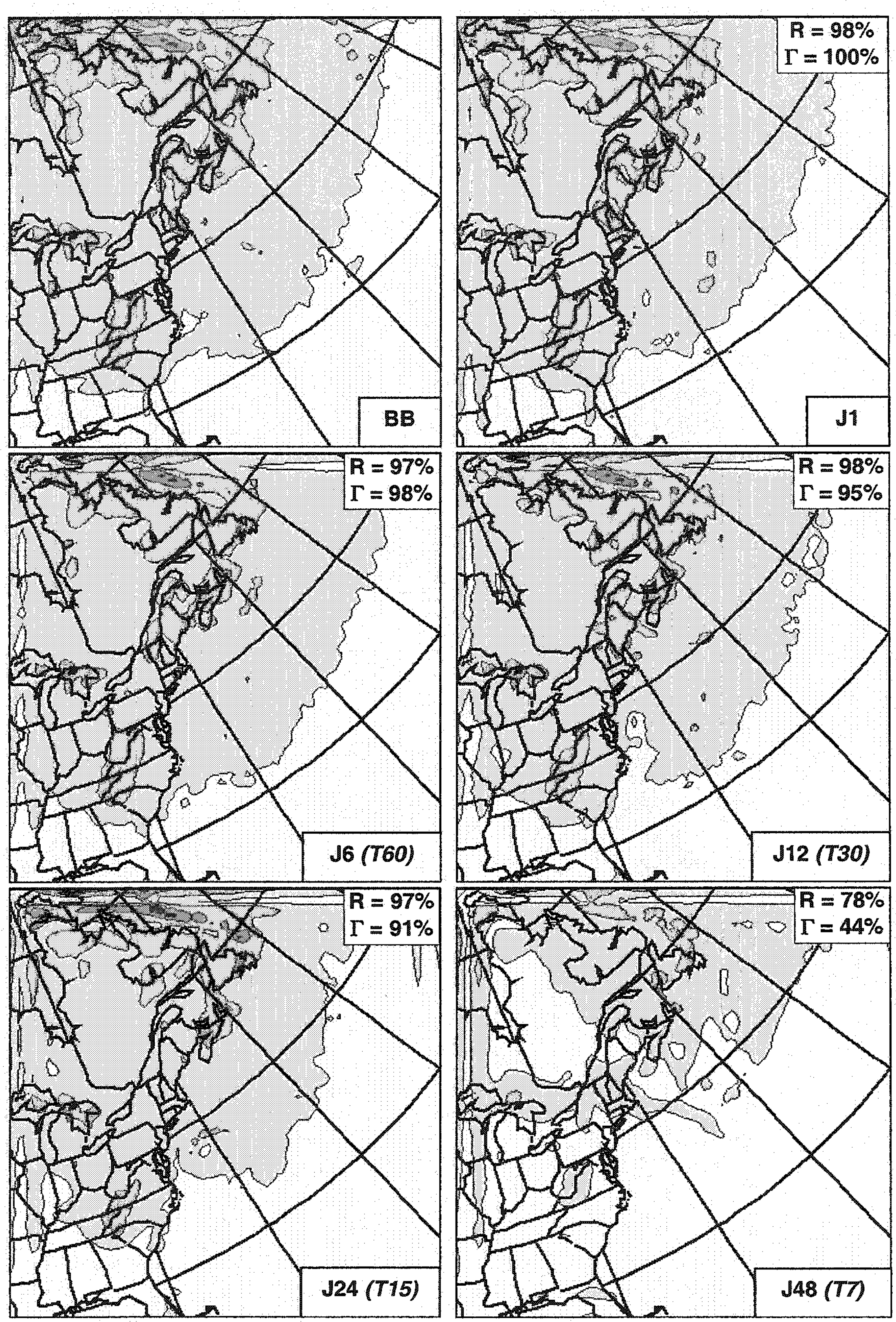

Fig. 11. Transient-eddy standard deviations of the small-scale component of slp. Contours are at every 0.2 hPa. Areas with values larger than 0.2 hPa are shaded.

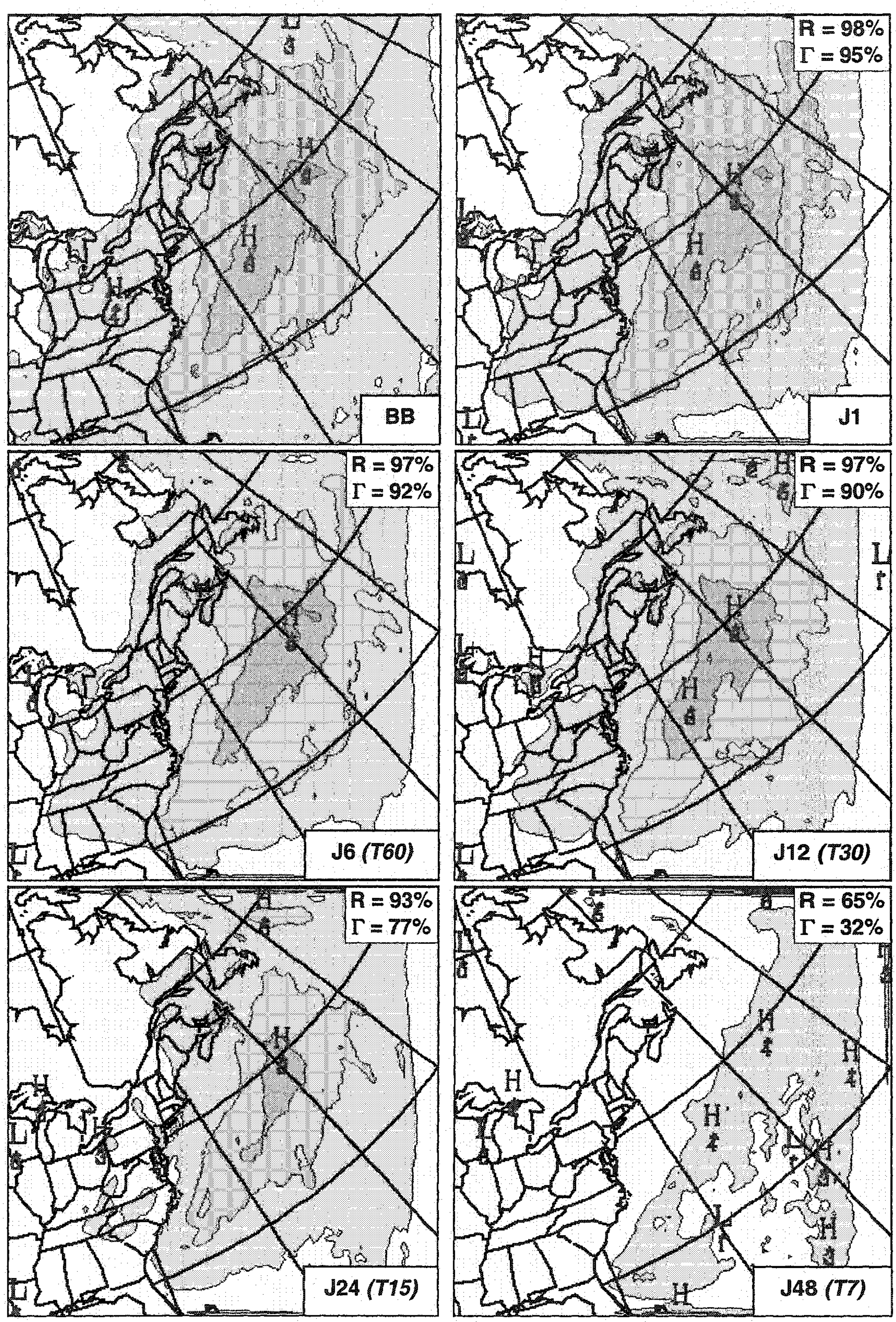

Fig. 12. Precipitation rates averaged over four February months. Contours are at every 2 mm per day. Areas with values larger than 2 mm per day are shaded.

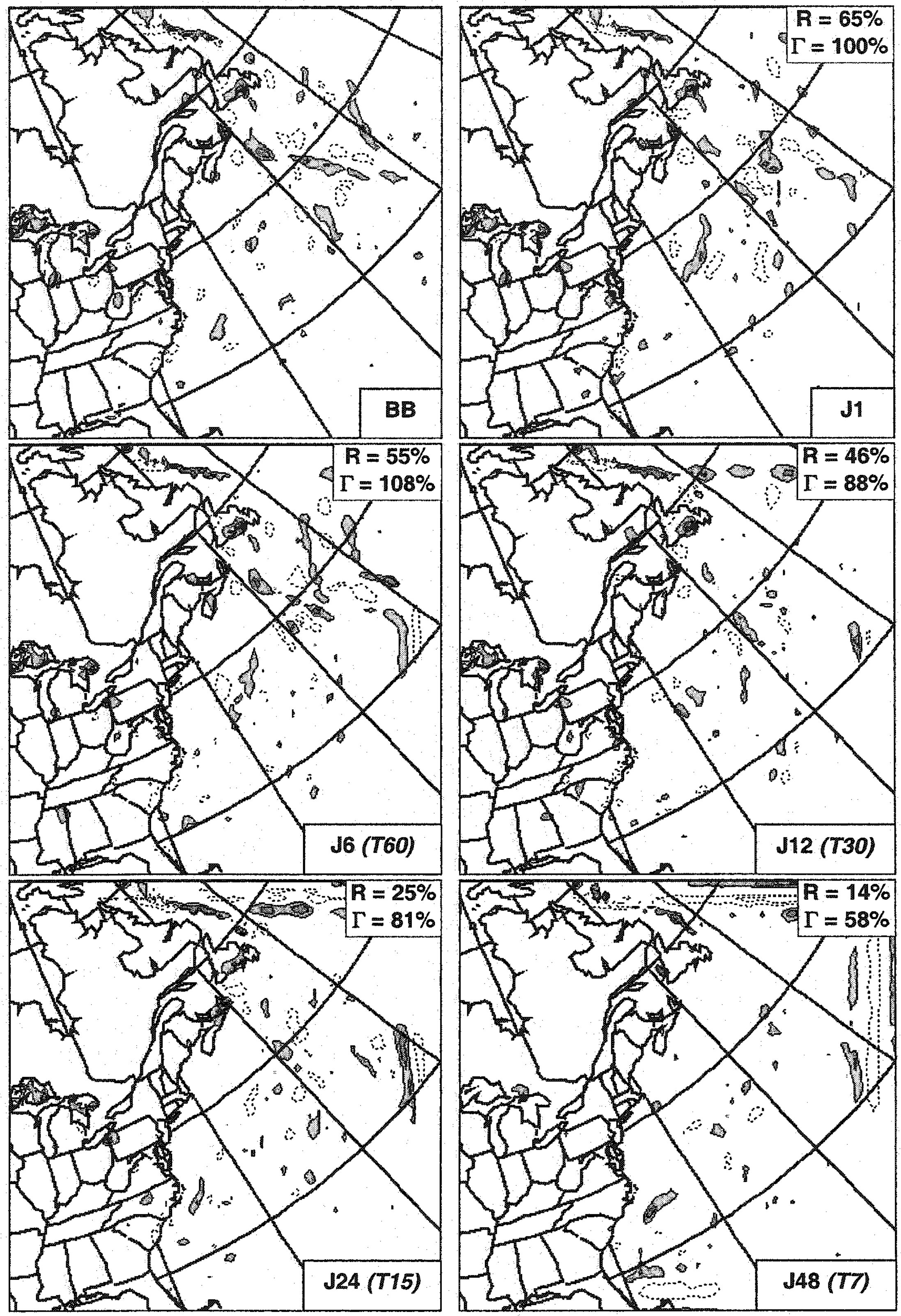

Fig. 13. Stationary small-scale component of precipitation rates. Contour intervals are [-5, -3, -1, -0.5, 0.5, +1, +3, +5] mm day $^{-1}$. Regions with values larger than 0.5 mm day $^{-1}$ are shaded.

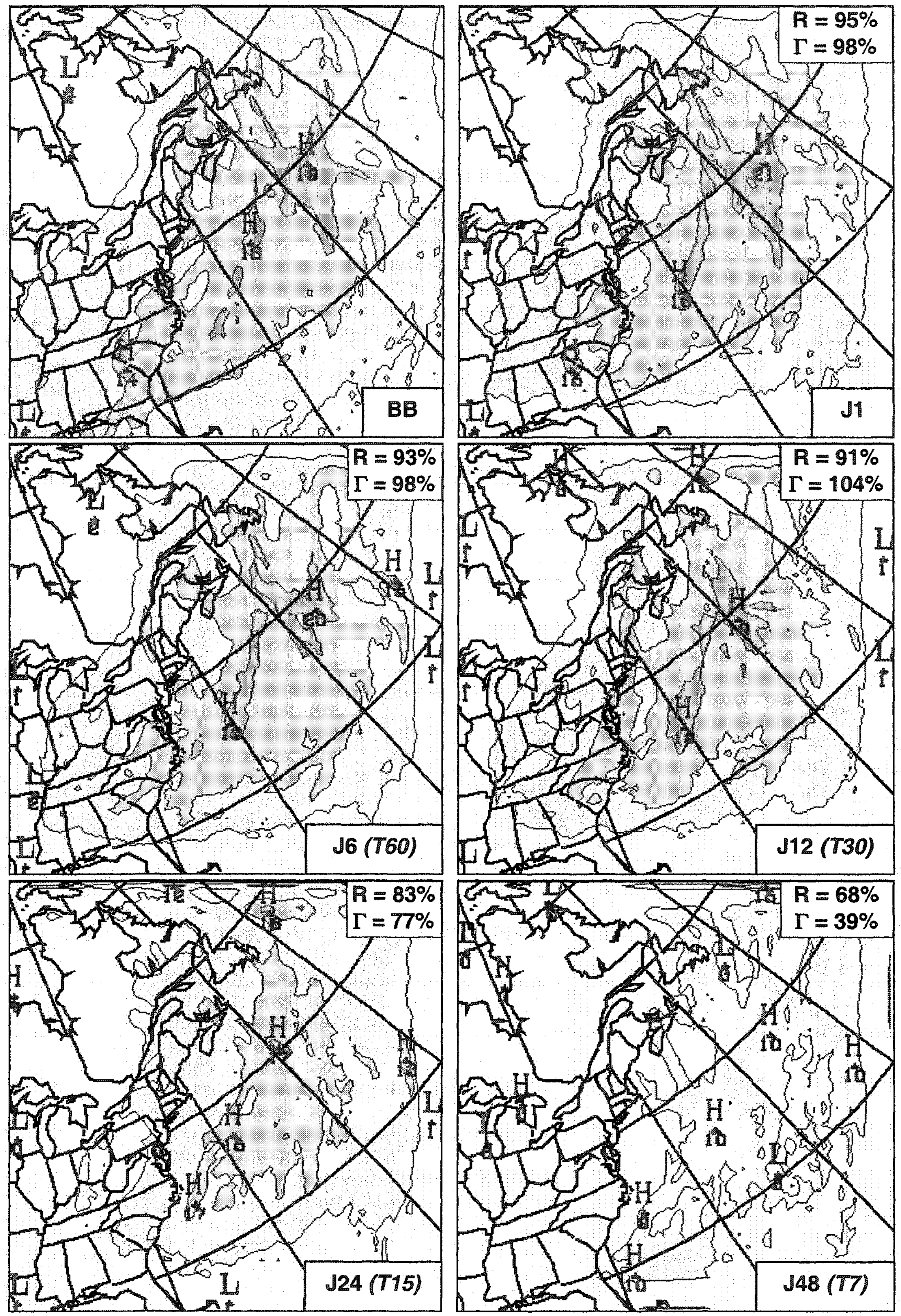

Fig. 14. Transient standard deviations of precipitation rates. Contours are at every 5 mm per day. Areas with values larger than 5 mm per day are shaded.

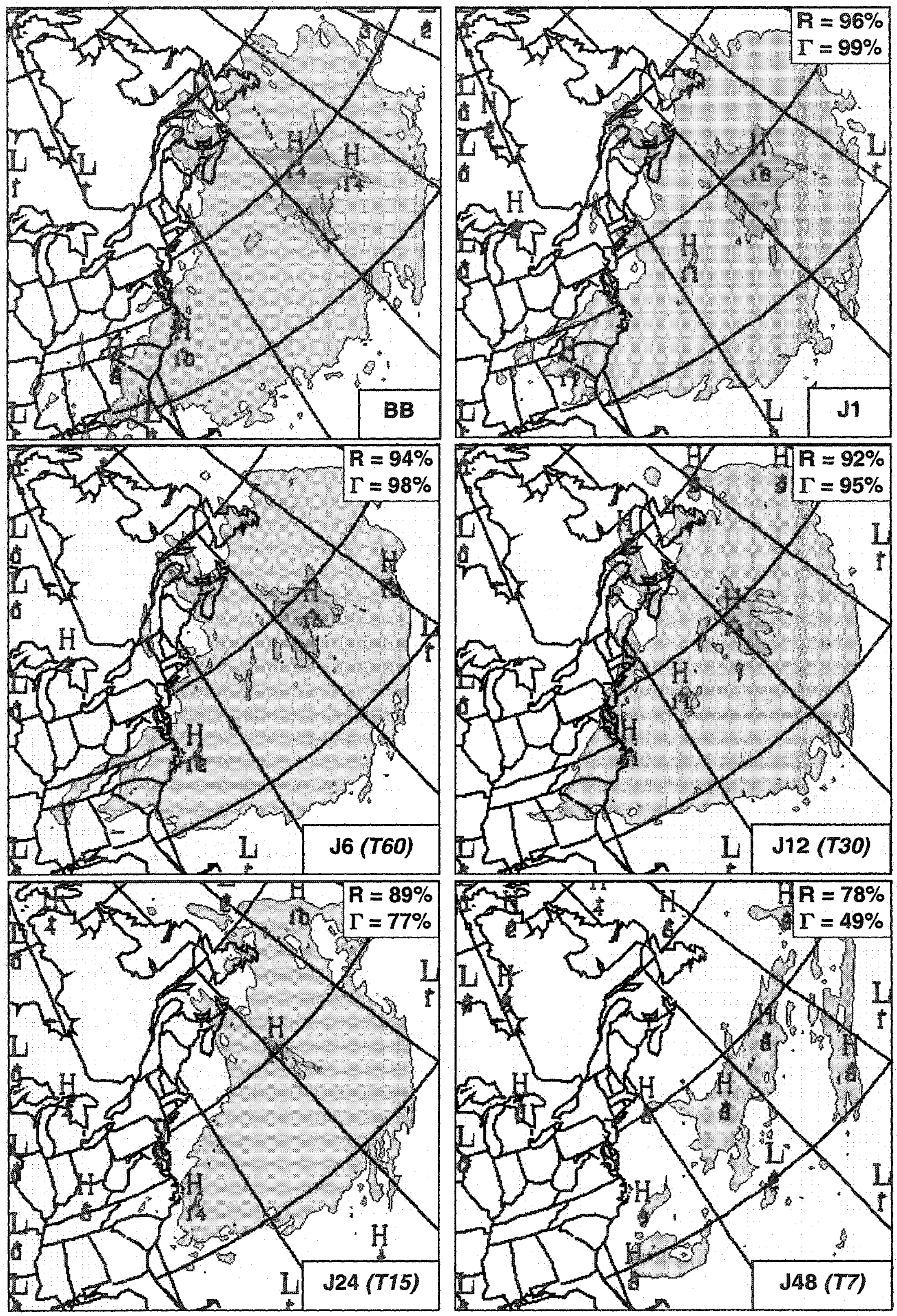

Fig. 15. Transient standard deviations of the small-scale component of the precipitation rates. Contours are at every 5 mm per day. Areas with values larger than 5 mm per day are shaded.

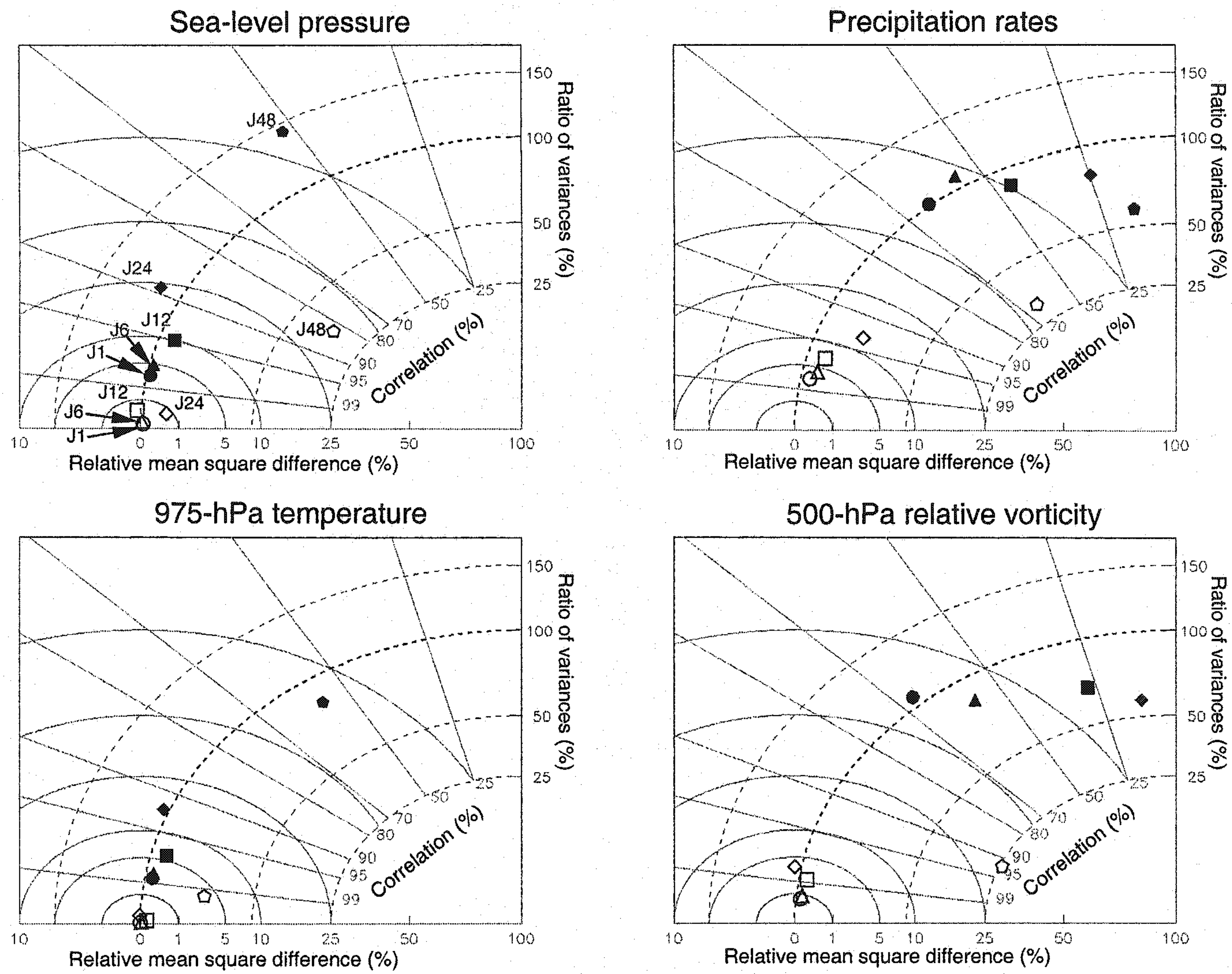

Fig. 16. Taylor diagrams showing the effect of the resolution jumps of the *stationary* component of the sea-level pressure, precipitation rates, 975-hPa temperature and 500-hPa vorticity fields. Circles: J1, triangles: J6, squares: J12, diamonds: J24 and pentagons: J48. The open symbols are for the total fields and the filled ones are for their small-scale components only.

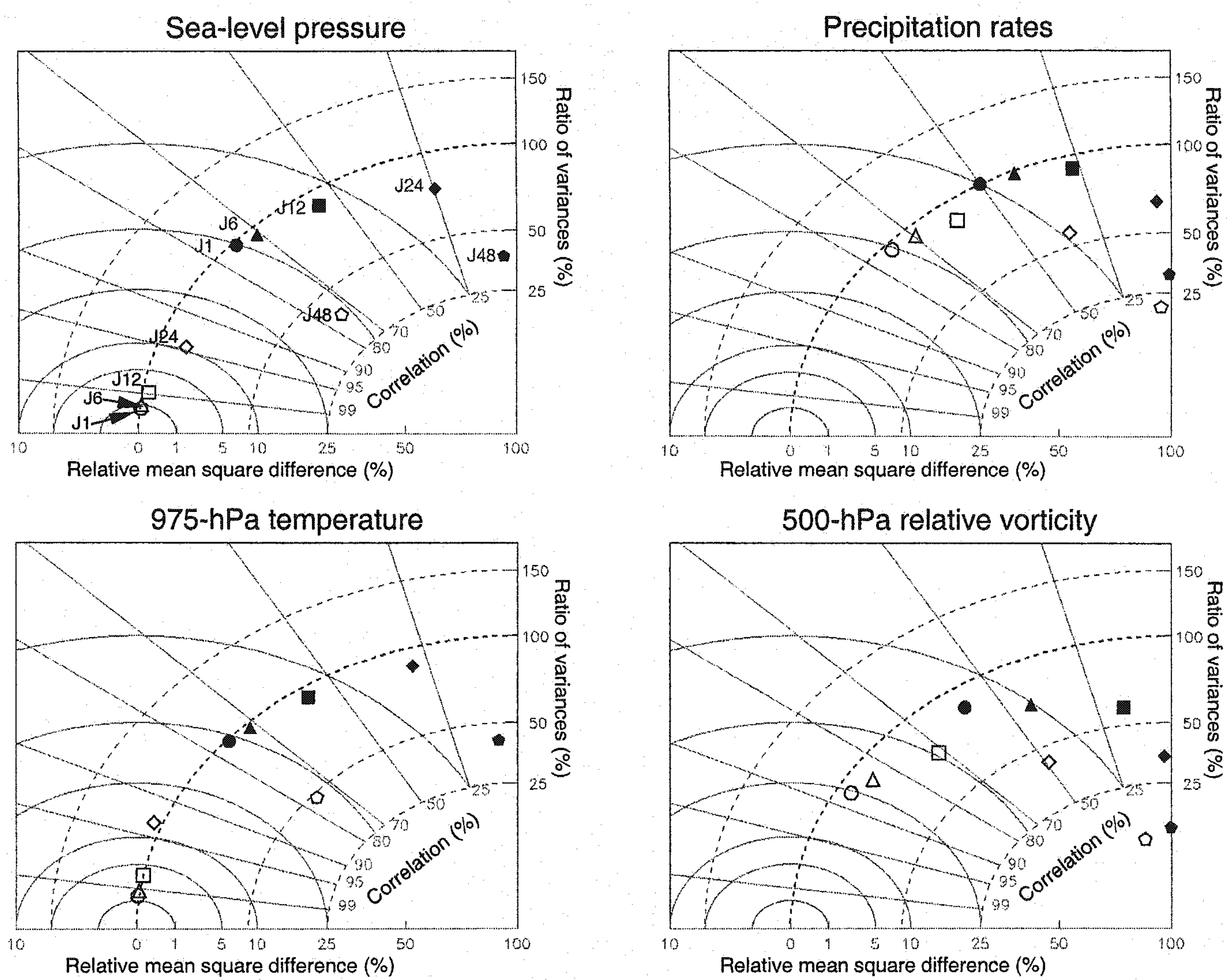

Fig. 17. Same as in Fig. 16, but for the *transient* component of the fields.

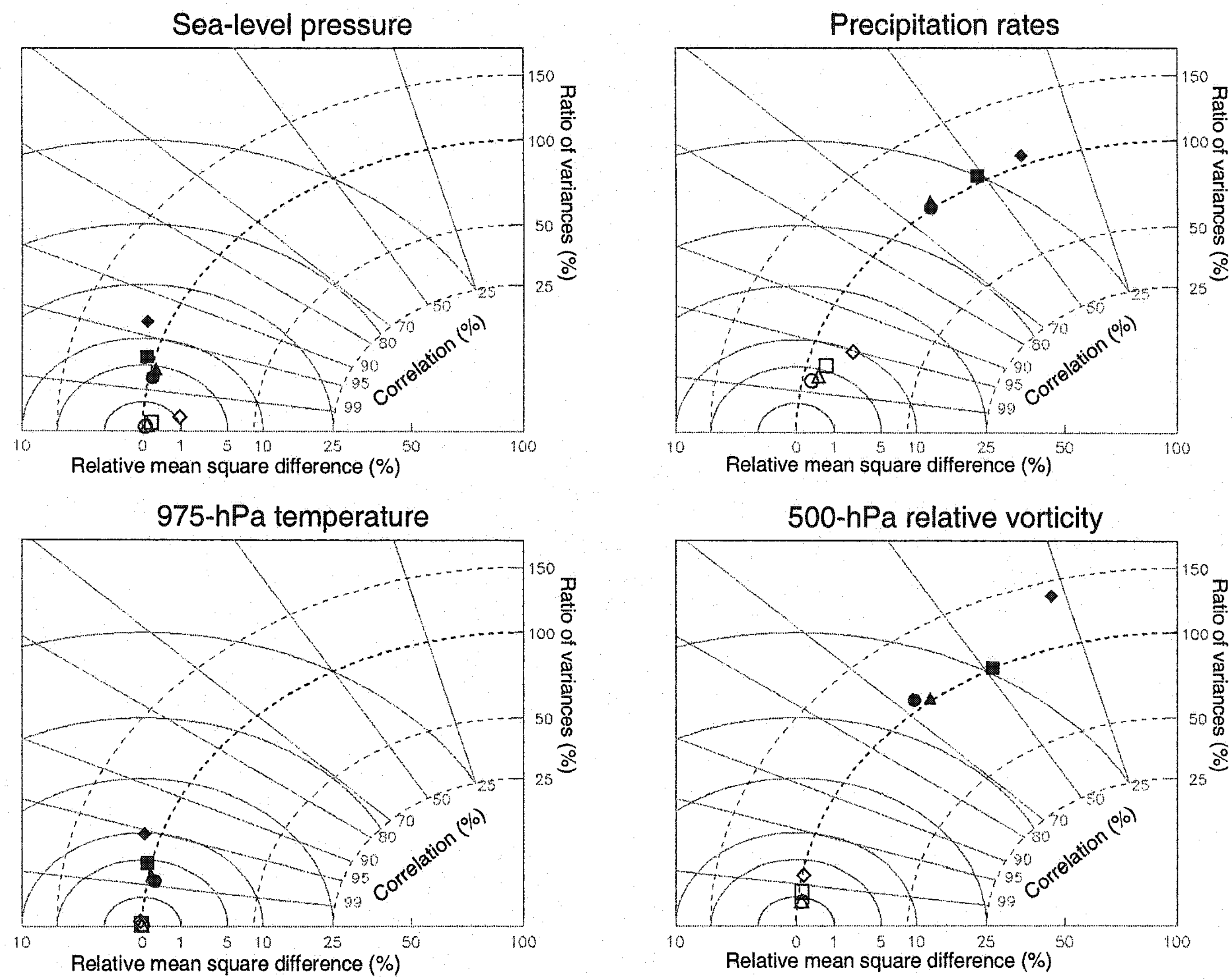

Fig. 18. Taylor diagrams showing the effect of update frequency on the *stationary* component of the sea-level pressure, precipitation rates, 975-hPa temperature and 500-hPa vorticity fields. Circles: U8 (3 h), triangles: U4 (6 h), squares: U2 (12 h), diamonds: U1 (24 h). The open symbols are for the total fields and the filled ones are for their small-scale components only.

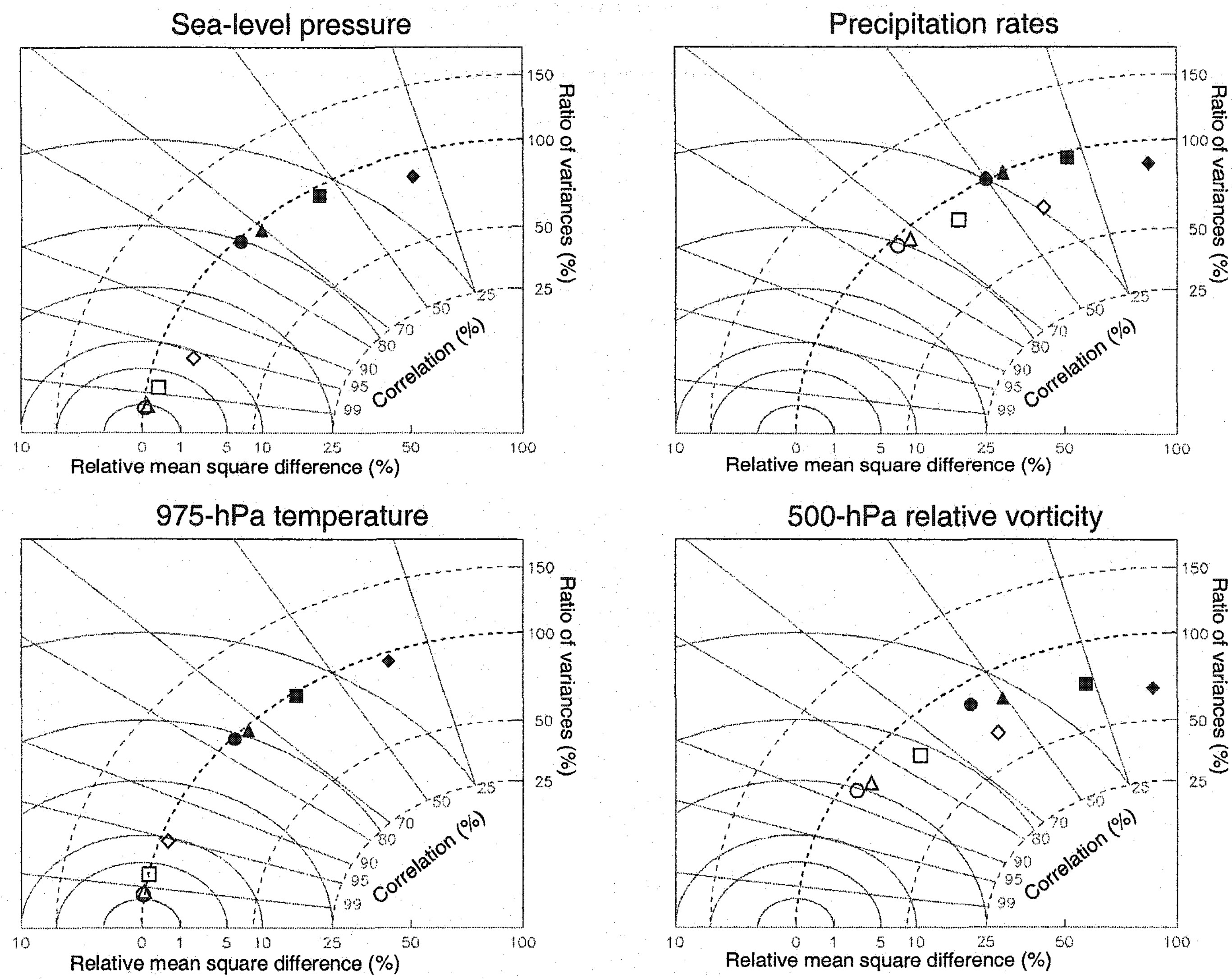

Fig. 19. Same as in Fig. 18, but for the *transient* component of the fields.

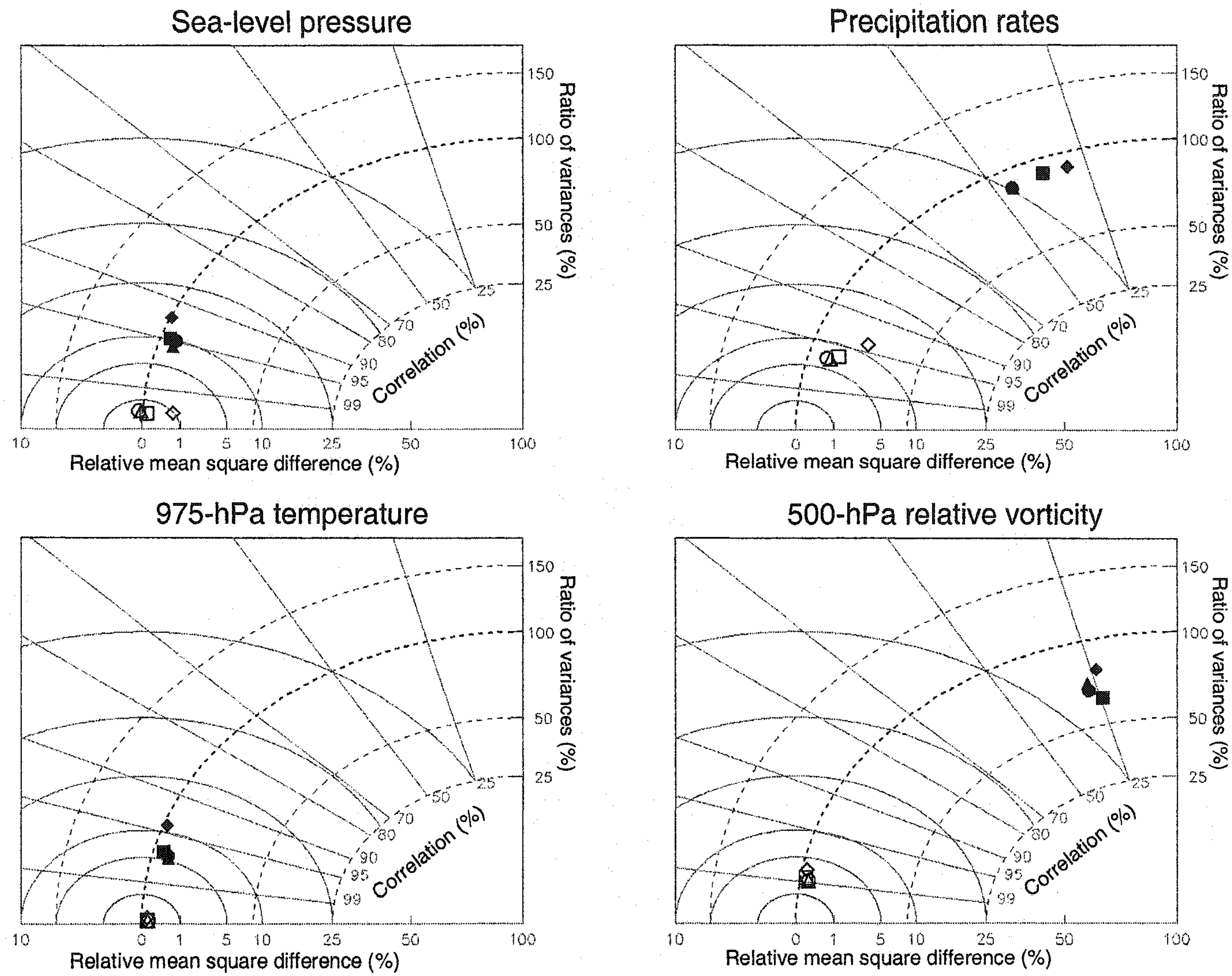

Fig. 20. Taylor diagrams showing the effect of update frequency for J12 on the *stationary* component of the sea-level pressure, precipitation rates, 975-hPa temperature and 500-hPa vorticity fields. Circles: J12-U8, triangles: J12-U4, squares: J12-U2, diamonds: J12-U1. The open symbols are for the total fields and the filled ones are for their small-scale components only.

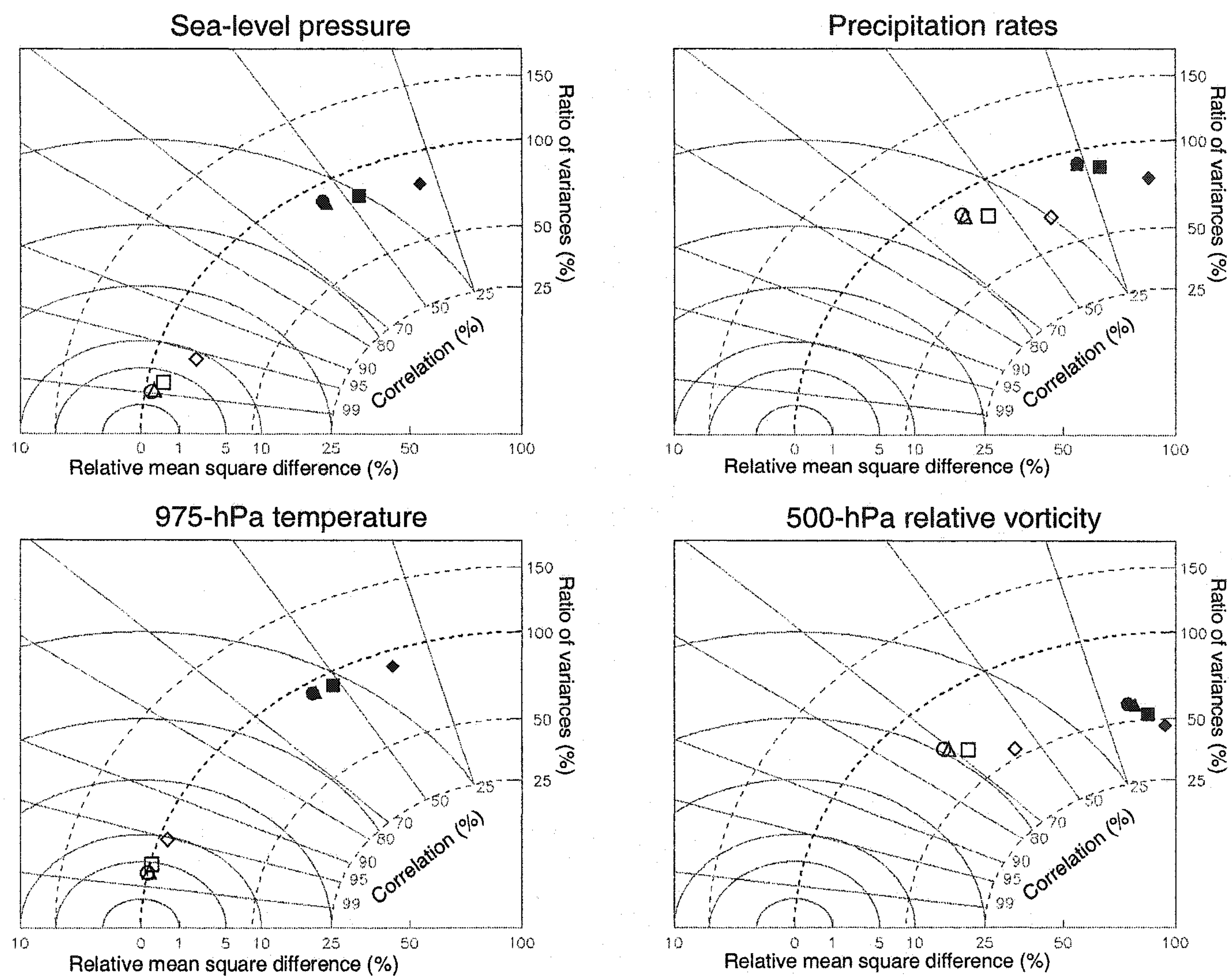

Fig. 21. Same as in Fig. 20, for the *transient* component of the fields

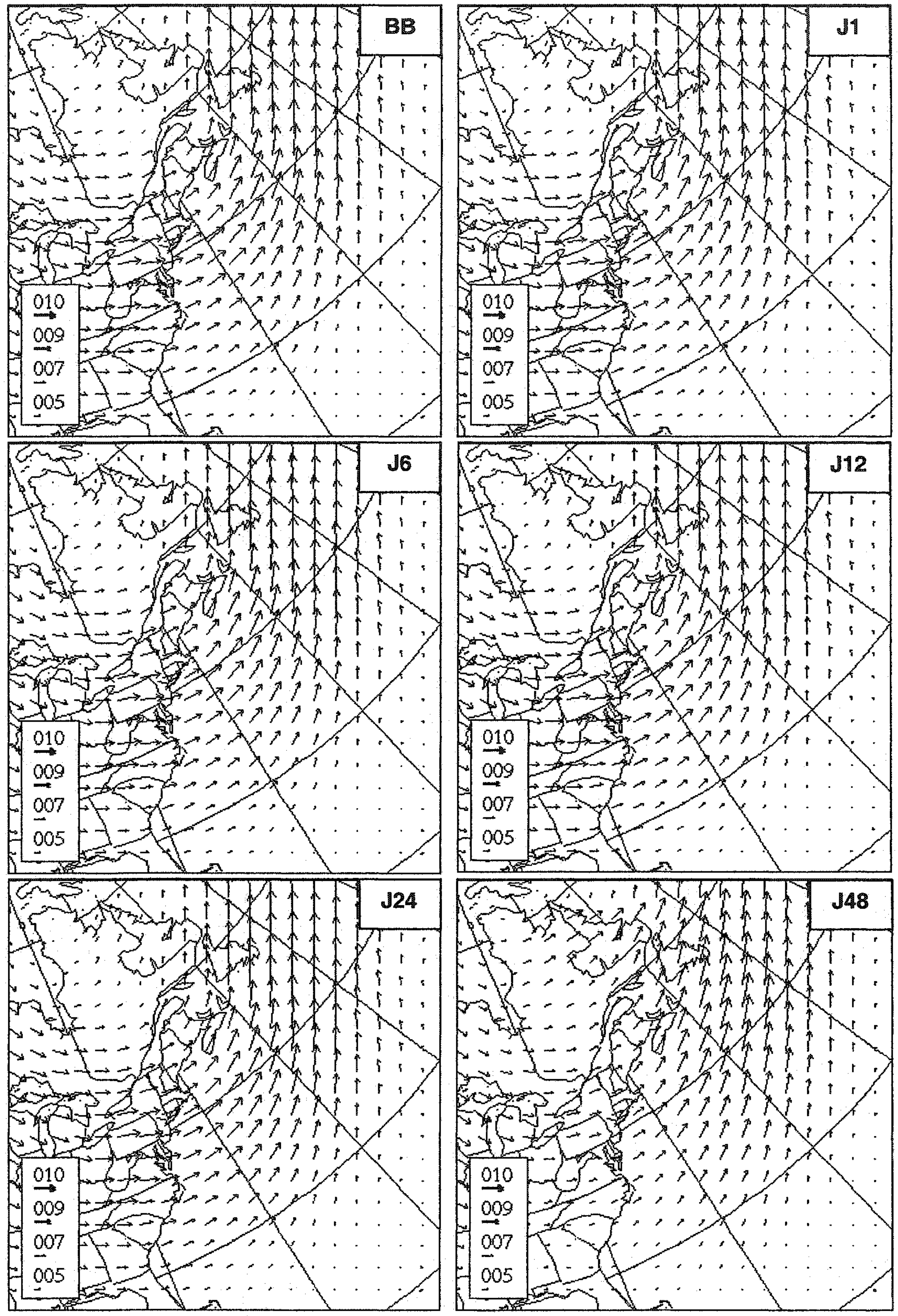

Fig. 22. Stationary component of the total 850-hPa wind fields (m s^{-1}).

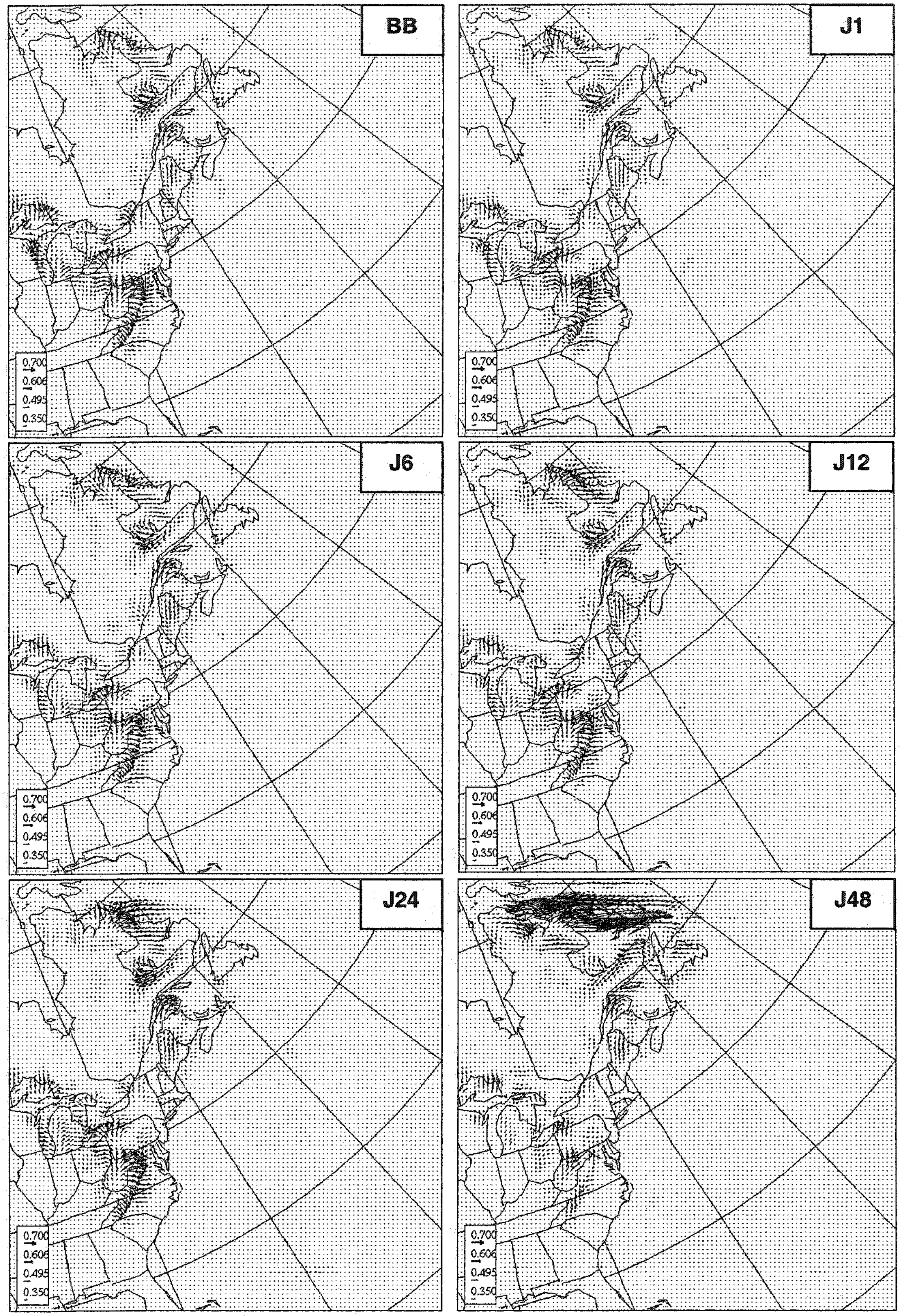

Fig. 23. Stationary component of the fine-scale component of the 850-hPa wind fields (m s^{-1}).

a) b)

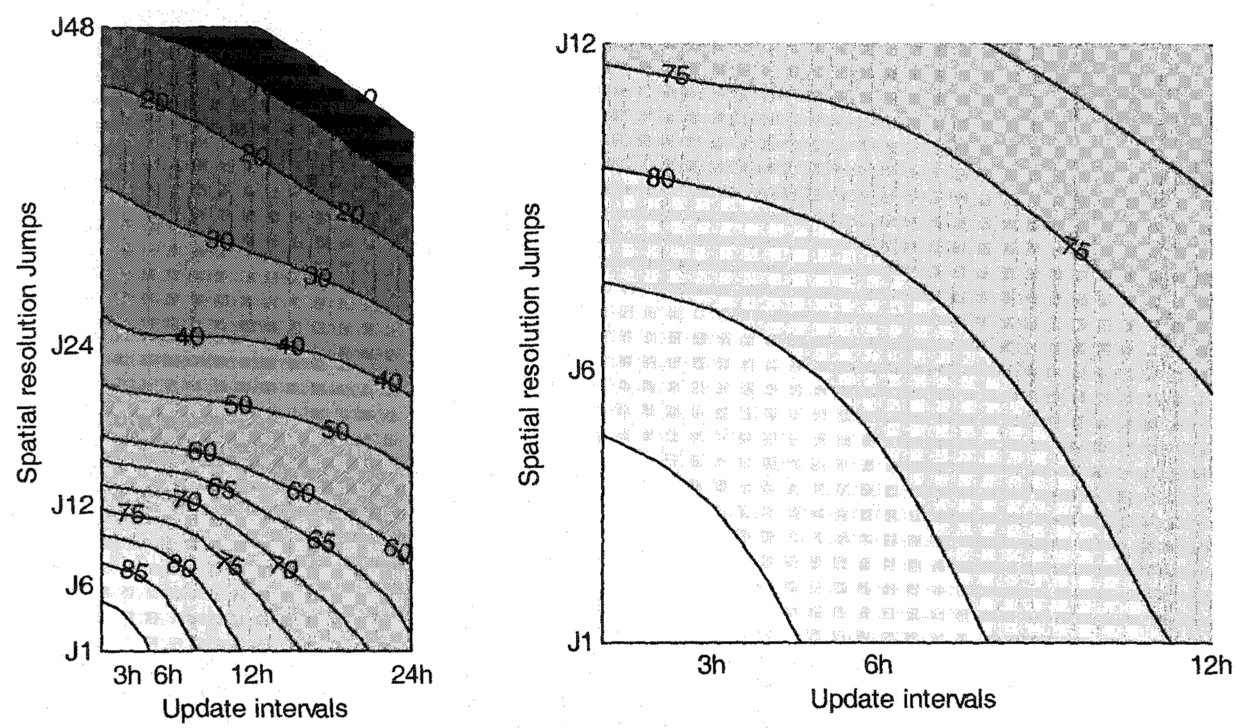

Fig. 24. Ratios of the variance of transient-eddy relative vorticity between the Little and Big Brother as a function of the spatial resolution jumps and update intervals of the lateral boundary conditions. Plot b) is a enlargement of the lower-left corner of plot a). The isolines have been generated by fitting the simulated-results statistics.

Tables

TABLE 1. List the experiments performed in this work. The first column of Xs shows the simulations performed for studying the impact of the spatial resolution jump between the LBC and the Little Brother; the first row of Xs is for studying the impact of the temporal update frequency of the LBC. The Ys are additional experiments for testing the effect of the temporal update frequency on a 45-km grid-point RCM that would be driven by T30 resolution data.

	U8 (3 hours)	U4 (6 hours)	U2 (12 hours)	U1 (24 hours)
J1	X	X	X	X
J6 (T60)	X			
J12 (T30)	X	Y	Y	Y
J24 (T15)	X			
J48 (T7)	X			

Chapter V

Conclusion

The main objective of this thesis was to test and validate the use of one-way nested regional climate models for downscaling large-scale information to the regional scale. In other words, the work presented was aimed at answering this question:

"Can a one-way nested regional climate model (RCM) accurately simulate fine-scale climate features when driven by large-scale information only?"

Asking this question is easier than to answer it. In effect, the validation of the climate fine-scale features produced by such a downscaling tool requires spatio-temporal high-resolution datasets than are not easy to obtained from brute observations nor from objective analyses, although some limited regions during intense observation periods are sometimes of a certain usefulness. In order to circumvent these deficiencies and to avoid mixing sources of errors, we turned our efforts to a perfect-prognosis methodology that we have called the Big-Brother Experiment. With this experiment, we are capable to test whether or not an RCM, using the one-way nesting strategy to downscale large-scale information, is capable to reproduced the regional climate, including the fine-scale features, that has been generated by itself. This sought capacity of our Little Brother to reproduce its Big Brother is fundamental since a failure to do so would necessary mean the uselessness of such a one-way RCM strategy for unreliability reasons. Therefore, a success in passing the BBE should be seen as an important and necessary condition, but not necessarily sufficient for clearing any doubts about this downscaling technique. Having put our work in context, this thesis leads us to the following main conclusions:

1) When an RCM is driven by data of spatial resolution similar to that of current GCMs of global objective analyses, it is found that

- Small-scale low-level features absent from the initial and lateral boundary conditions are almost fully re-generated by the one-way nested RCM within the first day of integration.

- Mesoscale features of sea level pressure and low-level temperature are simulated with a high level of accuracy. This conclusion applies as well to the mesoscale stationary features as to their time variability.

- The downscaling ability for the stationary precipitation patterns shows some skill except over areas dominated by stochastic convective activity. The time variability of precipitation is well reproduced.

- Some weaknesses has been noted in the middle and upper troposphere for the relative vorticity field where its time variability cannot be fully recovered by the RCM. This suggests that the nested domain of the Little Brother we employed might not have been large enough.

- Surface heterogeneities play a great role in determining stationary mesoscale climate features. The small-scale transient activity generated by nonlinear dynamics of the atmosphere, i.e. the cascade of information from the large-scale flow, is also generally well simulated by the one-way nesting RCM. But its spatial pattern has a more random behaviour than for the small scales directly forced by stationary surface forcings.

2) When the spatial resolution and the temporal updating frequency of the LBC are varied for investigating their impact on the simulated climate, it is found that

- Spatial resolution jumps up to 12 times between the resolution of the nesting LBC data and the RCM can yield reliable regional climate for most fields studied with an RCM at 45 km of resolution.

- Update frequency of twice a day (every 12 hours) seems sufficient but a 6-hour interval is significantly better and should be used since there is little increase of computational cost related to do so. No improvement was found by going from 6 to 3 hours in our tests with a 45-km grid-point RCM.

- Although the 500-hPa relative vorticity was the most affected variables when the resolution of the LBC was degraded, the most important climate fields, such as those of the precipitation, temperature, and sea-level pressure fields were far less affected. The last two fields showed the most robustness to the LBC resolution degradation; their largest scales did not need high-resolution LBC to be well nested, and their stationary fine-scale components are in turn strongly forced by the surface heterogeneities and therefore rather independent of the LBC.

- The combination of T32 and 6-hour interval that is currently employed in the Canadian RCM mode of operation seems acceptable, although significant improvements can be anticipated by reducing the spatial resolution jump from 12 to 6 times, i.e. by the use of T60 resolution GCM driving data.

In addition to the work presented in this thesis, the author has participated, during the last two years, to another area of meteorological scientific research with Prof. R. Laprise and Dr. R. de Elía. The topic of the research was the scale-dependence of *short-term* predictability. Two papers resulted from this collaboration: *Predictability in a Nested*

Limited-area Model (Laprise, Ravi Varma, Denis, Caya and Zawadski, 2000) and *Scale-Dependent Predictability of a Limited-area Model* (de Elía, Laprise and Denis, 2001). This research employed the BBE methodology (Chapter III & IV) and made use of the spectral decomposition using the DCT (Chapter II). The work done is this thesis and that done in these two papers led to apparent opposite conclusions concerning reliability of one-way nesting strategy; the nesting is reliable for climate (months to years) simulation of the statistics of the fine-scales but not for short-term (~ hours to days) deterministic prediction. The apparent contradiction of these conclusions can be attributed to the fact that the so-called climate quantities and their associated verifications are different than those related to deterministic short-term weather forecasting. In the first case, climate statistics such as averages, standard deviations and extremes are of primary interest; in the second case the intensity, position *and* timing are of major concern and proved to be more difficult to meet for fine-scale features generated by a one-way nested model.

Future work implying our BBE should aim at addressing other important issues such as the effect of the domain size and location, the season, and whether or not an RCM should improve the large-scale circulation of its driving model. Finally, the "one-way" nesting approach should be ultimately compared with an approach allowing for "two-way" interactions, such as a variable-resolution global climate model.

References

Achtemeier, G. L., 1986: The impact of data boundaries upon a successive corrections objective analysis of limited-area datasets. *Mon. Wea. Rev.*, **114**, 40-49.

Ahmed, N., T. Natarajan, and K. R. Rao, 1974: Discrete Cosine Transform. *IEEE Trans. Computers*, **C-23**, 90-93.

Barnes, L. S., 1986: On the accuracy of omega diagnostic computations. *Mon. Wea. Rev.*, **114**, 1664-1680.

Baumhefner, D. P., and D. J. Perkey, 1982: Evaluation of lateral boundary errors in a limited domain model. *Tellus*, **34**, 409-428.

Bergeron, G., R. Laprise, and D. Caya, 1994: *Formulation of the Mesoscale Compressible Community (MC2) model.*, Cooperative Centre for Research in Mesometeorology, 165 pp.

Bergeron, S. Y., A. P. Vincent, D. A. Yuen, J. S. Tranchant, and C. Tchong, 1999: Viewing seismic velocity anomalies with 3-D continuous Gaussian wavelets. *Geophys. Res. Lett.*, **26**, 2311-2314.

Biner, S., D. Caya, R. Laprise, and L. Spacek, 2000: Nesting of RCMs by imposing large scales., 7.3-7.4. In: Research activities in Atmospheric and Oceanic Modelling, WMO/TD - No. 987, Report No. 30.

Boer, G. J., and S. J. Lambert, 2001: Second-order space-time climate difference statistics. *Climate Dyn.*, **17**, 213-218.

Boer, G. J., and T. G. Shepherd, 1983: Large-scale two-dimensional turbulence in the atmosphere. *J. Atmos. Sci.*, **40**, 164-184.

Bourke, W., 1972: An efficient one-level primitive equation spectral model. *Mon. Wea. Rev.*, **100**, 683-689.

CAS/JSC WGNE, 1999: *Report of Fourteenth Session of the CAS/JSC Working Group on Numerical Experimentation (Recherche en Prévision Numérique, Environnement Canada, Doval, Québec, Canada, 2-6 November 1998).* No. 14, WMO/TD-NO. 964, World Meteor. Org., 28 pp.

CAS/JSC WGNE, 2000: *Report of Fifteenth Session of the CAS/JSC Working Group on Numerical Experimentation (Naval Research Laboratory, Monterey, CA, USA, 25-29 October 1999).* No. 15, WMO/TD-NO. 1024, World Meteor. Org., 29 pp.

Caya, D., and R. Laprise, 1999: A semi-implicit semi-Lagrangian regional climate model: The Canadian RCM. *Mon. Wea. Rev.*, **127**, 341-362.

Christensen, O. B., J. H. Christensen, B. Machenhauer, and M. Botzet, 1998: Very high-resolution regional climate simulations over Scandinavia-present climate. *J. Climate*, **11**, 3204-3227.

Cocke, S., and T. E. LaRow, 2001: Seasonal predictions using a regional spectral model embedded within a coupled ocean–atmosphere model. *Mon. Wea. Rev.*, **128**, 689–708.

Daley, R., C. Girard, J. Henderson, and I. Simmonds, 1976: Short-term forecasting with a multi-level spectral primitive equation model. *Mon. Wea. Rev.*, 99-134.

Davies, H. C., 1976: A lateral boundary formulation for multi-level prediction models. *Quart. J. Roy. Meteor. Soc.*, **102**, 405-418.

Davies, H. C., and R. E. Turner, 1977: Updating prediction models by dynamical relaxation: an examination of the technique. *Quart. J. Roy. Meteor. Soc.*, **103**, 225-245.

de Elía, R., R. Laprise, and B. Denis, 2001: Forecast skill limits of nested, limited-area models: A perfect-model approach. *Accepted in Mon. Wea. Rev.*

Denis, B., J. Côté, and R. Laprise, 2001a: Spectral decomposition of two-dimensional atmospheric fields on limited-area domains using the discrete cosine transform (DCT). *Mon. Wea. Rev. (submitted).*

Denis, B., R. Laprise, D. Caya, and J. Côté, 2001b: Downscaling ability of one-way nested regional climate models: the big-brother experiment. *Accepted for publication in Climate Dyn.*

Déqué, M., P. Marquet , and R. G. Jones, 1998: Simulation of climate change over Europe using a global variable resolution general circulation model. *Climate Dyn.*, **14**, 173-189.

Dickinson, R. E., R. M. Errico, F. Giorgi, and G. T. Bates, 1989: A regional climate model for the Western United States. *Climate Change*, **15**, 383-422.

Errico, R. M., 1985: Spectra computed from a limited-area grid. *Mon. Wea. Rev.*, **113**, 1554-1562.

Errico, R. M., 1987: A comparison between two limited-area spectral analysis schemes. *Mon. Wea. Rev.*, **115**, 2856-2861.

Farge, M., 1992: Wavelet transforms and their applications to turbulence. *Annu. Rev. Fluid Mech.*, **24**, 395-457.

Flato, G. M., G. J. Boer, W. G. Lee, N. A. McFarlane, D. Ramsden, M. C. Reader, and A. J. Weaver, 2000: The Canadian Centre for Climate Modelling and Analysis Global Coupled Model and its Climate. *Climate Dyn.*, **16**, 451-467.

Fox-Rabinovitz, M. S., G. L. Stenchikov, M. J. Suarez, L. L. Takacs, and R. C. Govindaraju, 2000: A uniform- and variable-resolution stretched-grid GCM dynamical core with realistic orography. *Mon. Wea. Rev.*, **128**, 1883–1898.

Giorgi, F., 1990: Simulation of the regional climate using a limited-area model nested in a general circulation model. *J. Climate*, **3**, 941-963.

Giorgi, F., M. R. Marinucci, and G. T. Bates, 1993: Development of a second-generation regional climate model (RegCM2). Part II: Convective processes and assimilation of lateral boundary conditions. *Mon. Wea. Rev.*, **121**, 2814-2832.

Giorgi, F., and L. O. Mearns, 1999: Introduction to special section: regional climate modeling revisited. *J. Geophys. Res.*, **104**, 6335-6352.

Gonzalez, R. C., and R. E. Woods, 1992: *Digital image processing / by Rafael C. Gonzalez, Richard E. Woods* Addison-Wesley, 716 pp.

Grotjahn, R., and C. Castello, 2000: A study of frontal cyclone surface and 300-hPa geostrophic kinetic energy distribution and scale change. *Mon. Wea. Rev.*, **128**, 2865-2874.

Hong, S.-Y., and A. Leetmaa, 1999: An evaluation of the NCEP RSM for regional climate modeling. *J. Climate*, **12**, 592-609.

Houghton, J. T., Y. Ding, D. J. Griggs, M. Noguer, P. J. van der Linden, and D. Xiaosu, 2001: *Climate Change 2001: The Scientific Basis*. Cambridge University Press, 944 pp.

Houghton, J. T., G. J. Jenkins, and J. J. Ephraums, 1990: *Climate Change—The IPCC Scientific Assessment*. Cambridge University Press, 365 pp.

Houghton, J. T., L. G. Meira Filho, B. A. Callander, N. Harris, A. Kattenberg, and K. Maskell, 1996: *Climate Change 1995: The science of climate change*. Cambridge University Press, 572 pp.

Jacob, D., and R. Podzun, 1997: Sensitivity studies with the regional climate model REMO. *Meteorol. Atmos. Phys*, **63**, 119-129.

Ji, Y., and A. D. Vernekar, 1997: Simulation of the Asian summer monsoons of 1987 and 1988 with a regional model nested in a global GCM. *J. Climate*, **10**, 1965-1979.

Jones, R. G., J. M. Murphy, and M. Noguer, 1995: Simulation of climate change over Europe using a nested regional-climate model. I: Assessment of control climate, including sensitivity to location of lateral boundaries. *Quart. J. Roy. Meteor. Soc.*, **121**, 1413-1449.

Jones, R. G., J. M. Murphy, M. Noguer, and A. B. Keen, 1997: Simulation of climate change over Europe using a nested regional-climate model. I: Comparison of driving and regional model responses to a doubling of carbon dioxide. *Quart. J. Roy. Meteor. Soc.*, **123**, 265-292.

Juang, H.-M. H., and M. Kanamitsu, 1994: The NMC nested regional spectral model. *Mon. Wea. Rev.*, **122**, 3-26.

Kain, J. S., and J. M. Fritsch, 1990: A one-dimensional entraining/detraining plume model and its application in convective parameterization. *J. Atmos. Sci.*, **47**, 2784-2802.

Laprise, R., D. Caya, G. Bergeron, and M. Giguère, 1997: The formulation of André Robert MC2 (Mesoscale Compressible Community) model. The André J. Robert Memorial Volume (C. Lin, R. Laprise and H. Ritchie, Eds.), companion volume to *Atmos.-Ocean*, **35**, 195-220.

Laprise, R., D. Caya, M. Giguère, G. Bergeron, H. Côté, J.-P. Blanchet, G. Boer, and A. N. McFarlane, 1998: Climate and climate change in western Canada as simulated by the Canadian regional climate model. *Atmos.-Ocean*, **36**, 119-167.

Laprise, R., M. K. Ravi Varma, B. Denis, D. Caya, and I. Zawadzki, 2000: Predictability in a nested limited-area model. *Mon. Wea. Rev.*, **128**, 4149-4154.

Laprise, R., and P. Zwack, 1992: Variation de l'activité cyclonique dans un scénario double CO2. *Le Climat*, **10**, 39-62.

Leung, L. R., and S. J. Ghan, 1999: Pacific Northwest climate sensitivity simulated by a regional climate model driven by a GCM. Part I: Control simulations. *J. Climate*, **12**, 2010-2030.

Maddox, R. A., 1979: An objective technique for separating macroscale and mesoscale features in meteorological data. *Mon. Wea. Rev.*, **108**, 1108-1121.

Majewski, D., 1997: Operational Regional Prediction. *Meteorol. Atmos. Phys.*, **63**, 89-104.

Matlab, 1998: Matlab / The language of Technical Computing, version 5.2.

McFarlane, N. A., G. J. Boer, J.-P. Blanchet, and M. Lazare, 1992: The Canadian Climate Centre second-generation general circulation model and its equilibrium climate. *J. Climate*, **5**, 1013-1044.

McGregor, J. L., 1997: Regional climate modelling. *Meteorol. Atmos. Phys.*, **63**, 105-117.

Noguer, M., R. Jones, and J. Murphy, 1998: Sources of systematic errors in the climatology of a regional climate model over Europe. *Climate Dyn.*, **14**, 691-712.

Pauley, P. M., 1990: On the evaluation of boundary errors in the Barnes objective analysis scheme. *Mon. Wea. Rev.*, **118**, 1203-1210.

Pauley, P. M., and X. Wu, 1990: The theoretical, discrete, and actual response of the Barnes objective analysis scheme for one- and two-dimensional fields. *Mon. Wea. Rev.*, **118**, 1145–1164.

Pennebaker, W. B., and J. L. Mitchell, 1993: *JPEG still image data compression standard/ William B. Pennebaker, Joan L. Mitchell* Van Nostrand Reinhold, 638 pp.

Pratt, W. K., 1991: *Digital image processing / William K. Pratt* Wiley, 698 pp.

Press, W. H., 1992: *Numerical recipes in FORTRAN: the art of scientific computing.* Cambridge University Press, 963 pp.

Raymond, W. H., 1989: High-order, high-pass implicit filters for evaluating information within finite areas. *Mon. Wea. Rev.*, **117**, 2772-2781.

Raymond, W. H., and A. Gardner, 1991: A review of recursive and implicit filters. *Mon. Wea. Rev.*, **119**, 477-495.

Risbey, J. S., and P. H. Stone, 1996: A case study of the adequacy of GCM simulations for input to regional climate change assessments. *J. Climate*, **9**, 1441-1467.

Robert, A., and E. Yakimiw, 1986: Identification and elimination of an inflow boundary computational solution in limited area model integrations. *Atmos.-Ocean*, **24**, 369-385.

Salvador, R., J. Calbó, and M. M. Millán, 1999: Horizontal grid size selection and its Influence on mesoscale model simulations. *J. Appl. Meteor.*, **38**, 1311–1329.

Sardeshmukh, P. D., and B. J. Hoskins, 1984: Spatial smoothing on the sphere. *Mon. Wea. Rev.*, **112**, 2524-2529.

Seth, A., and F. Giorgi, 1998: The effects of domain choice on summer precipitation simulation and sensitivity in a regional climate model. *J. Climate*, **11**, 2698–2712.

Shuman, F. G., 1957: Numerical methods in weather prediction: II. Smoothing and filtering. *Mon. Wea. Rev.*, 357-361.

Staniforth, A., 1997: Regional modeling: A theoretical discussion. *Meteorol. Atmos. Phys.*, **63**, 15-29.

Takle, E. S., W. J. Gutowski, Jr., R. W. Arritt, Z. Pan, C. J. Anderson, R. R. da Silva, D. Caya, S.-C. Chen, F. Giorgi, J. H. Christensen, S.-Y. Hong, H.-M. H. Juang, J. Katzfey, W. M. Lapenta, R. Laprise, G. E. Liston, P. Lopez, J. McGregor, R. A. Pielke, Sr., and J. O. Roads, 1999: Project to Intercompare Regional Climate Simulations (PIRCS): Description and initial results. *J. Geophys. Res.*, **104**, 19443-19461.

Taylor, K. E., 2001: Summarizing multiple aspects of model performance in a single diagram. *J. Geophys. Res.*, **106**, 7183-7192.

Trenberth, K. E., and A. Solomon, 1993: Implications of global atmospheric spatial spectra for processing and displaying data. *J. Climate*, **6**, 531-545.

Turner, S., 1994: Analyse spectrale des données du modèle régional du climat de l'UQAM. Master thesis, Université du Québec à Montréal, Sciences de l'Atmosphère, Montréal, 113 pp.

Van Tuyl, A. H., and R. M. Errico, 1989: Scale interaction and predictability in a mesoscale model. *Mon. Wea. Rev.*, **117**, 495-517.

von Storch, H., H. Langenberg, and F. Feser, 2000: A spectral nudging technique for dynamical downscaling purposes. *Mon. Wea. Rev.*, **128**, 3664–3673.

Waldron, K. M., J. Paegle, and J. D. Horel, 1996: Sensitivity of a spectrally filtered and nudged limited-area model to outer model options. *Mon. Wea. Rev.*, **124**, 529-547.

Walsh, K., and J. L. McGregor, 1995: January and July climate simulations over the Australian region using a limited-area model. *J. Climate*, **10**, 2387-2403.

Warner, T. T., R. A. Peterson, and R. E. Treadon, 1997: A tutorial on lateral boundary conditions as a basic and potentially serious limitation to regional numerical weather prediction. *Bull. Amer. Meteor. Soc.*, **78**, 2599-2617.

Weygandt, S. S., 1994: Quantification of predictive skill for mesoscale and synoptic-scale meteorological features as a function of horizontal grid resolution. *Mon. Wea. Rev.*, **122**, 57-71.

Xue, M., 2000: High-order monotonic numerical diffusion and smoothing. *Mon. Wea. Rev.*, **128**, 2853-2864.

Yakimiw, E., and A. Robert, 1990: Validation experiments for a nested grid-point regional forecast model. *Atmos.-Ocean*, **28**, 466-472.